

SCANNING TUNNELING MICROSCOPY AND SPECTROSCOPY OF SILICON AND CARBON SURFACES

Thesis by
Shenda Mary Baker

In Partial Fulfillment of the Requirements
for the Degree of
Doctor of Philosophy

California Institute of Technology
Pasadena, California

1992
(Submitted October 15, 1991)

Acknowledgments

The growth of a graduate student from a naive first year student to an "experienced" scientist, worthy of being decreed "*Doctor*" is a long process that involves a number of people. I would like to thank some of these people who helped me in my scientific endeavors, contributed to the research and who provided the laughter and the encouragement along the way.

During my first few years in the STM group, Richard Colton, visiting scientist from the Naval Research Labs, shared his experience in approaching problems and a dialog that has continued throughout the years. Bill Kaiser has continued up to the end to be an excellent "sanity check" for scientific ideas, an endless and enthusiastic source of information about semiconductor spectroscopy and was always willing to share his ideas.

John T. Yates, Jr. at the University of Pittsburgh, graciously shared his laboratory for one phenomenal month. I thank him for that opportunity and the advice on future employment. I owe much of my sanity and humor to Patrick Taylor who continued to share his scientific and graduate school experiences with me long after the Pittsburg exchange had ended.

John Kramar and Michael Wiemer were instrumental in bringing me up to speed on the UHV-STM. They, Michael Youngquist and Chunli Bai are primarily responsible for the graphics, software and hardware on that system. Robert Driscoll provided the tip etching apparatus. The members of the JDB group, from 1985 until now, all contributed in some way to this thesis. Mark Junge contributed the more artistic renderings of designs, and his work is marked with the initials MMJ

George Rossman graciously agreed to be the "fourth" on my thesis committee. He provided incredible diamond samples (!!!) and was always interested in the latest result. His guidance in all of the diamond work is greatly appreciated. I also appreciate the efforts of the remainder of my committee--Jack Beauchamp and Bill Goddard.

Special thanks are due to Guy Duremburg, Tony Stark and Ray Garcia, who spent countless hours milling, drilling and advising for both the construction of the atmospheric STM and the numerous heater iterations, to Tom Dunn for valuable electronic advice . . . I wonder how many theses they are part of . . .

Maria Giorgi started at Caltech the same year as I, and throughout our experiences here, provided friendship and support as did the members of the Supper Club. The 6:30 am Saturday morning Rose Bowl running group also contributed greatly to my sanity and my extracurricular amusement!

Throughout my years at Caltech, John Baldeschwieler provided the encouragement and the respect for his students that produce capable graduates, prepared for "the next step". I enjoyed his wealth of experiences both in addressing scientific inquiry and the politics of employment situations. He provided for or permitted incredible opportunities in addition to the Caltech experience, always in my best interest, the student, not the least of which were an incredible teaching job at Harvey Mudd College, an STM conference in Oxford, UK and a month at the University of Pittsburgh. In addition to Caltech-related work, I was fortunate to know John and Marlene on a personal level through a group of devoted runners and value the discussions that we had while ticking off the miles, topics ranging from technitium labelling applications in the medical field to tip effects in STM to the preferred breakfast spot in Santa Barbara.

I would like to thank my entire family who support me without qualification, especially my parents who assured me from preschool that I could accomplish any desired feat. I also thank them for supporting my relatively expensive academic tastes.

James Sterling, my husband, friend, advisor and confidant deserves more gratitude and respect than words can describe for the laughter, the miles, the smiles, the silliness, the love and the infinite support.

The work of *Chapter 2* is based primarily upon work supported under a National Science Foundation Graduate Fellowship and by the Office of Naval Research, the Shell Companies Foundation, Inc. and the National Institutes of Health. Technical assistance was provided by Pat Koen of the Caltech Electron Microscope Facility, Carol Garland of the Caltech Material Sciences Department and J. Wandass and R. Jones of the NRL Surface Chemistry Branch. All of the XPS work of *Chapter 4* was graciously provided by Richard Vasquez at the Jet Propulsion Laboratory, and the Ion Microprobe work was done by Robert Wilson of Hughes Research Laboratories.

I would like to thank the National Science Foundation, the National Institutes of Health Biotechnology Program-National Research Service Award, Office of Naval Research, Shell Oil Foundation and Abbott Laboratories for their support.

*If I knew what to integrate
To find a diamond surface state
On density, I'd meditate
For voltage, charge would mediate
And IV curves, I'd recreate
Hypotheses to reinstate
With exponential tunnel rate
Obscuring the filled sample trait . . .*

My thesis I'd expediate.

SMB
9/26/91

Abstract

Scanning Tunneling Microscopy (STM) investigations and additional surface analyses were performed on carbon and silicon surfaces. A number of anomalies have been observed on highly oriented pyrolytic graphite (HOPG), including large corrugations, distorted images, large range of tip motion and the absence of defects. A mechanism involving direct contact between tip and sample or contact through a contamination layer to provide an additional conduction pathway is proposed. This model of point-contact imaging provides an explanation for added stability of the STM system, a mechanism for producing multiple tips or sliding graphite planes and an explanation for the observed anomalies. These observations indicate that the use of HOPG for testing and calibration of STM instrumentation may be misleading. Designs for the atmospheric STM used in this study are also presented.

The conditions necessary for preparing a clean silicon(111) (7x7) surface are discussed. The design and analysis of heaters necessary to prepare the silicon reconstructed surface at ultrahigh vacuum (UHV) are described. Results from both radiatively and resistively heated samples are shown in addition to a comparison of topographic and barrier height images of the boron ($\sqrt{3} \times \sqrt{3}$) reconstructed surfaces. A spectroscopic distinction between sites of boron, silicon or contaminants is demonstrated.

A synthetic boron-doped diamond was examined by a number of analytical techniques in order to determine its composition and surface morphology. Current-voltage spectroscopy taken with the STM indicates that the diamond Fermi level can be pinned in atmospheric conditions. In ultrahigh vacuum, band bending is observed, but the strength of the electric field experienced by the diamond semiconductor is less than expected; introduction of surface charges is shown to account for the field screening.

Presentation of an STM study of a protein-antibody complex on a gold surface illustrates the requirements for and difficulties of imaging large biomolecules. A flat, conducting substrate and sample stability on the surface are shown and discussed. Molecular manipulation by the STM tip is also presented. Although routine imaging of large adsorbates on surfaces is not yet possible, this study presents the obstacles and the potential afforded by the STM in attaining this goal.

TABLE OF CONTENTS

<i>Acknowledgments</i>	ii
<i>Abstract</i>	vi
<i>Table of Contents</i>	vii
<i>Chapter 1. Introduction</i>	1
INTRODUCTION	2
<i>Purpose</i>	2
<i>Review of the Technique</i>	3
Basic Theory	4
Data Collection	5
Barrier Height Measurements	5
Current-Voltage Spectroscopy.....	7
Image Processing and Presentation.....	7
SUMMARY OF CHAPTERS.....	8
<i>Chapter 2. Imaging and Spectroscopy of Graphite in Air by Scanning Tunneling Microscopy: Role of the Tip</i>	10
INTRODUCTION	11
EXPERIMENT.....	14
<i>Preparation of Oxide-Free Tips</i>	14
<i>Microscopy and Spectroscopy</i>	14
RESULTS AND DISCUSSION.....	15
<i>Characterization and Analysis of Graphite Tips</i>	15
<i>Imaging Results with Oxide-Free Tips</i>	16
<i>Effect of Tip Geometry and Orientation on the Image of HOPG</i>	18
<i>Point-Contact Imaging</i>	20
<i>Point-Contact Spectroscopy</i>	21
<i>Discussion of Spectroscopy Anomalies</i>	22
CONCLUSION.....	24
FIGURES.....	25

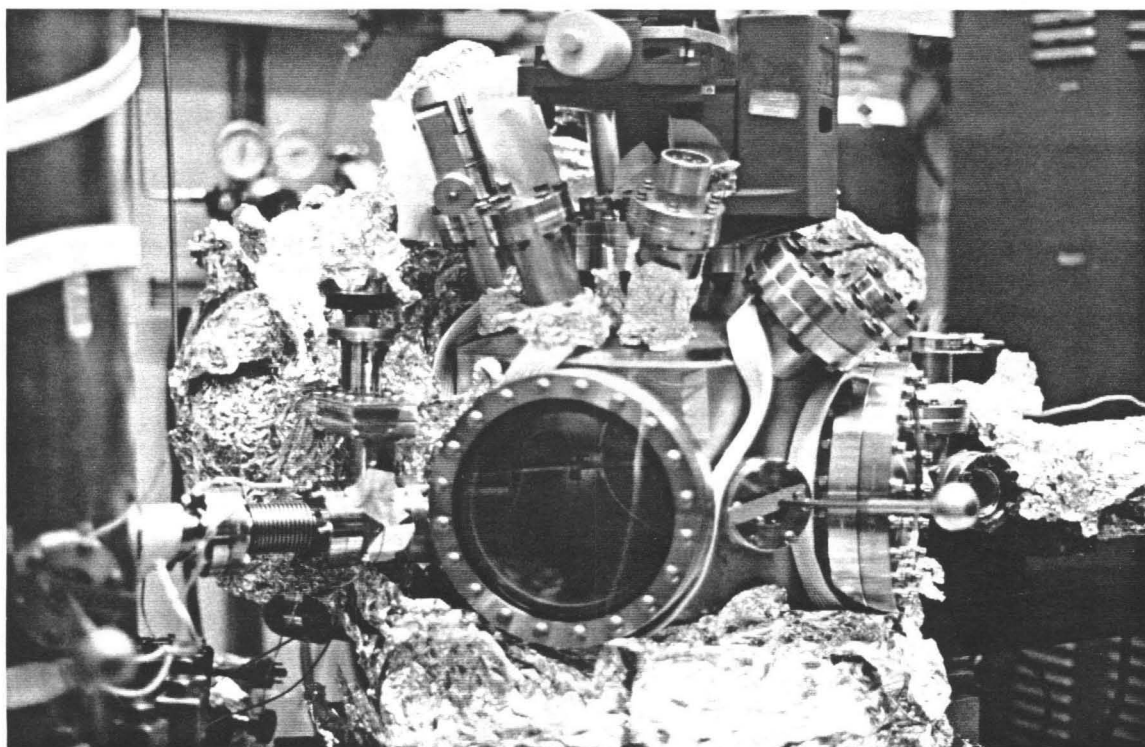
<i>Chapter 3. Preparation and Analysis of the Silicon (111) Surface</i>	36
INTRODUCTION	37
<i>Background</i>	37
<i>Proposed Experiments</i>	38
<i>Summary</i>	39
THEORY AND EXPERIMENT	40
<i>Preparation of Si(111) (7x7)</i>	40
<i>Radiative Heating</i>	41
Theory and Design.....	41
Experimental Parameters	44
<i>Resistive Heating</i>	44
Theory and Design.....	44
Experimental Parameters	46
<i>System Modifications</i>	46
<i>In-Situ Tip-Transfer Design</i>	46
<i>Vacuum Gas Doser Design</i>	47
<i>IR Heater for Sample Preparation Chamber Bake</i>	48
RESULTS	48
<i>Radiative Heating</i>	48
<i>Resistive Heating</i>	49
Boron Reconstruction on Si(111)	49
Topography of Resistively Heated Si(111).....	54
DISCUSSION	55
CONCLUSION.....	57
FIGURES.....	58
<i>Chapter 4. Topology, Composition and Spectroscopy of Synthetic Boron-doped Diamond</i>	76
INTRODUCTION	77
<i>Background</i>	77
<i>Purpose</i>	80

EXPERIMENT.....	81
<i>Compositional and Orientational Analyses.....</i>	81
<i>Scanning Tunneling Microscopy and Surface Analyses.....</i>	82
RESULTS.....	83
<i>Macroscopic Diamond Characterization.....</i>	83
<i>Laue Diffraction and Optical Goniometry.....</i>	83
<i>Secondary Ion Mass Spectroscopy.....</i>	84
<i>X-ray Photoelectron Spectroscopy.....</i>	86
<i>Scanning Tunneling Microscopy.....</i>	88
<i>Scanning Tunneling Spectroscopy.....</i>	89
DISCUSSION.....	90
<i>Contaminants and Dopants in Semiconducting Diamond.....</i>	91
<i>Imaging Diamond by Tunneling Electrons.....</i>	92
<i>Current-Voltage Spectroscopy.....</i>	95
<i>Surface Potential Screening and Reduced Band Bending.....</i>	95
<i>Pinning of the Fermi Level.....</i>	98
CONCLUSION.....	101
FIGURES.....	103
APPENDIX A: <i>Design and Construction of an Atmospheric Scanning Tunneling Microscope.....</i>	119
INTRODUCTION.....	120
INSTRUMENT DEVELOPMENT.....	120
<i>Vibration Concerns.....</i>	120
<i>Tip Effects.....</i>	121
<i>Operational Modes.....</i>	123
INSTRUMENT DESIGN.....	125
<i>Core STM.....</i>	125
<i>Piezoelectric Ceramics.....</i>	126
<i>Vibration Isolation and Shielding.....</i>	127
<i>Electronics.....</i>	128
<i>Operating Parameters.....</i>	130
<i>Data Collection.....</i>	131
FIGURES.....	132

APPENDIX B: <i>On Imaging Biological Molecules With the Scanning Tunneling Microscope--a Protein-Antibody Complex</i>	153
INTRODUCTION	154
EXPERIMENTAL	155
RESULTS	156
<i>Sputtered Gold Surface</i>	156
<i>Antibody Complex on Sputtered Gold Surface</i>	156
<i>Molecular Manipulation</i>	156
DISCUSSION	157
FIGURES	159

Chapter 1

INTRODUCTION



INTRODUCTION

Purpose

Scanning tunneling microscopy (STM) has rapidly become an important technique for the investigation and understanding of surface structure and chemical reactivity of conducting materials. Since its invention¹, the variety of applications to which it has been applied has outpaced the theory necessary to explain many of the observed phenomena. Although the general mechanisms for electron tunneling from metals to metals, to semiconductors or to superconductors through an insulating layer have been studied and explained² for planar junctions, the unique geometric and size restrictions of the STM tip have produced images and spectroscopy inexplicable by standard theory. In fact, the mechanisms important to STM have little in common with planar junctions--image contrast mechanisms, local effects and tip geometry effects are all considerations unique to the STM and its derivatives (Atomic Force Microscope, Scanning Capacitance Microscope, etc.).

Thus, although basic physical properties of semiconductors and metals in vacuum are often discovered with the STM, interpretation of more complicated systems such as adsorbates on these substrates in vacuum, at ambient conditions, or in liquids is less obvious. As a result, most recent research in STM involves more than simple routine use of an instrument. Careful analysis of the results is necessary to determine any ambiguities in the STM data obtained. In fact, the most highly imaged surface in STM, highly oriented pyrolytic graphite (HOPG) has high visibility as a calibration standard despite the numerous anomalies observed upon imaging.

The leap from high vacuum imaging of metal and semiconductor surfaces to ambient and liquid imaging of large biological molecules left a gap in the theory, unable to explain either the contrast mechanism or the conduction pathway for these insulating systems. A series of experiments that examine the effect of small molecules on the imaging and spectroscopy of the surface by STM would be useful in providing information on a scale between the extremes of bare or single atoms and complex macromolecules

¹G. Binnig and H. Rohrer *Helv. Phys. Acta* 55, 726 (1982)

²See, for example, C. B. Duke *Tunneling in Solids* (Academic Press: New York), 1969

on a surface. By understanding how individual molecules with different functional groups and different molecular bonds above the surface affect the surface wave functions, a basis for the nature of the contrast mechanism and current conduction can be established. By building more complexity into the system upon this foundation, the interpretation of images of large molecules in a variety of environments can be attained as can the necessary STM parameters required to achieve the highest contrast and resolution.

Despite some inherent complexities in STM interpretation, STM data are very useful, especially as a complementary tool with other techniques. Diamond has long been known to be a semiconducting material, but until the recent development of chemical vapor deposition (CVD) techniques able to produce high-quality diamond films³, diamond has not been considered as a feasible component of most electronic devices. Furthermore, electrical characterization of diamonds has been hindered by the lack of compositional information on the natural diamonds available for study and by those diamonds' low dopant level. GE has developed a technique to synthesize gem-quality diamonds⁴, more highly doped with boron than any natural diamonds yet discovered. The enhanced conductivity and presumably known components of the new synthetic diamond make it an ideal subject for STM and complementary surface techniques.

This thesis addresses some of the complexities of STM imaging on carbon surfaces and on adsorbates. This and other surface techniques are also used to understand the surface characteristics, composition and electronic properties of a synthetic, boron-doped diamond.

Review of the Technique

Although the principles of the STM technique are becoming common knowledge to the scientific community, a review of basic theoretical principles is useful. An explicit description of the experimental details for the particular ultrahigh vacuum (UHV) system used for all STM imaging and spectroscopy in *Chapters 3 and 4* of this thesis is also presented.

³P. K. Bachmann and R. Messier *Chem. and Engrng. News*, May, 24 (1989)

⁴F. P. Bundy, H. T. Hall, H. M. Strong and R. J. Wentorf, Jr. *Nature* 176, 51 (1955)

Basic Theory

In order to grasp the complexity of interpreting STM imaging and spectroscopy, a basic understanding of the physical principles involved in this technique is necessary. Excellent basic reviews of STM theory have been published⁵ and will serve to enhance the simple explanation provided here. Ideally, a conducting tip with an atomically sharp point is positioned within a few tens of angstroms of the surface to be studied. When a small electric potential bias is applied to the sample, electrons will tunnel quantum mechanically without loss of momentum from the sample to the tip (negative bias) or from the tip to the sample (positive bias). The technique's exquisite resolution is due to the exponential dependence of the tunnel current on the separation between the tip and sample;

$$I \propto \exp(A\sqrt{\phi} s), \quad (1)$$

where $A=1.025 \text{ V}^{-1/2}\text{\AA}^{-1}$, ϕ is the barrier height to tunneling (often estimated as the average work function between tip and surface), and s is the tip-sample separation. For example, for a typical barrier height of 5 V, the current will change by a factor of 10 for a single angstrom change in separation.

The STM is a highly unique probe in that it is local both spatially and electronically. A more detailed examination of the tunnel current between a tip of finite radius and a surface⁶ shows that the current is proportional to the tunneling conductance, σ , where

$$\sigma \propto \rho(r_t, E_F) = \sum_v \left| \psi_v(r) \right|^2 \delta(E_v - E), \quad (2)$$

and $\rho(r_t, E_F)$ is referred to as the local density of states (LDOS), r_t is the position of the center of curvature of the tip relative to the surface, ψ_v are the surface wave functions at the energy E_v , and E_F is the Fermi energy. The spatial dependence of current on distance is contained within the exponential decay of the surface wave functions into the gap, and the energy dependence is

⁵P. K. Hansma and J. Tersoff *J. Appl. Phys.* 15 (2), R1-R23 (1987), and A. Baratoff *Physica* 127B, 143-150 (1984)

⁶J. Tersoff and D. R. Hamann *Phys. Rev. B* 31, 2 (1985)

described by the extent of wave function amplitude at a given energy. Thus, as a tip is scanned across the surface at a constant current, it traces contours of constant LDOS that are dependent on both the established bias energy and tip position above the surface.

Data Collection

The data for images are taken by rastering the tip across the surface in x and y while measuring some function $z(x,y)$. The most common STM image presented is a topographic image (constant current image or slow scan). In this data collection method, the z measurement is the voltage applied to the z piezo by the feedback circuit to move the tip in order to keep the current constant. Since the current is exponentially dependent on the distance away from the surface, this measurement is very sensitive and provides an image of the surface topography. However, because the current is sensitive not only to distance but also to energy density of states effects, topographic images are convoluted with the effects of the electronic structure of the surface as discussed in the previous section.

Another common method of acquiring images provides current images (fast scan). The tip is rastered over the surface at a rate faster than the feedback response so that an average "height" above the surface is maintained. The measured current is plotted as a function of x and y in the resultant images. An explanation and illustration of these two imaging modes can be found in **Figure 1** of *Appendix A*.

The UHV system is fully digitized with computer-driven menus and data storage. Only the current feedback loop is controlled by an analog amplifier to increase the bandwidth and reduce digitization noise. Implementation of the computer and signal converters along with the detailed design of the Caltech UHV-STM system is explained in Reference 7.

Barrier Height Measurements

From the basic theory of Equation 1, it is clear that $d\ln I/dz$ is proportional to the square root of the barrier height. Local barrier height images are obtained by applying a 1kHz, small voltage modulation to the z

⁷John A. Kramar Ph. D. Thesis 'Tunneling Microscopy and Spectroscopy of Molybdenum Disulfide' California Institute of Technology, 1990

piezo, where z is the direction perpendicular to the surface. Consequently, the tip-sample distance is modulated at a frequency higher than the feedback bandwidth so that an average tunnel current is maintained while taking a normal topographic image. The modulation voltage (distance) can be chosen for each image, but usually varies from 10 to 100 mV (~ 1 to 10 Å). The derivative $d\ln I/dz$ is measured with a lock-in amplifier at the modulation frequency. These images are subject to less noise than topographic images because the ac detection technique has an inherent increase in signal-to-noise⁸.

Although barrier height images are occasionally referred to as work function images, the latter term is misleading. Since the work function is defined for infinite separation between tip and sample, it has a value dependent on the entire surface. The STM technique requires a measurement of a change in tunnel current for a given, small modulation distance of the tip-sample separation. As a result, the barrier height is a highly localized measurement, again in both space and energy, which complements the topographic images. Further discussions of the barrier height measurements are presented by Binnig and Rohrer⁹ and in the context of *Chapter 3*.

The barrier height measurements presented in this thesis are taken at 1kHz with the z modulation amplitude indicated in the images. For both the barrier height images and topographic images, the pixel density matrix is 500 points in x and 100 points in y . Depending on the size of the image taken, the resolution scales accordingly. In high-resolution images, such as a typical 50 Å/side image shown in *Chapter 3*, the resolution in x (10 points/Å in the example) and y (5 points/Å) is much better than atomic spacing. All topographic and barrier height images are scanned both in the forward and reverse directions across the same x and y positions and stored as separate images, which are then compared to verify reproducibility of the scan lines. Use of both forward and reverse scans also provides a good test for low-frequency noise that often appears as atomic-sized corrugation.

⁸B. Marchon, P. Bernhardt, M. E. Bussell, G. A. Somorjai, M. Salmeron and W. Siekhaus *Phys. Rev. Lett.* 60 (12), 1166 (1988)

⁹G. Binnig and H. Rohrer *IBM J. Res. Develop.* 30 (4), 355 (1986)

Current-Voltage Spectroscopy

Spectroscopy with the STM is often performed to further investigate the nature of the surface under study. The most common STM spectroscopy is current *versus* voltage (IV) spectroscopy. The tip is held at a constant height above a given x,y position on the surface. The feedback to the z piezo is temporarily paused (typically ~5ms), the voltage is swept through a given range and the resultant current is measured. Feedback is then reestablished. Although the IV curves have a distance dependence defined by the parameters established before breaking feedback, information can be gained about both filled and unfilled states regardless of the sign of the original bias set point. The normalized conductance ($\frac{dI}{dV} \times \frac{V}{I}$) is often plotted as a function of voltage as it has been shown¹⁰ to correlate directly to the local density of states with little z dependence. Although the tip structure has been shown to have little effect on the IV spectra for some systems¹¹, the nature of the tip electronic structure probably affects the spectroscopy of most tip-surface combinations.

When examining semiconductors, the unit-cell averaged IV data can be quite useful for simple confirmation of *n*- or *p*-type character¹² or more complicated calculations of band-bending¹³ and Fermi level pinning¹⁴. In all of the IV's in this thesis, > 400 IV's were averaged over the area probed by the tip in the time taken to collect all the data, typically 15-30 seconds. Consequently, the IV's presented are unit-cell averaged and represent an area over which the tip drifted during acquisition time (~1-5 Å).

Image Processing and Presentation

The images in all chapters, excluding *Chapter 2*, which is self-contained, are presented in one of three forms: line scans, gray-scale or 3-dimensional rendering. All images are first leveled by a background planar subtraction. Line scans are shown as *x versus y+z*, where each successive line

¹⁰J. A. Stroscio, R. M. Feenstra and A. P. Fein *J. Vac. Sci. Technol.* **A 5** (4), 838 (1987)

¹¹W. J. Kaiser and R. C. Jaklevic *IBM J. Res. and Develop.* **30** (4), 411 (1986)

¹²W. J. Kaiser, L. D. Bell, M. H. Hecht and F. J. Grunthaner *J. Vac. Sci. Technol.* **A 6**, 519 (1988)

¹³L. D. Bell, W. J. Kaiser, M. H. Hecht and F. J. Grunthaner *Appl. Phys. Lett.* **52** (4), 278 (1988)

¹⁴H. Salemink and O. Albrektsen *J. Vac. Sci. Technol.* **B 9** (2), 779 (1991)

in y is offset from the line beneath. The gray-scale images are presented in 256 levels where white (bright) always represents higher topographic distance or higher values (such as current or barrier height). Three-dimensional rendering is accomplished by filling the space between the lines in a line scan and adding shading or lighting by taking the slope rather than the height to add brightness. Smoothing of the data is possible by a simple, weighted average and is indicated if performed.

The images are stored with file names and a given extension: .DAT, .REV, .HDR, .WFD and .RWF for the forward, reverse, header, barrier height, reverse barrier height data, respectively. For all UHV images presented in this thesis, the file name is inserted in parentheses after the figure number and in the figure caption so that future analyses or reference can be facilitated.

SUMMARY OF CHAPTERS

The thesis is organized in four Chapters and two Appendices. Although each chapter contains a complete set of experiments and results, the chapters all involve the technique of Scanning Tunneling Microscopy and Spectroscopy and the attempt to understand the basic mechanisms of imaging. The final chapter extends the technique to a more basic study of a carbon surface and utilizes a number of different techniques to complement the STM work.

Chapter 2 presents a detailed study of the highly oriented graphitic carbon surface performed in air. Since HOPG has become the standard surface used to calibrate and test new STM's, this chapter, while applicable to all environments, is especially relevant to atmospheric STM work. A mechanism is proposed for the commonly observed enhanced stability in imaging layered compounds such as HOPG. The proposed multiple-tip imaging is able to account for a number of anomalies observed in numerous research laboratories on graphite surfaces. The details of the atmospheric STM used for this study, imaging and spectroscopy data collection, and data presentation are described in *Appendix A*.

In *Chapter 3*, the preparation of a clean, Si(111) (7x7) surface as a substrate for small, organic molecules is discussed. Because the interest in imaging biological molecules is growing, the need to understand the contrast mechanism in these images is imperative. This chapter addresses the

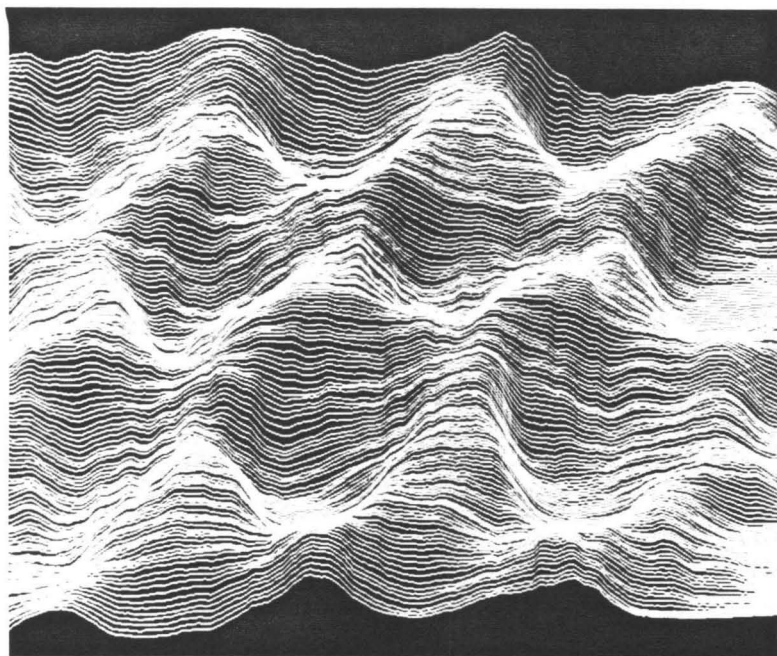
preliminary work: the design and testing of apparatus suitable for heating the Si(111) surface to atomic cleanliness. Two heater designs are presented with a discussion of their advantages and disadvantages. The necessary precautions for preparing the silicon, and results of heating the surface and examining it by STM are presented and discussed. Furthermore, the observation of the $R30^\circ (\sqrt{3} \times \sqrt{3})$ surface reconstruction of boron on Si(111) is also presented as both topographic and barrier height images. This reconstruction is interpreted and discussed both in regard to the topography and to the relationship between the information obtained from the two imaging modes.

Chapter 4 presents an integrated examination of the composition, surface morphology and electronic properties of a synthetic, boron-doped gem-quality diamond by STM, X-Ray Photoelectron Spectroscopy (XPS), Ion Microprobe analysis, optical goniometry and Laue diffraction. Compositional analyses and spectroscopy reveal the nature of the more prevalent impurities and their effect on the current-voltage curves observed. New surface features are presented in addition to a comparison of the spectroscopy of an unpinned and a pinned Fermi level on the diamond surface.

Appendix B presents the STM images obtained for a gold surface to which is attached a submonolayer coverage of human serum albumin and its antibody. Because the data contain many of the features associated with the difficulty of imaging biomolecules, it is presented with a discussion of these problems, despite the inability to verify the presence of the antibody complex by alternate means.

Chapter 2

*IMAGING AND SPECTROSCOPY OF GRAPHITE IN AIR BY SCANNING TUNNELING MICROSCOPY: ROLE OF THE TIP **



INTRODUCTION

The rapid growth of Scanning Tunneling Microscopy¹ has produced the need for instrument test and calibration standards. Imaging of Highly Oriented Pyrolytic Graphite (HOPG) has become the benchmark for STM instrument test and calibration because HOPG can be readily cleaved to give large, atomically flat areas that are relatively clean and inert. In addition, atomically resolved images of HOPG are easily attained in air and liquid as well as in high vacuum. However, researchers have observed numerous anomalous characteristics of the graphite surface, including the following:

- 1) low barrier heights
- 2) large distance dependencies
- 3) giant atomic corrugations up to 2.4 nm
- 4) enhanced spatial resolution of about 0.1 nm
- 5) absence of surface defects
- 6) asymmetric/changing images

In order to explain some of these anomalies, tip-surface contact through a contamination layer and/or surface-tip deformation has been proposed. By invoking a tip-contamination-sample contact mechanism, Coombs and Pethica² assert that the nonconducting contamination causes elastic deformation of the surface. As a result, the anomalously low barrier heights and large distance dependencies can be explained. Elastic deformations³ and contamination-mediated deformations⁴ have also been invoked to explain giant corrugations. Pethica⁵ has proposed an STM image contrast source of sliding graphite planes under the tip, which results in a

*This chapter is a combination of two published papers and some additional information not contained within. The original papers are: R. J. Colton, S. M. Baker, W. J. Kaiser and J. D. Baldeschwieler *Appl. Phys. Lett.* **51** (5), 305 (1987), and R. J. Colton, S. M. Baker, R. J. Driscoll, M. G. Youngquist, W. J. Kaiser and John D. Baldeschwieler *J. Vac. Sci. Technol.* **A6** (2), 349 (1988)

¹G. Binnig and H. Rohrer, *Helv. Phys. Acta.* **55**, 726 (1982), and G. Binnig, H. Rohrer, Ch. Gerber, and E. Weibel, *Phys. Rev. Lett.* **50**, 120 (1983)

²J. H. Coombs and J. B. Pethica *IBM J. Res. Develop.* **30**, 455 (1986)

³J. M. Soler, A. M. Baro, N. Garcia, and H. Rohrer *Phys. Rev. Lett.* **57**, 444 (1986)

⁴H. J. Mamin, E. Ganz, D. W. Abraham, R. E. Thomson and J. Clarke *Phys. Rev. B* **34**, 9015 (1986)

⁵J. B. Pethica *Phys. Rev. Lett.* **57**, 3235 (1986)

variation in total conductivity dependent on the lattice registry. Enhanced spatial resolution could be a consequence of the electronic structure of graphite for which the Fermi surface collapses to a point at each corner of the surface Brillouin zone⁶. This chapter addresses the absence of surface defects and unexpected images (hexagonal rings, dots, rows) that have not been adequately addressed.

While most STM experiments to date have focussed on the preparation and cleaning of the surface to be analyzed, the tip preparation and cleaning procedures have been qualitative at best. The exact role of the tip structure in STM is still an unresolved question. The sharpness of the tip is believed to be one factor affecting the resolution of the STM image⁷. Although various studies of the tip structure and STM image have been endeavored^{3,8}, correlation between the actual geometry and experimental STM results has still not been fully established. STM tips have been fabricated from metal wires such as tungsten (W) and platinum (Pt) that can be electrochemically etched⁹ or sharpened to achieve a radius of curvature less than 100 nanometers. While the etching procedure is straightforward and the resultant tips are fairly reproducible, the tip composition can vary depending on the purity of the starting material and contamination from the air and electrochemical bath. The usual contaminants are metal oxides, organic adsorbates, and alkali metal salts.

Processing of prepared tips includes field desorption/evaporation, indirect electron bombardment, sputtering and annealing¹⁰ or controlled (or uncontrolled) tip crashes against the surface^{11,12}. These procedures may crack the native oxide, transfer materials from the surface to the tip, or reform the atomic structure of the tip in such a way as to attain an atomically resolved STM image. However, the image is often short-lived because of the delicate and seemingly dynamic structure of the tip. Currently, a good tip is merely

⁶J. Tersoff *Phys. Rev. Lett.* **57**, 440 (1986)

⁷A. Baratoff *Physica* **127 B**, 143 (1984).

⁸G. F. A. Van de Walle, H. van Kempen and P. Wyder *Surf. Sci.* **167**, 219 (1986)

⁹G. Binnig, H. Rohrer, Ch. Gerber and E. Stoll *Surf. Sci.* **144**, 321 (1984)

¹⁰J. E. Demuth, R. J. Hamers, R. Tromp and M. E. Welland *J. Vac. Sci. Technol. A* **4**, 1320 (1986)

¹¹G. Binnig and H. Rohrer *Helvetica Phys. Acta* **55**, 726 (1982)

¹²J. Schneir, R. Sonnenfeld, P. K. Hansma and J. Tersoff *Phys. Rev. B* **34**, 4979 (1986)

defined as one that gives a highly resolved image without reference to the actual tip structure.

The role of the tip in imaging of HOPG has been discussed with regard to the methods required to produce a functioning tip. By crashing the tip repeatedly against the surface, Hansma¹² claims to have developed a "tip cleaning" method. Sometimes, however, merely waiting a sufficient amount of time allows for atomic imaging. In either instance, the possibility of creating a tip with a graphite flake or graphite contamination exists. With these tip-surface interactions in mind, investigations of the interaction of a graphite tip with the HOPG surface were started.

Because an oxide-free tip would be ideal for use in STM (oxide contamination creates an insulating layer that is highly uncharacterizable when determining tunneling barrier heights), an STM tip that has very little native oxide and is highly resistant to air oxidation has been developed. An investigation of the mechanism for the enhanced resolution of STM images of HOPG¹³ is performed. In the process of simulating tunneling between two (sliding) graphite planes^{3,5} it was discovered that using a pencil lead as the tip readily produces atomically resolved STM images of HOPG. With the graphite tip, the questions of sliding graphite planes and graphite tip contamination can be addressed. In this chapter, further studies of the role of the tip in imaging HOPG are reported. In addition, the tip material is readily available and extremely inexpensive. The tip does not require sharpening or etching to produce atomically resolved STM images of highly oriented pyrolytic graphite (HOPG). The tip is fabricated from the lead of a mechanical pencil that consists mainly of graphite.

Analyses of the tip composition and structure were performed in order to characterize the tips. Images were obtained as a function of tip-sample separation, and IV characteristics of the tunneling junction were also measured. Conductance curves were plotted in order to determine gap resistances. The results of spectroscopic studies of tip-surface interactions and computer simulations of sliding graphite planes and multiple tips suggest a point-contact imaging mechanism. In this model, contact occurs between the tip and sample such that either a contamination layer or an actual tip-sample contact provides an alternate current source. This alternate mechanism for

¹³R. J. Colton, S. M. Baker, W. J. Kaiser and J. D. Baldeschwieler *Appl. Phys. Lett.* (1987)

current generation becomes convoluted with the current that is exponentially dependent on distance. Both current sources can arise from one or multiple tunneling tips.

EXPERIMENT

Preparation of Oxide-Free Tips

Tungsten tips were prepared using either an ac or dc electrochemical etching procedure⁹. The graphite-coated tips were made by dipping tungsten tips into a colloidal graphite suspension¹⁴. The graphite tips were standard mechanical pencil lead¹⁵. X-ray diffraction measurements were done on powdered pencil lead and on a colloidal graphite-coated glass slide. XPS spectra were obtained with a Surface Science Laboratories SSX 100-03 spectrometer using a monochromatized Al K α X-ray source (1486.6 eV). EDAX and TEM were done on a JEOL 430 transmission electron microscope using copper grids.

Microscopy and Spectroscopy

The experiments were done on an HOPG¹⁶ sample in air using an STM, which is described by Kaiser and Jaklevic¹⁷ and detailed in *Appendix B*. Images were obtained in the current imaging mode with typical tip-scanning frequencies of 250 Hz in x and 5 Hz in y; the voltage applied to the z piezo was held constant. Images were displayed on a variable-persistence oscilloscope and recorded on video tape. Selected images were digitized into 320 x 200 pixels with four gray levels¹⁸. The images were then smoothed into 256 gray levels with a 15 x 15 pixel sliding-window average; the image resolution was not a function of window size even for somewhat larger windows. Images presented here are photographs of smoothed data displayed on a graphics monitor¹⁹.

¹⁴Aquadag Colloidal Graphite, Ted Pella, Inc., Tustin, CA

¹⁵Pentel, 0.5mm HB

¹⁶HOPG was supplied by A. R. Moore, Union Carbide Corporation

¹⁷W. J. Kaiser and R. C. Jaklevic *Rev. Sci. Instrum.* 59(4), 537 (1988)

¹⁸Lodge Electronics Image Ace II Video Capture System

¹⁹Monitronix MX-200 Color Monitor via a Vectrix PEPE graphics controller. C. Bai, J. Kramar and M. Weimer, California Institute of Technology were responsible for the original graphics display software

The IV curves were obtained with constant voltages applied to the x, y, and z piezos. Bias voltage control and data acquisition were under microcomputer control²⁰. The output of a differential amplifier was monitored to measure the voltage of the sample relative to the tip, and the voltage drop across a resistor was monitored to measure the current. In a typical experiment, 200 voltage sweeps, each with 150 data points were averaged to make one IV curve in about 20 seconds.

RESULTS AND DISCUSSION

Characterization and Analysis of Graphite Tips

The carbon tip was made by breaking a small piece of 0.5 mm diameter pencil lead just before use in the STM. Electron micrographs of a used carbon tip (obtained on an ETEC Auto Scan Electron Microscope with a 20 keV electron beam) are shown in **Figure 1**. The end of the tip is fairly blunt (**Figure 1** insert) and many times the diameter of electrochemically sharpened tungsten tips (see **Figure 3** insert). The end of tip has been magnified 2,000 times and is shown to consist of small crystallites of graphite. The exact size of the crystallite from which tunneling occurs is unknown, but the crystalline nature of the graphite in the pencil lead was confirmed by x-ray diffraction.

The surface composition of the pencil lead determined by x-ray photoelectron spectroscopy (XPS) is given in **Table I**. The tip is composed mainly of carbon and smaller amounts of oxygen and silicon. The carbon exists in at least two distinct chemical states: One carbon species has a photoelectron binding energy of 284.6 eV that is due to carbon bonded to carbon (C-C), or graphitic carbon; the other carbon species has a photoelectron binding energy of 285.7 eV that is due to carbon singly bonded to a hydroxyl group (C-OH). The C-C:C-OH ratio is around 12:1. The oxygen species is only weakly observed as a broad asymmetric peak with a photoelectron binding energy centered around 532.0 eV. The lower binding-energy oxygen species is probably due to oxygen bonded to silicon. The higher binding-energy oxygen species is due to the hydroxyl oxygen that is bonded to carbon. The silicon

²⁰The Scientific Solutions DADIO and the Data Translation DT2821 analog and digital I/O boards installed in a Sperry PC/IT Personal Computer were used for bias voltage control and data acquisition, respectively.

species is present in an oxidized form probably associated with the clay used to make pencil leads. This tip has a relatively low oxygen content, where the C:O ratio is around 15:1 and should be extremely resistant to further oxidation. The presence of silicon was confirmed by Energy Dispersive Analysis of X rays (EDAX).

The carbon and oxygen content of the pencil lead is similar to that found for HOPG that had been cleaved and stored in air (see **Table I**). In fact, the photoelectron spectra of the pencil lead and HOPG look very similar. In addition to the low oxygen content, the carbon tip should be extremely resistant to further oxidation, particularly at room temperature²¹.

The surface composition of the colloidal graphite is also given in **Table I**. The colloidal graphite is composed mainly of carbon and smaller amounts of oxygen and nitrogen. This graphite has a C:O ratio of around 6:1, corresponding to a higher oxygen content than found in the pencil lead. This higher oxygen content is due primarily to a higher concentration of the oxidized carbon species with a photoelectron binding energy of 286.1 eV. The C-C:C-OH ratio is around 5:1 compared to 12:1 for the pencil lead. The higher oxygen content is also due to a measurable amount of adsorbed water. The observed nitrogen is presumably due to atmospheric contamination or to a nitrogen-containing species used in the formulation of the colloidal graphite.

Table I: **Composition of Graphite Tips Determined by X-Ray Photoelectron Spectroscopy**

Elemental Composition (atomic percent)				
<i>Tip Material</i>	<i>Carbon</i>	<i>Oxygen</i>	<i>Other</i>	<i>C/O Ratio</i>
Pencil Lead	89	6	5 (Si)	~15:1
Colloidal Graphite	84	13	3 (N)	~ 6:1
HOPG	93	7	--	~13:1

X-ray diffraction confirms the graphitic composition in both the pencil lead and the colloidal graphite. TEM images of the pencil lead showed jagged edges of protruding graphite planes. The graphite-coated tungsten (W) tip, on the other hand, has a continuous coating of randomly oriented graphite

²¹W. N. Reynolds **Physical Properties of Graphite** (Elsevier Publishing Co, Ltd.: New York) 1968

greater than 5 nm thick. Edge fringes of aligned graphite are evident on both the tip and the colloidal graphite alone.

The colloidal graphite appears to coat the tip easily to produce a relatively thick film with good adhesion. It is speculated that the random alignment of the graphite allows for realignment of the sheets upon contact with the HOPG surface (possible sliding planes) and provides a mechanism for deformation of either the sample or the tip coating. As the tip is pushed into the sample, more colloidal graphite comes into contact with the HOPG. The jagged edge of the pencil lead could also have successively more contact and possibly produce multiple tunneling tips as the tip moved toward the sample.

Imaging Results with Oxide-Free Tips

The STM image of HOPG shown in **Figure 2** was obtained with the pencil-lead carbon tip. The instrument that was used is described elsewhere²². These results were collected in the fast scan mode at room temperature in air and with the feedback circuit disabled. The scan speed of the tip was 250 Hz in the x direction and 5 Hz in the y direction, which produces five images/second. The images were recorded from the screen of a variable persistence oscilloscope by a VCR. The image shown in **Figure 2** (and **Figure 4**) is a photograph of a single VCR frame of the CRT display monitor. The images were not filtered. The size of the image in **Figure 2** is $\sim 2.1 \text{ nm} \times 1.2 \text{ nm}$. The sample-tip bias was about 100 mV and the peak-to-valley variation in tunneling current is about 4 nA, while the average value is about 10 nA.

In addition to the development of the carbon (pencil lead) tip, a tip-repair method that restores used or damaged tungsten tips and enables them to produce atomic images of HOPG has been developed. The method involves coating a used tungsten tip with graphite. In practice, the used tungsten tip is dipped into the colloidal suspension of graphite in water. Alternately, a tip that is already mounted in the STM is coated using a capillary tube filled with the colloidal graphite.

Figure 3 shows electron micrographs of a used AC-etched tungsten tip coated with colloidal graphite. A bend in the end of the tungsten tip is clearly visible (see insert) and was formed when the original tip made contact with

²²W. J. Kaiser and R. C. Jaklevic *Surf. Sci.* **181**, 55 (1987)

the surface. The colloidal graphite coating on the end of the tip appears relatively featureless and much smoother than the surface of the pencil lead (compare **Figures 1** and **3** -- note the equivalent scales). X-Ray diffraction confirmed the crystalline structure of the colloidal graphite coating.

Figure 4 shows an STM image of HOPG obtained after coating a used tungsten tip with the colloidal graphite. The uncoated tungsten tip could not produce an image of HOPG. The size of the image is around $1.5 \text{ nm} \times 0.9 \text{ nm}$. The sample-tip bias is about 20 mV and the peak-to-valley variation in the tunneling current is about 3 nA, while the average value is about 48 nA. The scan parameters are equivalent to those described for **Figure 2**.

Repetitive testing has never failed to achieve atomically resolved STM images of HOPG using either the pencil lead or colloidal graphite-coated tips upon the initial approach. Tip "crashing" is not required to obtain these images. The mechanism by which these tips interact with the HOPG surfaces to produce these highly resolved images of HOPG will be discussed later in this chapter.

The advantages of these tips are numerous: Atomic resolution is readily attained with a graphite tip. A nonimage producing tungsten tip can be easily restored to a functioning tip. Because of the graphitic composition, the tips are relatively oxide-free and resistant to further oxidation. In the case of imaging HOPG, these tips may also present a higher area of surface contact, which may allow for more rigidity and better image quality. The disadvantages of these tips may include limited applicability and the possibility of having multiple tunneling points that distort the image.

Effect of Tip Geometry and Orientation on the Image of HOPG

As mentioned above, most models use sample-tip contact to explain the anomalous tunneling behavior of graphite. In Pethica's model proposing the sliding of graphite planes under the tip, fluctuations in the total conductivity between the tip and sample occur as the planes pass in and out of registry. In order to simulate this contrast mechanism, a computer model was developed²³ that scans a single or multiatom tip over a large plane of graphite while summing the electron charge density at each tip atom. The

²³Primary computer modeling was performed by Dr. Rich Colton, Visiting Scientist at Caltech (1987)

graphite surface is represented by a hexagonal array of 77 atoms that has the appropriate C-C bond length for graphite, i.e., 0.142 nm. Each atom is surrounded by a spherically symmetric electron cloud derived from the hydrogen 1s wave function in order to simulate an exponentially decaying charge density.

The tip has been modeled with several different structures consisting of single or multiple atoms. The multiatom tip shown in **Figure 5a** represents a small, trigonally symmetric plane of graphite. The center atom of the tip is 0.142 nm away from the three outer atoms. As the tip is scanned over the graphite surface, the tip atoms go in and out of registry with the surface atoms. A single-atom tip or a trigonally symmetric, 3-atom tip (the tip shown in **Figure 5a**, but without the center atom) produces an image of the surface consisting of hexagonal rings where each of the six atoms in the ring has the same electron density. The trigonally symmetric, 4-atom tip shown in **Figure 5a** produces, however, a trigonally symmetric image where only three of the carbon atoms in the hexagonal ring have the same electron density. This image is commonly observed by STM for graphite and is believed to represent the correct surface structure of graphite²⁴. The experimental gray-scale images shown in **Figure 5a** show a ring structure (bright or raised area) around an hexagonal arrangement of holes (dark areas). The line drawing of the same image shows more clearly the arrangement of the trigonally symmetric atoms as they alternate in height around the hexagonal ring.

Rotating the trigonally symmetric tip between 0 and 60 degrees with respect to the surface plane produces other trigonally symmetric features such as triangles or clovers arranged in a hexagonal pattern. The formation of a row-type pattern (horizontal, vertical, or diagonal) never appears when trigonally symmetric tips are used in the model.

Making the tip structure asymmetric (with respect to the graphite lattice), as shown in **Figure 5b**, causes the computer-generated image to become less symmetric; and if the plane of the tip atoms is rotated parallel to the plane of the surface atoms, the image collapses into differently shaped rows. The image in **Figure 5b** was formed by deleting two atoms from the symmetric, 4-atom tip and rotating the tip by 40 degrees. The resulting image produces a staircase of diagonal rows. Diagonal rows are also observed in

²⁴S.-I. Park and C. F. Quate *Appl Phys Lett.* **48**, 112 (1986)

STM images of graphite as illustrated by the experimental images also shown in **Figure 5b**.

Row-type images can also be generated by placing two or more "tunneling" tips at arbitrary points in the plane above the surface. In fact, row-type images were also observed by placing two randomly oriented, trigonally symmetric tips in a plane above the graphite surface. A series of tips and their corresponding experimental images are shown in **Figures 5c-5f**. Two images that were not observed in the Caltech atmospheric system are also included in **Figures 6a and 6b**.

These observations support the premise that the different image patterns observed for graphite by STM can be explained by the presence of multiple tunneling tips. Some of the images obtained using the graphite tips described in this chapter show clear evidence for multitip tunneling.

Point-Contact Imaging

Spectroscopy measurements were performed to study the graphite imaging mechanism in air, which is based on contact between tip and sample directly or through a contamination layer. Since the graphite is deformable, the tip will push through any surface contamination until a current can be obtained as shown in **Figure 7**. A series of images was obtained using a graphite-coated tungsten tip on an HOPG surface for four tip positions (R_0) within the tunneling region. **Figure 8** shows the images obtained at a) upper-mid, b) lower, and c) bottom regions of the gap. The position of the tip is reported as Δz relative to the point at which tunneling is first detected ($R_0 = \text{inf}$). Current-voltage (IV) curves (see insets) were obtained while scanning in the current-imaging mode in order to correlate image quality with the IV characteristics at different gap widths.

Anomalous tip-sample separation dependence on tunnel current is observed over a Δz range greater than 20 nm. This observation would suggest that the z-piezo movement is not equivalent to the gap change and that a model involving elastic deformation of the HOPG surface or the tip is probable. The data in **Figure 8** show that the spectra taken at the top and upper-mid (a) portions of the gap exhibit the familiar IV curve shape with exponential tails at higher voltages, while those at the lower (b) and bottom

(c) portions show a linear dependence indicative of ohmic contact between the tip and sample.

Image quality is highly dependent on the R_0 value. Images cannot be maintained at the top of the tunneling gap because of noise and instability in the tunneling current. Although the peak-to-valley variation in current (image contrast) decreases from 0.5 ($\Delta z = 8.5$ nm) to 0.2 nA ($\Delta z = 23.5$ nm) from upper-mid to bottom gap, the image quality improves considerably. Images obtained at lower R_0 values are consistently stable and are atomically resolved. Imaging in this regime is surprising because at least part of the tip is in ohmic contact with the surface. Similar results have been obtained using tungsten and graphite tips. These observations suggest that the tip and sample are in contact (point-contact imaging), and an additional mechanical stability is established, which reduces the effect of vibrations on the STM. In addition, a conduction mechanism other than tunneling is necessary to explain the decreased contrast.

Point-Contact Spectroscopy

The voltage dependence of the tunneling current is exhibited in the shape of an I-V curve and is a probe of the local electron density of states (LDOS). Depending on the polarity of the applied voltage, either empty or filled states of the sample are detected: $V < 0$, occupied states; $V > 0$, unoccupied states. The inverse of the slope of the IV curve through zero bias is the gap resistance R_0 of the tunnel junction. Often, the first derivative spectrum, dI/dV vs V , or conductance curve (GV), is reported. For small bias potentials, since the barrier height is independent of V , dI/dV is a measure of the tunnel probability of the electron. The shape and nature of the conductance curve reflect the width, height, and shape of the potential barrier. However, interpretation of such data is not straightforward.

In order to study the IV relationships for the HOPG surface with tungsten, graphite-coated tungsten and graphite tips, IV curves were taken over a range of R_0 at a single point over the surface. **Figure 9** shows three IV curves for HOPG using a graphite-coated tungsten tip at R_0 equal to 20.7 M Ω (near the top of the gap), 6.2 M Ω (mid-gap) and 0.9 M Ω (point-contact). The trend toward linearity with decreasing R_0 is consistent with theory²⁵. A low

²⁵W. R. Brinkman, R. C. Dynes and J. M. Rowell *J. Appl. Phys.* **41**, 1915 (1970)

R_0 indicates a narrow potential barrier (small gap) and predicts a sharper rise in current with voltage at low voltages. The linear characteristic at $0.9 \text{ M}\Omega$ indicates ohmic contact between the tip and sample. The other curves are asymmetric about zero bias, exhibiting a slight rectifying behavior; that is, the current is greater at a particular negative voltage than at the same positive voltage.

The inset in **Figure 9** shows the conductance curves obtained by numerical differentiation of the IV data in **Figure 9**. Two anomalous features appear: 1) The curves are nonparabolic and 2) a slight offset from zero bias at minimum conductance exists. The conductance at $R_0 = 20.7 \text{ M}\Omega$ shows an abrupt minimum with essentially linear slopes at higher voltages. The curve at $6.2 \text{ M}\Omega$ is broader. Both curves have a negatively weighted (higher current at negative voltages) asymmetry. In addition, offsets of +20 to 50 mV (to the positive side of zero bias) are typically observed.

Similar asymmetry and rectifying behavior are observed for IV curves on HOPG using graphite tips. The current-voltage and conductance curves for graphite tips at three gap resistances shown in **Figure 10** are highly asymmetric, again with a negative weighting. Compared to the curves shown in the inset of **Figure 9**, the curves are rounder at low voltages and more parabolic for positive bias voltages. The wider nature of these curves indicates a narrower, perhaps also lower barrier height. Offsets from zero bias are typically +15 to 70 mV, similar to those of the graphite-coated tungsten tips.

The spectroscopic data for a tungsten tip at three different gap resistances on the HOPG surface are presented in **Figure 11**. Although the tungsten conductance curves are also nonparabolic, they are centered close to zero bias. The negative weighting is present but less prominent than with the carbon tips.

Discussion of Spectroscopic Anomalies

The nonparabolic nature of these curves is indicative of non-exponential behavior and suggests that the conduction mechanism does not involve only tunneling. Another conduction path would be provided if the tip and surface were in contact. This may contribute a nonexponential dependence that would alter considerably the shape of the conductance curve.

Tunneling theories would no longer suffice to describe the spectroscopic curves. Tip-sample contact of some type would also help explain the low gap resistances. Although strong band structure effects are doubtful for graphite since the band structure peaks at 1.7 eV (beyond the range of our spectra), they may contribute slightly to conductance changes at lower voltages that in turn cause asymmetry in the dI/dV curves.

The minimum conductance is at a zero bias when the barrier is symmetrical, and the tip and sample have identical Fermi energies²⁴. Image forces probably do not radically affect the shape of the curve. The offset is essentially due to the difference in work functions and geometry between the tip and sample. This fact is puzzling because the tungsten tip, not the graphite-coated tungsten or graphite tip, gives the most symmetric curve with the least offset. An asymmetric curve for a graphite-tip HOPG system, however, is not very surprising considering the different natures of the graphite on the tip and the HOPG sample. These observations may be peculiar to systems involving graphite since IV curves taken on Au samples using Au tips are highly symmetric, largely parabolic curves centered at zero bias.

Rectification of a different nature has been described by Feenstra *et al.*²⁶. A positive weighting to the IV's (negative rectification) may be accounted for by the inhomogeneous electric-field enhancement that is due to the tip curvature. The field must be stronger in the vicinity of the tip with a finite radius of curvature so that the change in potential over the gap distance is greater near the tip. For a positive bias, this effect lowers the potential barrier, resulting in an increase in the tunneling current. A negative polarity increases the tunneling barrier, reducing the current. Since the observed weighting for the IV's observed on HOPG with both types of carbon tips is *negative* rather than positive, these tips probably do not have the small radius of curvature necessary for field-enhancement effect. This observation supports the hypothesis that the tip is actually pushing into the surface providing a large contact area.

Another possible explanation for the nonexponential dependence of current on voltage involves tunneling from multiple tips or multiple-current sources. This is consistent with our computer simulations that

²⁶R. M. Feenstra, J. A. Stroscio and A. P. Fein *Surf. Sci* **181**, 295 (1987)

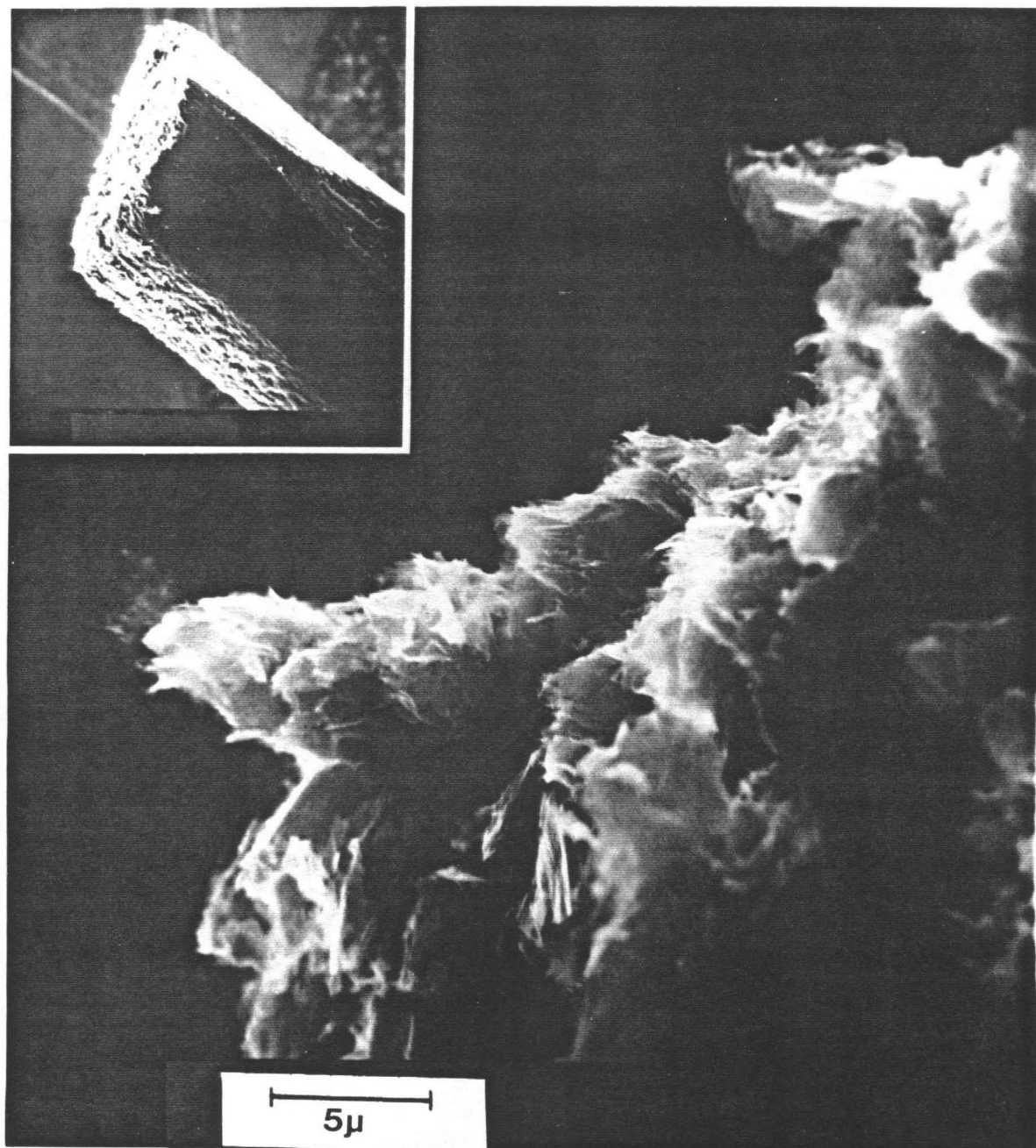
explain the image patterns created by multiple tips. The gradual change of slope in the IV curves also suggests current flow in channels other than tunneling channels. In either case, the identity of the tunneling tip was shown to affect significantly the IV characteristics of STM tunneling. These results are unlike those reported by Feenstra²⁶ or Kaiser²⁷ who did not see a contribution from the tip to the IV structure of their systems.

CONCLUSION

Atomically resolved images of HOPG in air at point contact with graphite tips have been successfully obtained. Direct contact between tip and sample or contact through a contamination layer provides a conduction mechanism in addition to the exponential tunneling mechanism. The enhanced conductance introduces an increasingly large background current at increased Δz , resulting in less image contrast. The graphite or graphite-coated tips may provide more surface area for contact with the HOPG to give higher mechanical stability, leading to quieter, more stable tunneling currents and easily reproducible, atomic images. The alignment of graphite planes upon tip-surface contact seems likely and would support Pethica's suggestion of sliding planes⁵. Furthermore, multiple tunneling tips are probably responsible for images without the expected hexagonal or trigonal symmetry. Finally, we can image HOPG without feedback control of the vertical tip position.

It is important to consider that experiments at ultrahigh vacuum where the HOPG surface is free from a contamination layer and on vibrationally stable systems most likely do not depend on this type of mechanism for atomic resolution. If the surface is free from contamination, the tip need not push through that layer. When sufficient stability of the instrument permits imaging without the added stability of point contact, atomic resolution may be obtained without crashing the tip or requiring graphite coating. These observations indicate that the use of HOPG for testing and calibration of STM instrumentation may be misleading because of the added stability of point-contact imaging.

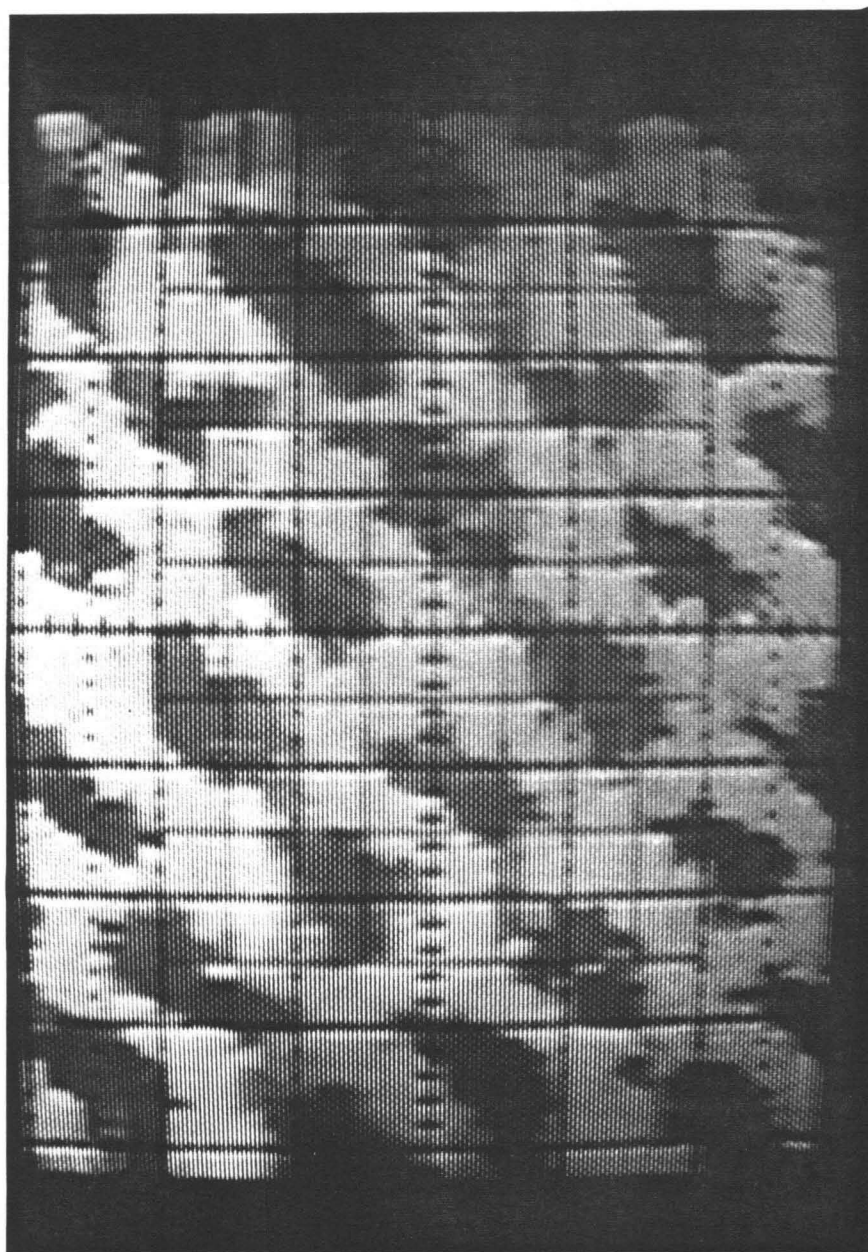
²⁷W. J. Kaiser and R. C. Jakelevic *IBM J. Res. Develop.* 30, 411 (1986)



PENCIL LEAD TIP

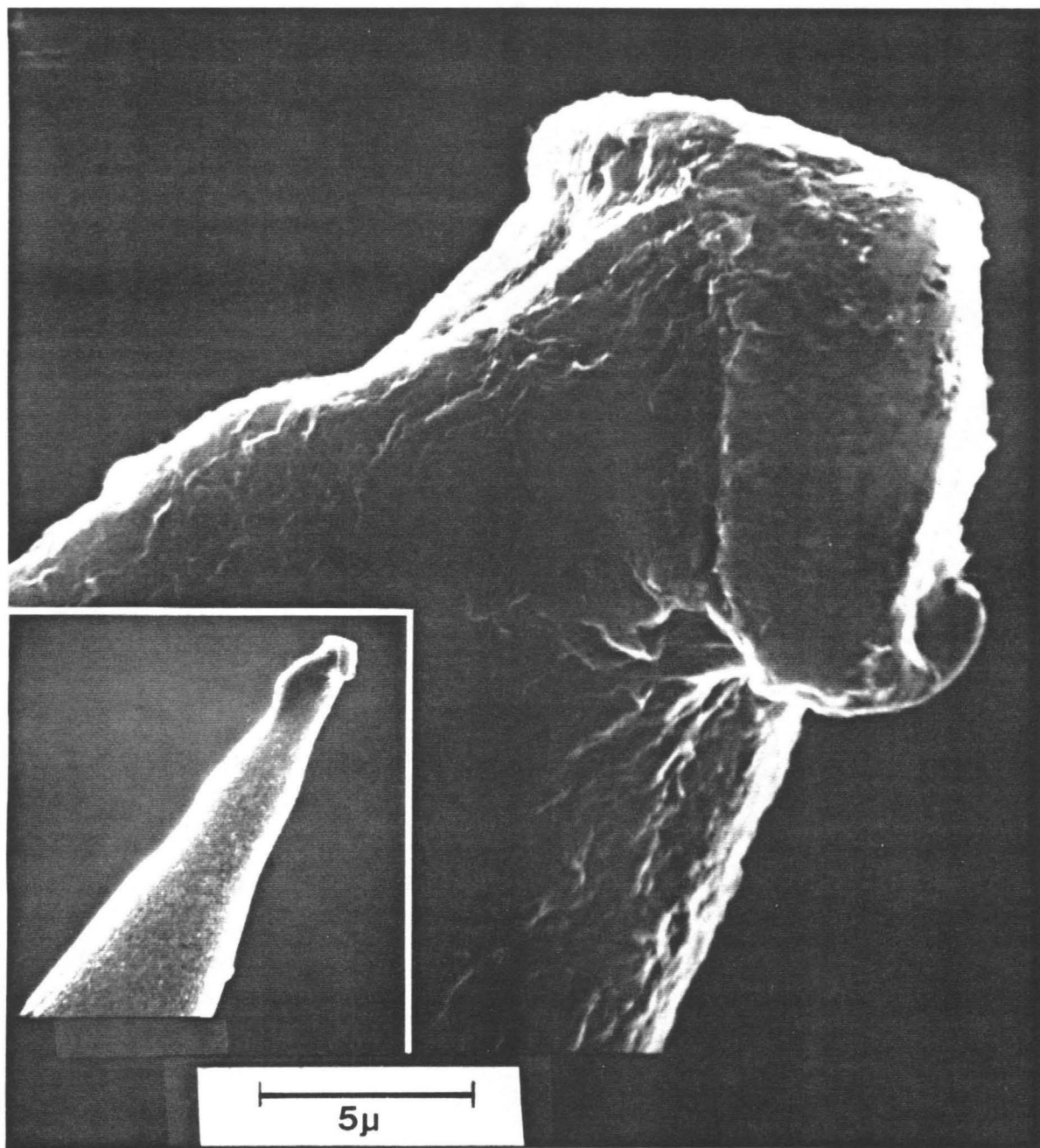
(insert is 10x less magnification)

Figure 1. Electron micrographs of a pencil lead tip magnified by 2000X (the bar scale corresponds to 1 micron). Inset shows tip magnified by 200X.



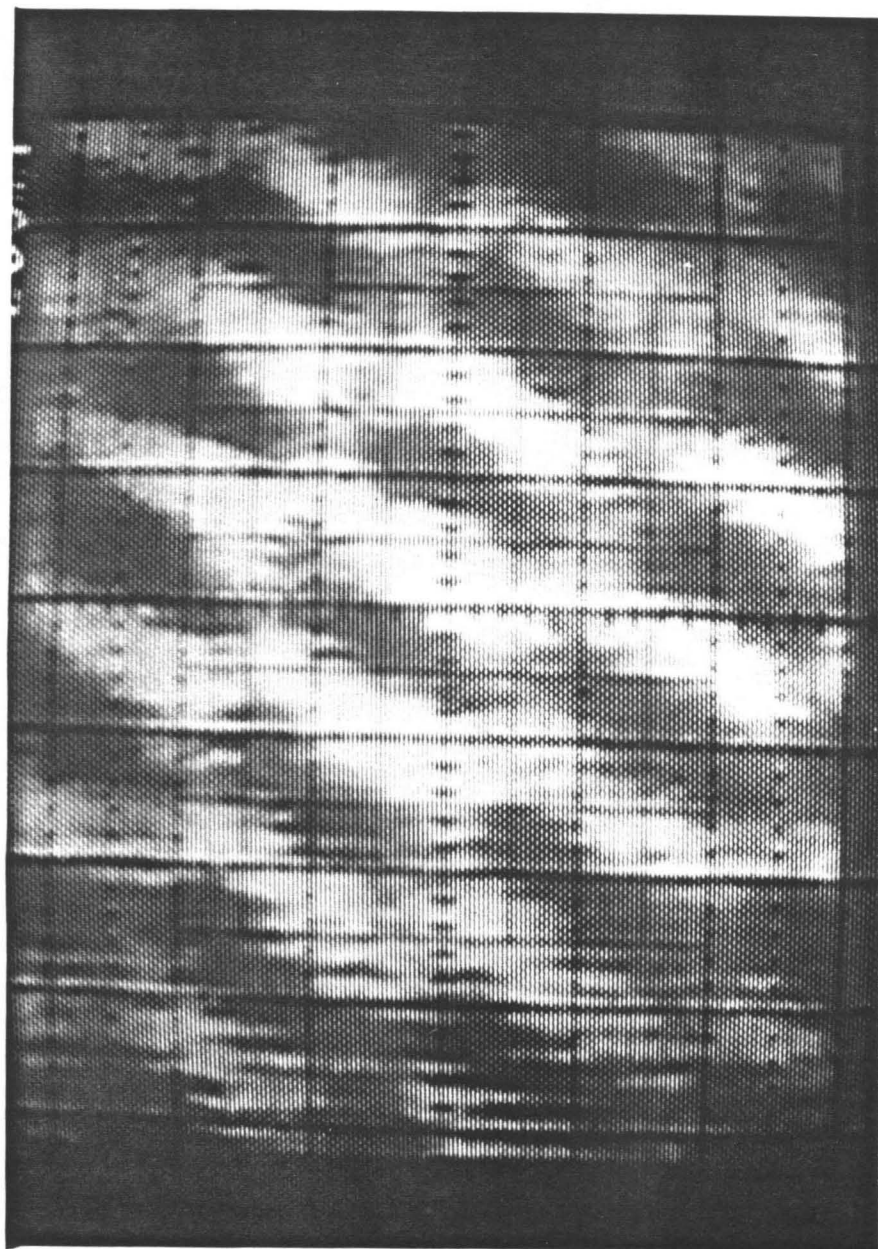
- Sample bias = -200 mV
- Tip-sample bias = -100 mV
- 2.1 x 1.2 nanometers
- Average current ~10nA

Figure 2. STM image of HOPG taken in the fast scan mode with a pencil lead tip. The sample-tip bias is 100 mV and the peak-to-valley variation in tunneling current is about 4 nA, while the average value is about 10 nA. The image size is around 2.1 nm x 1.2 nm and the sample bias is 200 mV.



**USED TUNGSTEN TIP COATED
WITH COLLOIDAL GRAPHITE**
(inset is 10x less magnification)

Figure 3. Electron micrographs of a used tungsten tip coated with colloidal graphite magnified by 2000X (the bar scale corresponds to 1 micron). Inset shows the tip magnified by 200X.



- Sample bias = -500mV
- Tip-sample bias = -20mV
- 1.5 x 0.9 nanometers
- Average current ~45nA

Figure 4. STM image of HOPG taken in the fast scan mode with a used tungsten tip coated with colloidal graphite. The sample-tip bias is about 20 mV and the peak-to-valley variation in tunneling current was about 3 nA, while the average value was about 48 nA. The image size is about 1.5 x 0.9 nanometers and the sample bias was ~500 mV.

TIP-GEOMETRY &
ORIENTATION

COMPUTER SIMULATION

EXPERIMENTAL IMAGES *

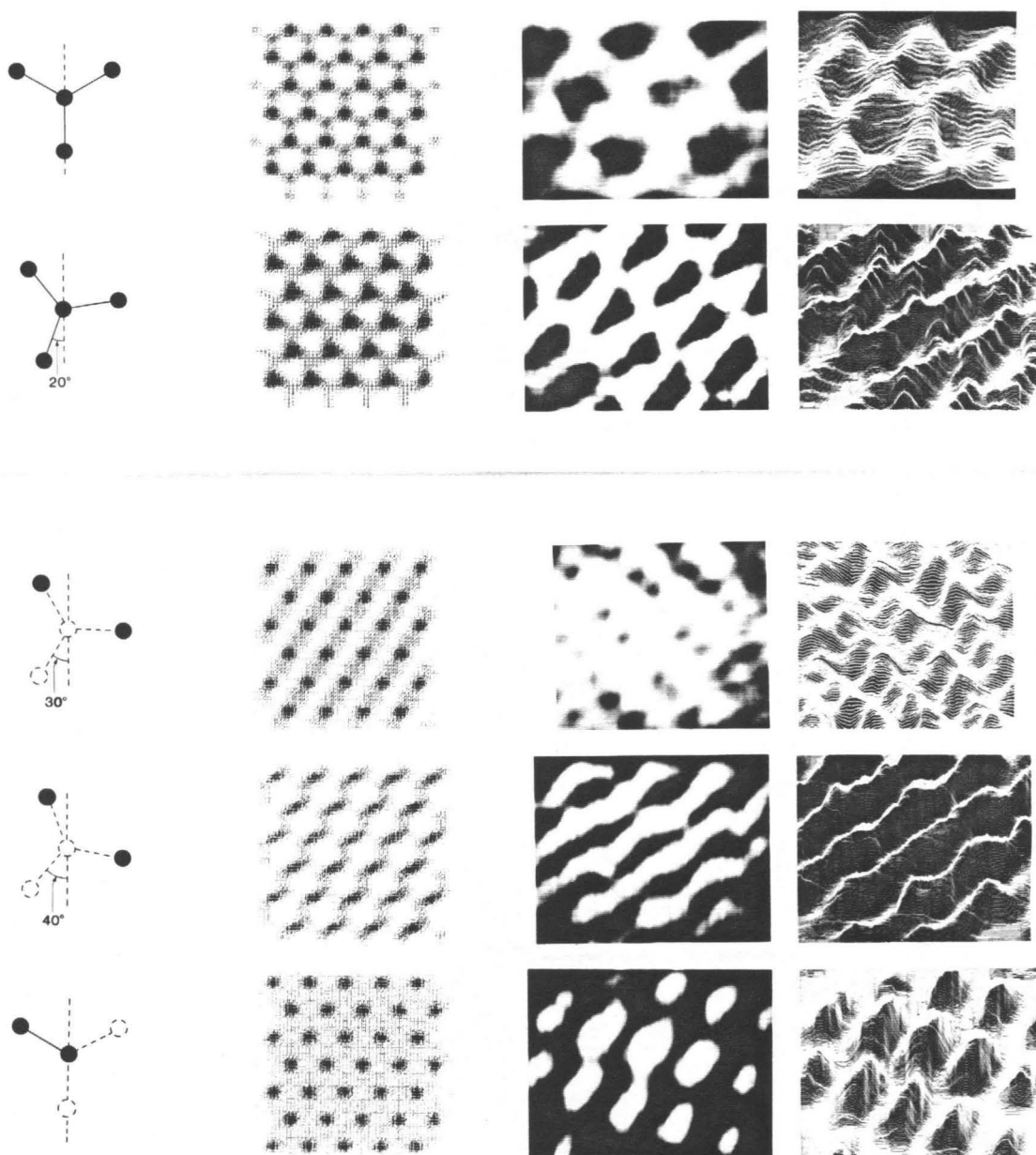


Figure 5: Comparison of computer-generated images with experimental images on HOPG. The computer-generated images were obtained using the trigonally symmetric, 4-atom tip or the asymmetric 2-atom tip rotated from registry with the underlying graphite surface as indicated by the farthest left sketch. The experimental images are gray-scale and line drawn plots obtained with a graphite coated tungsten tip or a graphite tip in the current-imaging mode. The computer-generated and experimental images are not the same scale.

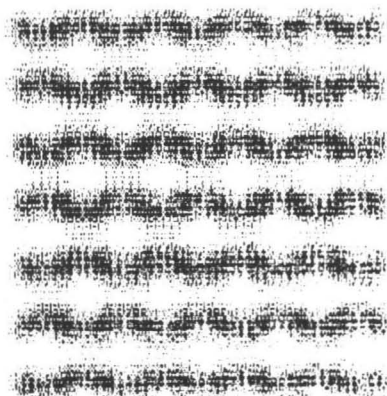
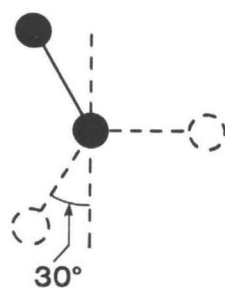
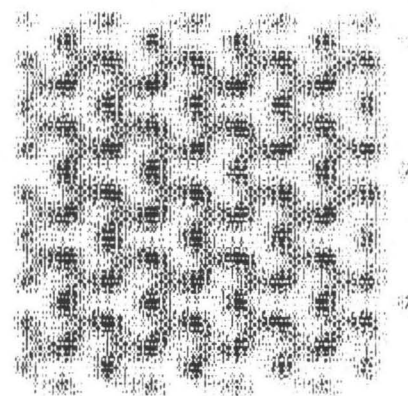
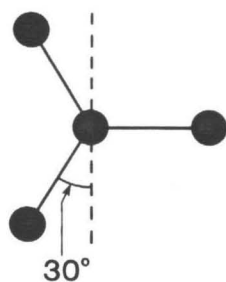
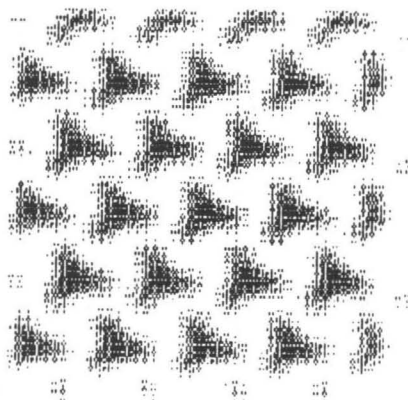
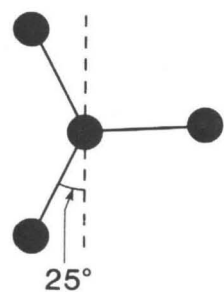


Figure 6: Computer-generated images obtained as in **Figure 5** with symmetric 4-atom tips rotated 25° and 30° and an asymmetric 2-atom tip rotated 30° as indicated to the left of the image.

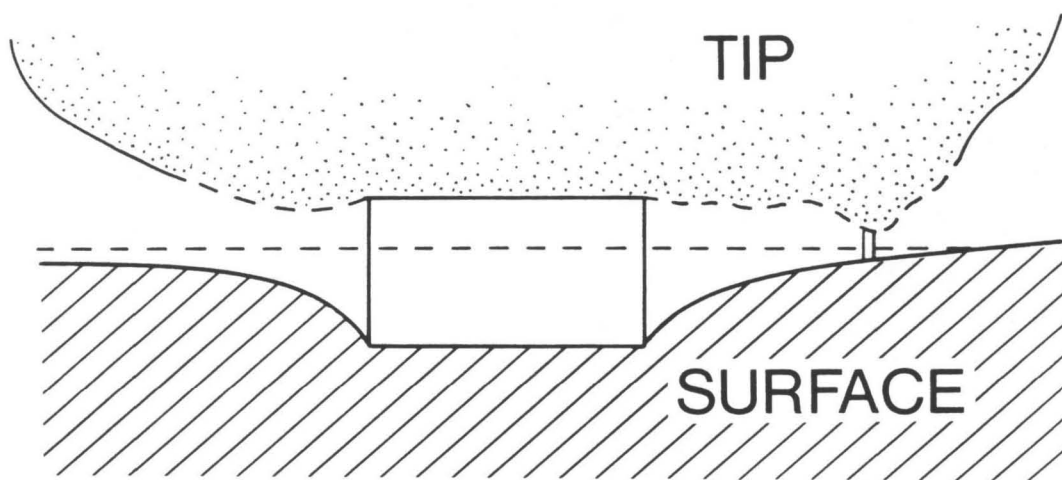


Figure 7: Sketch of a tip pushing through a solid contaminant on the deformable graphite surface. In this case, only one 'mini-tip' is within tunneling range, but multiple tips are possible and different 'mini-tips' may become active within a scan.

POINT-CONTACT IMAGING OF HOPG

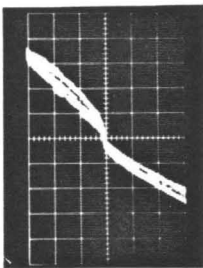
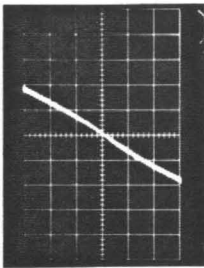
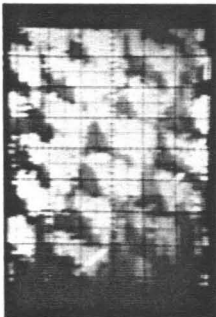
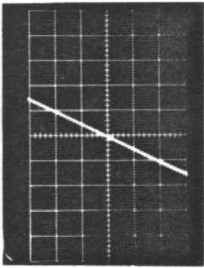
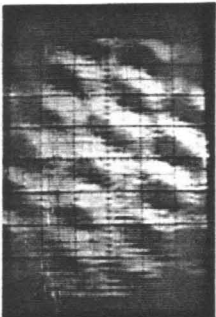
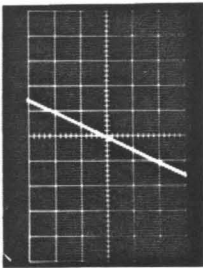
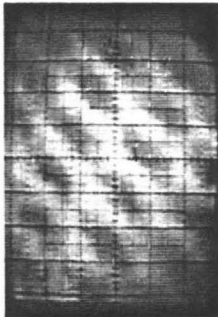
$\Delta Z(\text{nm})$	I-V	IMAGE	TIP-SAMPLE BIAS CONTRAST
0		very noisy	<ul style="list-style-type: none"> • 450mV • - - -
8.48			<ul style="list-style-type: none"> • 250mV • 5nA
20.2			<ul style="list-style-type: none"> • 20mV • 3nA
23.5			<ul style="list-style-type: none"> • 20mV • 2nA

Figure 8: STM images obtained in the current-imaging mode at 500 mV sample bias using a graphite-coated tungsten tip on HOPG for the following conditions: gap position, Δz from top of gap, contrast current, tip to sample bias and average tunneling current for a) upper-mid, 8.5 nm, 5 nA, 250 mV, 25 nA b) lower, 20.2 nm, 3 nA, 20 mV, 48 nA and c) bottom, 23.5 nm, 2 nA, 20 mV, 48 nA.

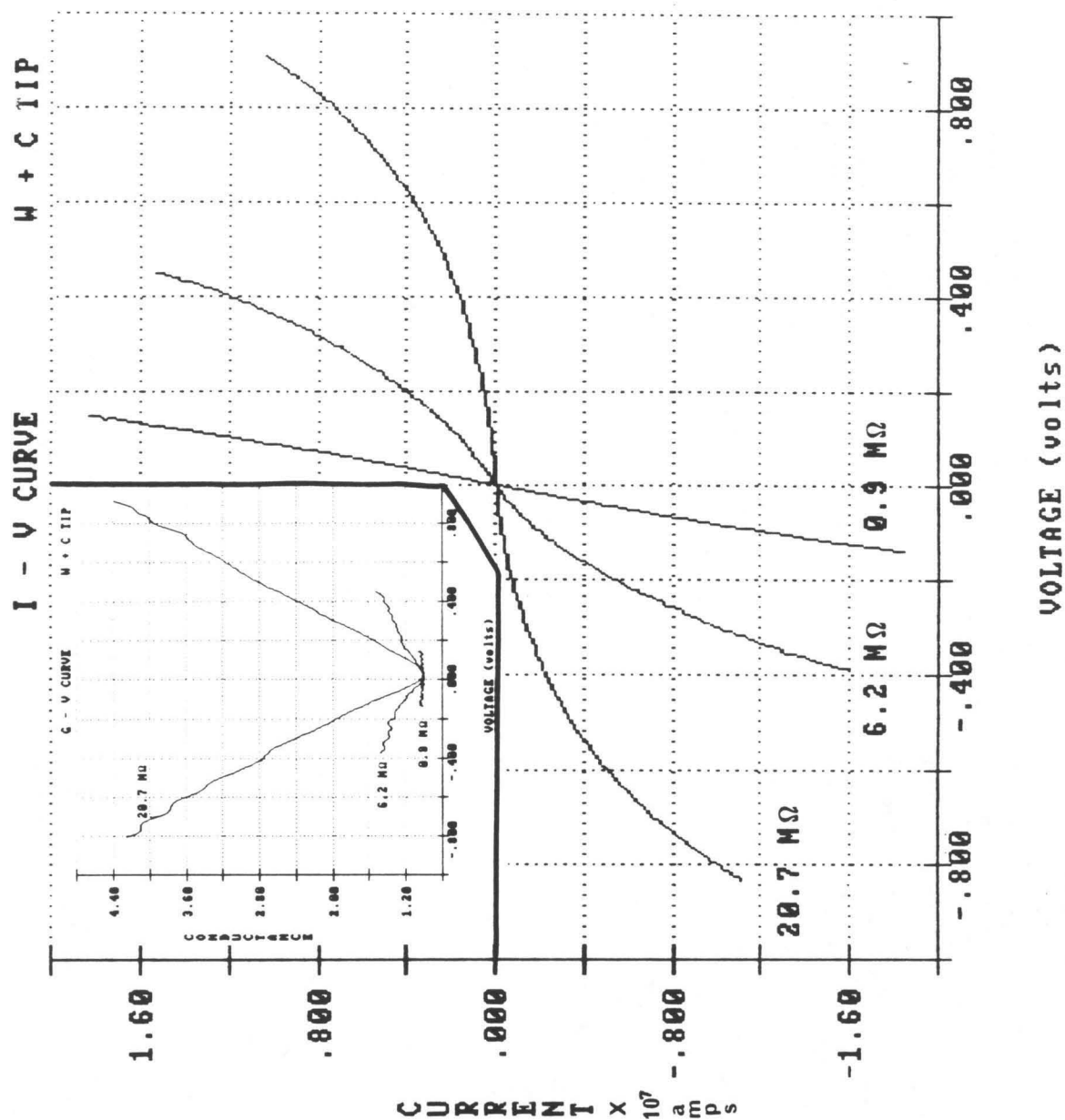


Figure 9: Current-voltage (IV) curves for a graphite-coated tungsten tip and HOPG sample at tunnel gap resistances of 20.7, 6.2 and 0.9 MΩ. The inset shows the conductance-voltage (GV) curves obtained by numerically differentiating the IV data. The GV curves have also been smoothed and normalized.

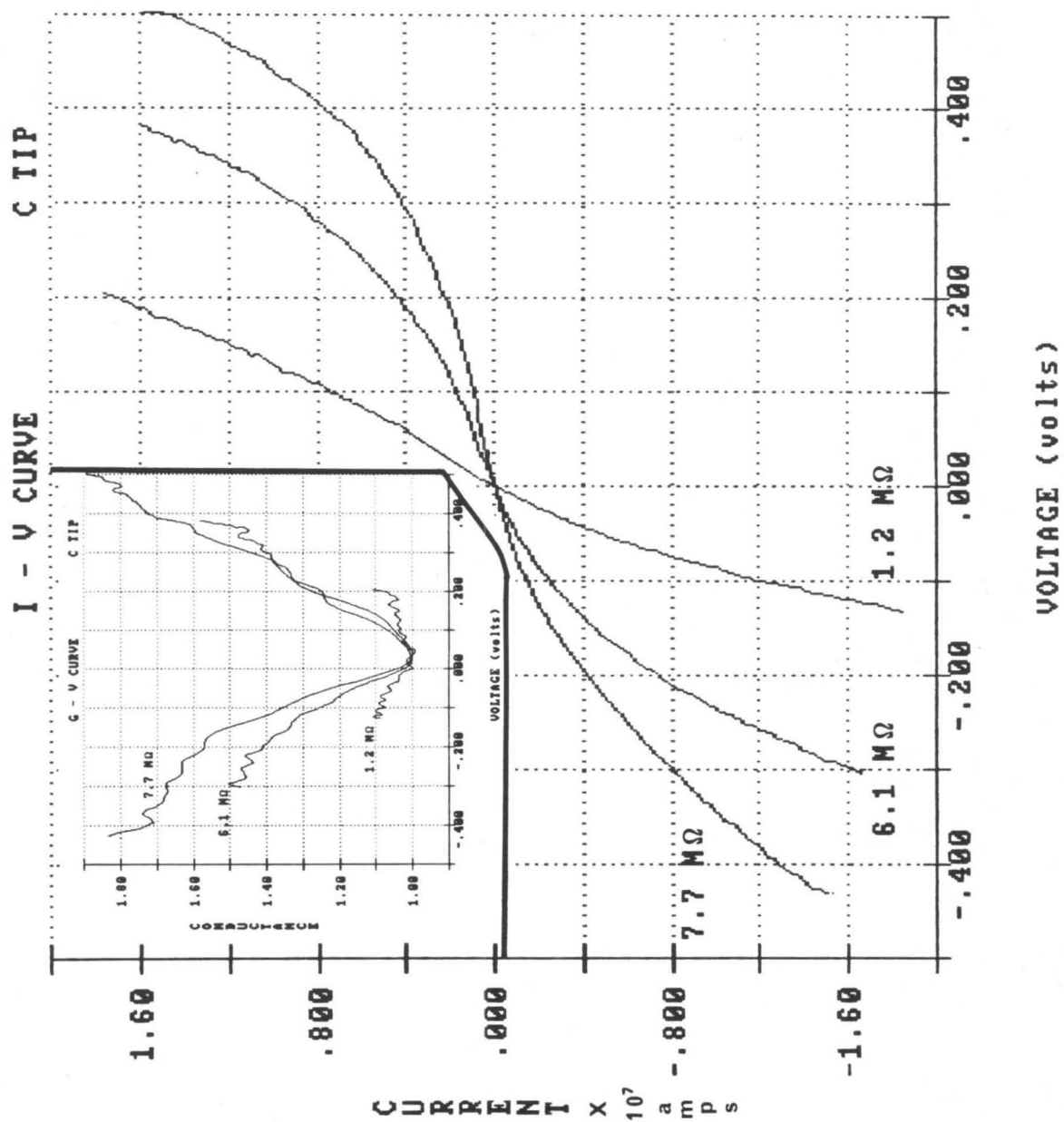


Figure 10: Current-voltage (IV) curves for a graphite (C) pencil-lead tip and HOPG sample at tunnel gap resistances of 1.2, 6.1 and 7.7 MΩ. The inset shows the conductance-voltage (GV) curves obtained as in Figure 9.

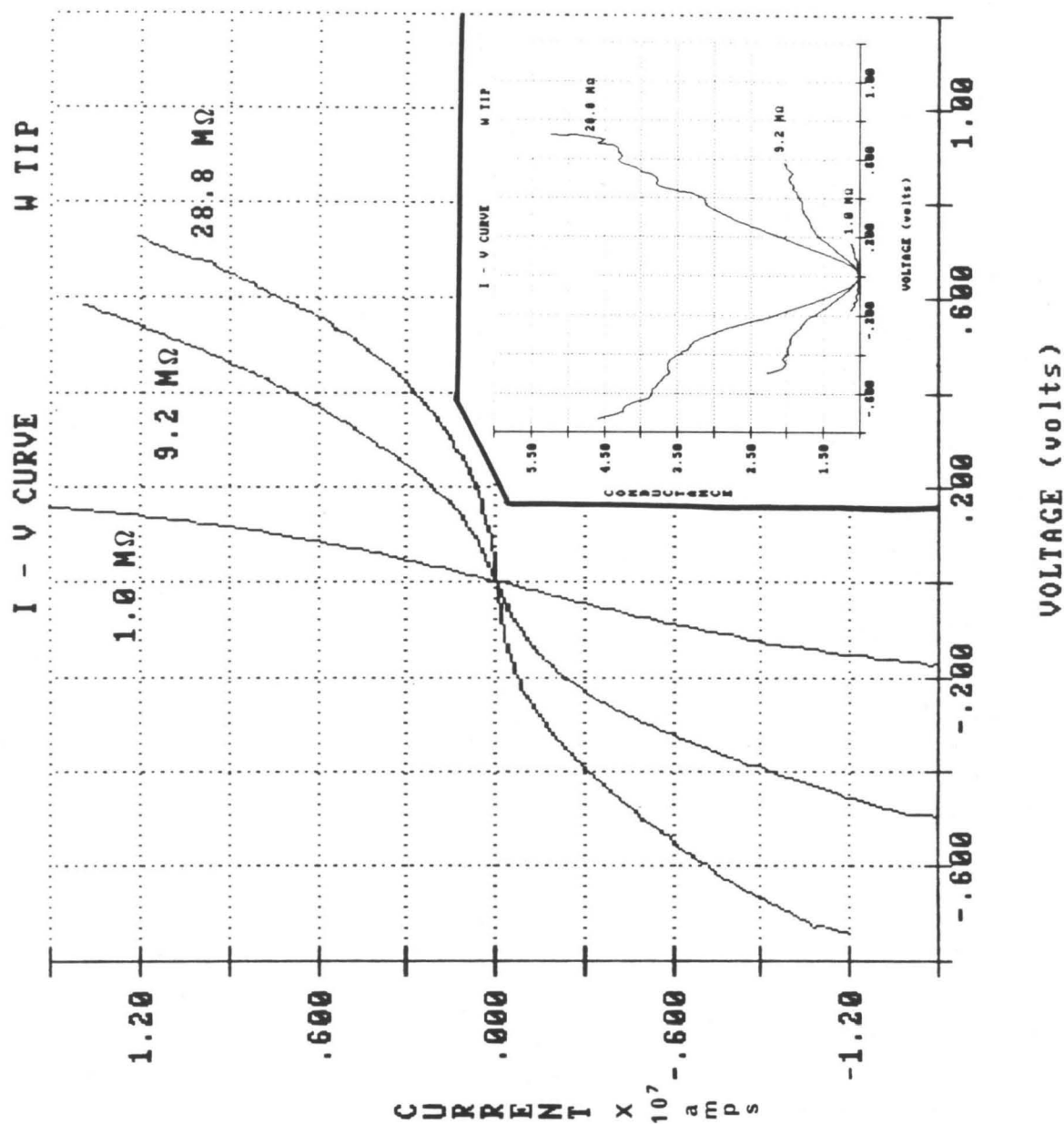
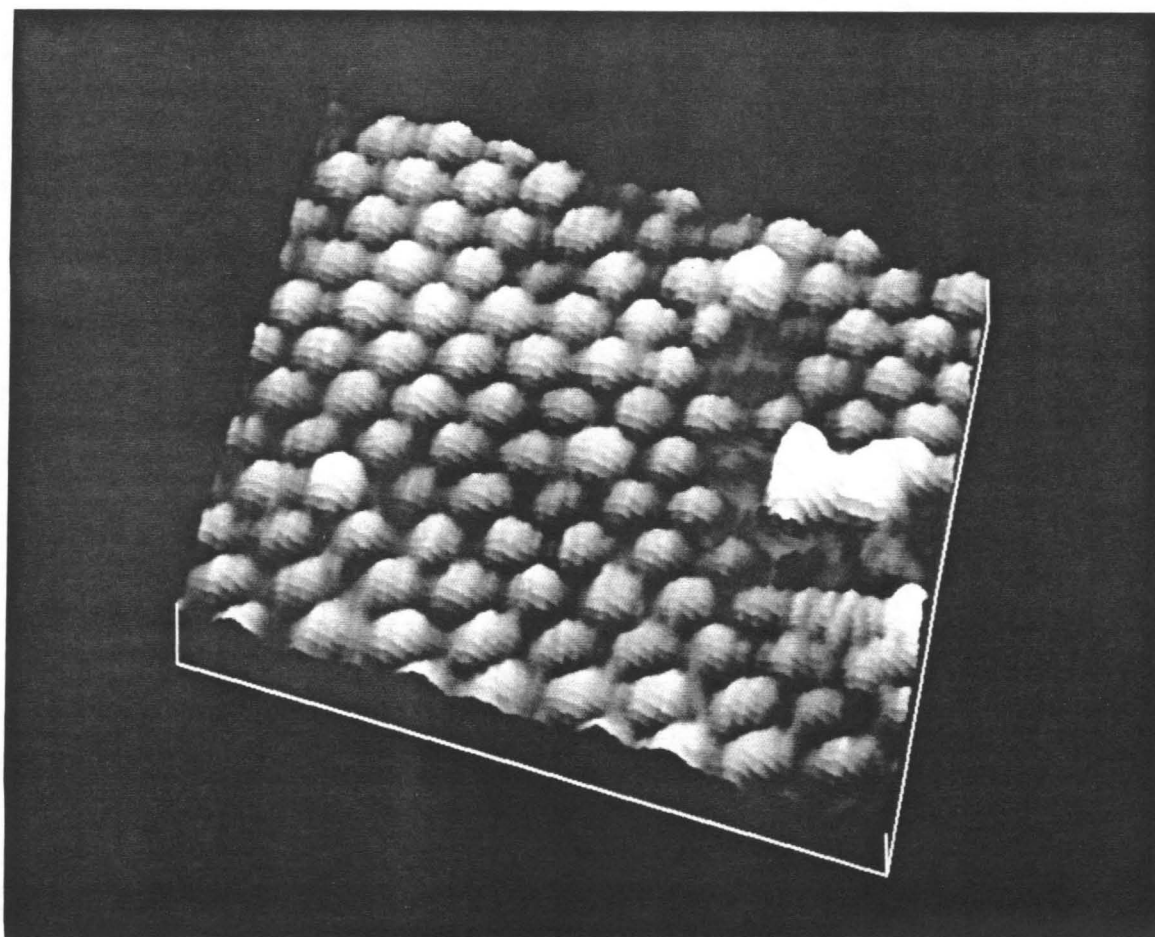


Figure 11: Current-voltage (IV) curves for a clean tungsten (W) tip and HOPG sample at tunnel gap resistances of 1.0, 9.2, and 28.8 $\text{M}\Omega$. The inset shows the conductance-voltage (GV) curves obtained as in Figure 9.

Chapter 3

PREPARATION AND ANALYSIS OF THE SILICON (111) SURFACE



INTRODUCTION

Background

Although interpretation of STM images has improved since the STM's introduction to the scientific community, a number of basic questions about the physics of imaging still remain. Only conducting materials in vacuum or air were initially considered as feasible substrates for STM studies. However, STM imaging in aqueous and other liquid solutions was soon accomplished¹. With the possibility of imaging molecules with atomic resolution in environments other than ultrahigh vacuum (UHV) or of ordered crystalline arrays, researchers began to examine larger molecular systems including proteins^{2,3} and nucleic acids⁴. Although atomic resolution is very rare in these systems⁵, electron tunneling apparently does occur to or through these molecules that are considered to be insulators.

The advance of STM imaging from single atoms on metals or semiconductors to large, molecules with high molecular weight was quite a large step. Even on well characterized semiconductors, the ability to distinguish definitively between types of atoms is not yet possible. Imaging adsorbates on surfaces poses particular problems as well. Smaller molecules are not necessarily "seen" in a topographical sense, although they may be observed spectroscopically. Larger biological molecules, both mobile and deformable, have the more difficult problem of being insulators. Yet, rough images of nonconductors have been produced. A fundamental question remains: On an atomic level, how does a tip/adsorbate/surface interaction affect the images and spectroscopy observed by STM?

Often, the atomic structure of the adsorbate on a surface is not observed by STM. The lack of topographical information on an adsorbate because of its energy levels lying well below or above those probed by the STM may be overcome by examining the effect of the adsorbate on the underlying surface.

¹B. Giambattista, W. W. McNairy, C. G. Slough, A. Johnson, L. D. Bell, R. V. Coleman, J. Schneir, R. Sonnenfeld, B. Drake and P. K. Hansma *Proc. Natl. Acad. Sci. USA* **84**, 4671 (1987)

²Lukas Häussling, B. Michel, H. Ringsdorf and H. Rohrer *Angew. Chem. Int. Ed. Engl.* **30** (5), 569 (1991)

³J. P. Ruppertsberg, J. K. H. Hörber, C. Gerber and G. Binnig *FEBS Letts.* **257** (2), 460 (1989)

⁴D. Keller, C. Bustamante and R. W. Keller *Proc. Natl. Acad. Sci. USA* **86**, 5356 (1989)

⁵R. J. Driscoll, M. G. Youngquist and J. D. Baldeschwieler *Nature* **346**, 294 (1990)

Although the molecular energies are not directly accessed, the perturbation of the surface wave functions, localized at the adsorbate site most likely produce a mechanism for image contrast⁶. By studying the spectroscopy of the adsorbate/surface interaction, the extent of adsorbate effect on the overall surface wave functions may be studied. If information about adsorbate structure is desired, optimum STM operating conditions need to be chosen reliably to produce the maximum contribution of contrast from the adsorbate wave functions to the image, perhaps by judicious selection of tunneling bias and current set point.

Proposed Experiments

In order to address these questions adequately, a well characterized surface to which a variety of molecules can be adsorbed in submonolayer coverage is required. The (7x7) reconstruction of the silicon(111) surface has been extensively studied by STM. Wolkow and Avouris⁷ have performed atom-resolved chemistry studies of NH₃, H₂O and other small adsorbates on Si(111) (7x7). Villarrubia and Boland have prepared the (7x7) surface and observed chlorine removal of adatoms⁸ and hydrogen interactions with this surface⁹. Furthermore, they have demonstrated the ability of STM to distinguish between the different products from the reaction of Cl with this surface¹⁰.

The (7x7) reconstruction of this surface is known by other techniques to be highly reactive to a variety of adsorbates. Organic molecules containing either a hydroxy or carboxy group react with the Si(111) (7x7) surface through the oxygen atom and subsequent dissociative adsorption at room temperature^{11,12,13}. Methanol^{11,12}, ethanol, as well as formic acid (HCO₂H), propanoic acid (CH₃CH₂CO₂H), acrylic acid (CH₂=CHCO₂H), propiolic acid

⁶M. G. Youngquist, R. J. Driscoll, T. R. Coley, W. A. Goddard and J. D. Baldeschwieler *J. Vac. Sci. Technol.* B9 (2), 1304 (1991)

⁷R. Wolkow and Ph. Avouris *Phys. Rev. Lett.* 60 (11), 1049 (1988)

⁸J. S. Villarrubia and J. J. Boland *Phys. Rev. Lett.* 63(3), 306 (1989)

⁹J. J. Boland *J. Phys. Chem.* 95, 1521 (1991)

¹⁰J. J. Boland and J. S. Villarrubia *Science* 248, 838 (1990)

¹¹K. Edamoto, Y. Kubota, M. Onchi and M. Nishijima *Surface Science* 146 L533 (1984)

¹²J. A. Stroscio, S. R. Bare and W. Ho *Surface Science* 154, 35 (1985)

¹³D. Outka, J. Stöhr, R. Madix, H. Rotermund, B. Hermsmeier, J. Solomon *Surface Science* 185, 53 (1987)

(HC=CCO₂H) and the corresponding alcohols¹³ were adsorbed and studied by electron energy loss spectroscopy (EELS), thermal desorption spectroscopy (TDS), photon induced desorption spectroscopy, high resolution EELS, and low energy electron diffraction (LEED). These adsorbates are stable to well over 450°C and are covalently bound to the surface, minimizing molecular motion. Furthermore, the addition of unsaturated bonds to the hydrocarbon has been shown not to affect the adsorption and provides a system in which the electronic properties of the adsorbate can be selectively modified with minimal change to the overall system parameters.

The (7x7) surface also exhibits two different types of dangling bond sites which should show different reactivities¹⁴. The adatom sites are electron-poor so that they should act as sites for nucleophilic reactions. Conversely, the rest atoms are electron-rich and should react with the electrophilic portion of molecules. Thus, adsorption of an unsaturated alcohol or acid whose reactive sites were separated by the interadatom distance of the surface could provide information about the effect of reacted sites on neighboring sites and determine exactly the placement of the molecule on the surface.

Summary

This study was proposed to elucidate systematically the effects of different molecular properties of small organic adsorbates on the image obtained by STM. Understanding these effects should lead to the optimization of conditions for imaging larger organic molecules, for differentiating between types of bonds and for describing the physics important for the theoretical understanding of large-molecule imaging.

The first step in such a project is to prepare reproducibly and characterize the silicon surface before adsorbing the series of molecules. This chapter addresses the construction of the heating apparatus for obtaining the silicon (7x7) surface in vacuum, the important constraints of the preparation and the different surface features that may be observed upon exposure to sub-maximal vacuum. Designs for an *in situ* UHV tip transfer are also presented. Variables influencing the nature of the surface cleanliness and saturation of the surface by boron atoms migrating from the bulk of the sample will also be discussed. Finally, the apparatus necessary for the dosing will be described.

¹⁴Ph. Avouris and F. Bozsco *J. Phys. Chem.* 94, 2243 (1990)

THEORY AND EXPERIMENT

Preparation of Si(111) (7x7)

In order to prepare the clean Si(111) (7x7) surface, the oxide must be removed and the silicon atoms given enough energy to overcome the translational barrier and form the most stable surface configuration, minimizing the number of dangling bonds as well as the surface strain⁹. Typically, the silicon must obtain a temperature from 950-1250°C. Many discussions on the stability of the (7x7) surface as well as the similar (5x5) and (9x9) surfaces have been published¹⁵. Furthermore, the methods used to prepare the Si(111) surface are also used to prepare the clean Si(100) surface, which is even more sensitive to environmental conditions. Although a variety of recipes are followed to prepare reproducible (7x7) surfaces, certain factors are common to all preparations.

The sample must never be touched with stainless steel, as Ni and other metals will contaminate the surface (Teflon-coated or plastic tweezers are acceptable.) The electrical contact to the sample should be made with either molybdenum or tantalum, as they have very low vapor pressures at elevated temperatures. The pressure of the system should not rise above 10^{-10} during the final stages of the oxide removal and heating (higher pressures are acceptable at temperatures below $\sim 700^\circ\text{C}$ before the final "flash" and during initial outgassing). The pressure restriction is primarily important in the range of 900-1100°C, for in that temperature range, hydrocarbon "cracking" occurs on the surface from background system contamination¹⁶. Above $\sim 1100^\circ\text{C}$, the silicon evaporates from the surface faster than the incoming molecules. However, Hamers and Demuth¹⁷ claim to observe the (7x7) reconstruction by annealing at 1225K (940°C) without any higher flashes at pressures less than 10^{-9} torr. More typically, the sample is flashed 1-3 times at temperatures ranging from 1050-1200°C^{18,19,20} for 15-30 seconds in order to obtain the desired reconstruction with no significant rise in chamber pressure

¹⁵R. S. Becker, B. S. Swartzentruber, J. S. Vickers and T. Klitsner *Phys. Rev. B.* **39** (3), 1633 (1989)

¹⁶R. J. Hamers *Phys. Rev. B.* **34**, 5343 (1986) and B. S. Swartzentruber *J. Vac. Sci. Technol. A* **7**, 2901 (1989)

¹⁷R. J. Hamers and J. E. Demuth *J. Vac. Sci. Technol. A* **6** (2), 512 (1988)

¹⁸T. Sakurai, Y. Hasegawa, T. Hashizume, I. Kamiya, T. Ide, I. Sumita, H. W. Pickering and S. Hyodo *J. Vac. Sci. Technol. A* **8** (1), 259 (1990)

Two types of heater designs will be discussed; radiative and resistive. Electron-beam heating is another common method for heating silicon samples but was not feasible in the Caltech system because of geometry constraints. Both radiative and resistive heating of the silicon sample were attempted. The advantages and disadvantages of each method will be discussed in subsequent sections.

In designing a heating system for the Caltech UHV system, certain restrictions must be considered. First, the STM uses a "louse" for sample coarse motion²¹. The sample bias is provided through contact to a sample stub that fits into a hole on the tongue of the louse. A spring clip holds the stub vibrationally immobile. Because the louse fits under the assembly for the X, Y and Z piezoceramics, the stub must be no larger than ~.3" in height (~5 mm). Second, the heater system must have a separate base and stub design allowing for transfer of the stub from the heater in the sample preparation chamber to the louse in the STM chamber. Finally, the stub must make good electrical contact with the sample and with the louse tongue. This final restriction can be difficult for radiative heating, where the sample should be physically removed for the stub to minimize any thermal conduction of heat from the sample, and for resistive heating, where the sample needs to be electrically isolated from the body of the stub.

Radiative Heating

Theory and Design

Radiative heating has been used to heat silicon wafers for thin-film processing²². It is an attractive technique for the Caltech system because the sample can be mounted on a stub without concern for electrical isolation. In radiative heating, the sample is brought within close proximity of a radiating filament. The radiation from the filament can be focused by a highly reflecting material onto the sample to minimize loss to the walls.

¹⁹R. Wiesendanger, G. Tarrach, D. Bürgler and H.-J. Güntherodt *Europhys. Lett.* **12** (1), 57 (1990)

²⁰H. Tokumoto, K. Miki and K. Kajimura *J. Crystal Growth* **99**, 1329 (1990)

²¹For all references to the design of the Caltech UHV system, one should refer to the Ph. D. Thesis of John A. Kramar *Scanning Tunneling Microscopy and Spectroscopy of Molybdenum Disulfide*, California Institute of Technology, 1990

²²C. K. Chen and J. S. Im *Appl. Phys. Lett.* **55** (12), 1238 (1989)

A diagram of the radiative heater is shown in **Figure 1**. The sample stub consists of thin tantalum supports beneath each of two sides of a rectangular sample on either a BN stub or a stub milled from pure Ta. The sample is elevated from the stub on the rails to minimize contact and thus thermal conductivity away from the sample. The pancake filament was placed very close to the sample (<.5 cm), and a highly reflective tantalum-foil shroud acted to focus the emitted radiation back to the filament and the sample. The filament temperature was determined by optical pyrometry. The surface temperature of the silicon was not observable because of the relative brightness of the filament.

The total power delivered to the system is determined by $I^2R=Q_f$, the power used to heat the filament. Losses from the heater filament are due to radiative emission to the sample and to the walls. Emission/absorption for radiating and absorbing materials is calculated from a T^4 power law as follows:

$$Q = \sigma A \theta (\epsilon_A T_A^4 - \epsilon_B T_B^4) \quad , \quad (1)$$

where A = the surface area of the emitter, σ = the Stefan-Boltzmann constant (W/cm^2K), ϵ is the emissivity (unitless), assuming a grey body (absorptivity equals emissivity), θ is a view factor for the absorbing medium (unitless), and T is the temperature in K.

The filament (designated with subscript f in future equations) produces heat that is distributed by radiation to the walls (Q_w) and to the sample (Q_s), since the filament is not in thermal contact with any other medium,

$$I^2R = Q_w + Q_s \quad . \quad (2)$$

At equilibrium, the heat absorbed by the sample from the radiating filament equals the heat transferred away from the sample by thermal contact to the stub upon which it is mounted. The heat transfer calculated for two objects of different temperature is

$$Q = C \kappa R_c \frac{dT}{dx} \quad , \quad (3)$$

where C = area of contact (cm^2), κ = thermal conductivity ($\frac{\text{W}}{\text{cm K}}$), and R_c is a correction factor for the contact resistance (unitless), dT/dx is the temperature drop (K) for a given distance (cm). Thus, the equilibrium heat transfer into and out of the sample, $Q_s(\text{in}) = Q_s(\text{out})$, is

$$\sigma A_s \theta (\epsilon_f T_f^4 - \epsilon_s T_s^4) = C \kappa_{\text{stub}} R_c \frac{(T_s - T_{\text{stub}})}{x} \quad (4)$$

For the heater system at equilibrium, Equation 2 becomes

$$Q = I^2 R = \sigma A \theta_1 (\epsilon_f T_f^4 - \epsilon_w T_w^4) + C \kappa \left(\frac{T_s - T_{\text{stub}}}{x} \right), \quad (5)$$

where R_c will be assumed to be 1 for an upper bound on the necessary input power and x is the distance from the sample/stub contact to an area of known T on the stub.

A minimum value for the sample temperature can be calculated, assuming the maximum amount of radiative absorption from the walls and thermal conductivity away from the sample. A plot showing the theoretical filament and sample temperatures for the stub in equilibrium is shown in **Figure 2**. The actual parameters used correspond to the experimental parameters of the heater built and schematically diagrammed in **Figure 1**. The view factor, θ , here refers to the fraction of total area subtended by the absorbing medium for a given area of emitting filament and is $\sim 30\%$. The area of the pancake heater is calculated assuming a two-sided, infinitely thin, flat disk ($2\pi (.005 \text{ m})^2 \times 2$). The thermal conductivity of boron nitride is $.0179 \text{ W/K-cm}$ (tantalum is 0.575 W/K cm). The thin Ta rails are assumed to be at the same temperature as the sample, so the temperature drop to 300K is estimated across the distance to the bottom of the stub (0.4 cm). The emissivity of the filament ϵ_w is 0.5 (not a polished surface) and that of the polished silicon surface is $\epsilon_{\text{si}} = 0.2^{23}$. As shown in **Figure 2**, the filament temperature at steady-state equilibrium is 250-300K greater than the sample temperature for the temperature range important for silicon preparation.

²³Values from Robert Weast and Melvin Astle, eds. **CRC Handbook of Chemistry and Physics**, 62nd Edition (CRC Press, Inc.: Boca Raton, FL), 1982

The total power needed in the filament to raise the sample to the desired temperature can be calculated using the data from **Figure 2** by assuming that the filament temperature is 300K greater than the sample temperature and substituting into Equation 5. The necessary heat supplied to the filament, Q_f , is plotted versus the sample temperatures between 1000K and 1500K in **Figure 3**. The calculated range of input powers is accessible with standard laboratory equipment.

Experimental Parameters

The heater and filament were degassed by constant heating up to 1400°C continuously during and after the system bakeout until the pressure in the sample preparation chamber remained in the low 10^{-9} torr. The silicon samples were mounted on the stubs, often degassed for 8 hours to 2 days at 700°C before flashing to greater than 1000°C. The temperature was lowered either rapidly or slowly depending on the experiment. The samples were allowed to cool briefly and transferred to the STM chamber as quickly as possible. The transfer time when the system was open to the long-stroke translator varied from ~1-5 minutes, depending on whether pressure was to be minimized by moving the translator slowly (P remains in the high 10^{-8} range) or by moving the sample quickly to the STM chamber (P bursts into the low 10^{-7} range upon rapid translator motion). All images of silicon were taken with ac-etched tungsten tips.

Resistive Heating

Theory and Design

The majority of Si(111) (7x7) surfaces reported in STM studies are prepared by resistive heating. Vacuum STM systems built with the intent of preparing these types of surfaces often use sample holders that are made to fit snugly on two sides of the sample and into the heater as well *without* subsequent transfer to a different chamber. No external filaments close to the sample surface are necessary, so that after the surface has been heated, the STM tip can approach the sample directly. Also, the desorption from the surface is not blocked, so the oxide and contaminants have less chance of readsorption. The temperature of the surface can be easily monitored by an

optical pyrometer. In order to modify the sample stub for use in the Caltech system, the sample mounting scheme for the radiative heater could be used, but the rest of the stub and heater design were completely redone.

A diagram of the final design for the resistive heater is shown in **Figure 4**. The central core of the stub is milled from an insulating material with excellent UHV and heater properties: it does not outgas at very high temperatures, it is UHV compatible and it has a very high melting point. Both Macor and Boron nitride stub cores were made with no differences observed except that the softer BN was easier to mill, thus a less expensive use of time. Since it is imperative that the silicon be in contact with only Mo or Ta (metals with very low vapor pressure and very high melting points), the sample stub rails upon which the sample rests were made of Ta²⁴ as were the 0-80 screws. The bottom rails that make contact with the heater were machined from 304 stainless steel as were all the metal components of the heater itself. The sample was held snugly onto the stub by means of Ta wire clips, which were pressed onto the sample by tightening the screw or by the screw heads themselves. Care was taken to assure that contact on the surface was behind the edge of the step of the rail so that the current would flow primarily from the bottom rail contact and not through the focused wire contact.

The heater base [**Figure 1**] has two spring clips that hold the sample stub in place. The springs are compressed between two metal blocks with one end of the spring applying pressure to a stainless-steel ball, which extends .020-.030" beyond flush with the surface. The spring-loaded balls hold the stub in place and can provide electrical contact if the stub does not make good contact with the base. Furthermore, the bottom rails of the sample stub are angled slightly outward so that the ball tends to pull the stub downward to make contact with the bottom of the heater platform as well. In this manner, electrical contact is assured in at least one place, probably two, on each side of the stub.

The stub is pushed into the heater base with a UHV-compatible wobblestick equipped with a pointer end. The current is brought to screws set in the heater base by copper leads. The sides of the heater base are electrically

²⁴It is best to use Ta "foil" of the same thickness as the rail because of the difficulty in machining such small parts. In this case, the rail was 0.050" thick; thus, the purchase of foil of that thickness enabled machining of only the step.

isolated from each other and are mounted on a Macor baseplate. The measurement of the placement of these sides on the plate has a very close tolerance if the sample stub is to fit snugly between them without losing contact on either side or without its being impossible to push into place with an externally operated wobblestick.

Experimental Parameters

A Hewlett Packard Harrison 6274A dc current-regulated power supply was used to control and monitor the current through the sample. It is important to note that the silicon originally has an oxide layer which for a typical sample increases the resistance of the silicon-to-metal contact to greater than $500\text{k}\Omega$. In order to produce a stable heating current, the oxide must first be removed utilizing a power much greater than will be necessary for the regulated heating. Without the use of a regulated current source, the sample experiences a huge current surge after the resistive oxide layer is removed (resistance decreases dramatically) and typically melts. Setting the current to $10\mu\text{A}$ typically protects current spikes from destroying the sample. Initially, boron-doped silicon (111) wafers were used with $.005\text{--}.002\Omega\text{-cm}$ resistivity. This low resistivity was used to insure adequate conduction when adsorbates were dosed onto the surface. Subsequently, $1\Omega\text{-cm}$ *p*- or *n*- type wafers were used to reduce the need for high currents and to reduce the diffusion of dopant atoms to the surface.

System Modifications

In Situ Tip-Transfer Design

An important feature in an ultrahigh vacuum system is the ability to change samples and tips without opening the system to air. *In situ* sample transfer was originally built into the STM system, but the tip transfer was not. The designs for the Caltech UHV *in situ* tip-transfer system are presented and discussed here.

The tip is held at 45° from perpendicular to horizontal so that it is at 90° to the sample presented by the louse. This arrangement facilitates the resting of the tip in the holder while tightening any clamping mechanisms. The tip holder is shown in Figure 5. The tip is held in place by an 0-80 screw,

polished to a cone at the tip end and spot-welded to a 0.010" tantalum wire at the other end. The thin wire was used to minimize the mass and to act as a paddle wheel, which can be turned by the wobblestick. The slot is large enough to accommodate tips up to 1/8", but the set screw is milled to a smooth conical end in order to clamp wires of 10 to 25 μ m securely against the corner. The tips are bent so that they can be carried by a wobblestick, stored in the same racks as the sample stubs and rested against the back of the tip holder while tightening the set screw.

This design was a simple modification to the existing Ultra-high vacuum STM system described in detail in the thesis of John A. Kramar²⁵. Its function is primary to the continued and productive use of a vacuum STM and has been practically trouble-free.

Vacuum Gas Doser Design

The next step in characterizing small molecules is the chemical adsorption of the chosen hydrocarbons on the Si(111) (7x7) surface. One method of dosing a surface is to back-fill the chamber with the gas of choice. The advantage of this method is that it is easy and involves no modification of the existing system. The disadvantages, however, are serious. With only backfilling of the chamber with the gas of choice, characterization of the amount of coverage on the surface is virtually impossible without surface analytical techniques, as is the determination of a surface sticking coefficient. Also, the molecules will not adsorb selectively to the silicon surface but will adhere to most surfaces in the chamber. If dosing is performed in the STM chamber, this nonselective adsorption is highly problematic because piezoceramics and Viton elastomers, which cannot be baked to very high temperatures to remove the adsorbed gases, will become adsorption sites. As a result, the ultimate pressure and pumping speed may be compromised.

A molecular gas dosing system can be implemented into the sample preparation chamber relatively easily following the designs of Bozack *et al.*²⁶

²⁵John A. Kramar Ph. D. Thesis, *Scanning Tunneling Microscopy and Spectroscopy of Molybdenum Disulfide*, California Institute of Technology, 1990

²⁶M. J. Bozack, L. Muehlhoff, J. N. Russell, Jr., W. J. Choyke and J. T. Yates, Jr. *J. Vac. Sci. Technol. A* 5 (1),1 (1987)

IR Heater for Sample Preparation Chamber Bake

An important aspect of any vacuum system is keeping it free from contaminants such as water and organic molecules that often accumulate when the chamber is open to ambient air. These molecules will raise the base pressure of the system a few orders of magnitude if not properly baked out of the system and adequately pumped. Many UHV systems still use exterior heating tapes to provide the necessary energy to desorb the molecules attached to the interior walls. A convenient and rapid method for baking the sample preparation chamber was ordered and installed: an internal IR lamp²⁷. This item is mentioned because it reduced baking time from three days to one day, and was installed with an internal thermocouple to insure that the internal walls attained a temperature greater than 100°C. The IR lamp can be powered from a simple 10 Amp/120 V Variac. It is highly suggested that those who want convenience and expediency consider this option for chamber bakeout apparatus.

RESULTS

Radiative Heating

The heater was calibrated by monitoring the filament temperature and the input current, since the brightness of the filament and the geometry of the heater obscured direct reading of the sample temperature. The calibration data of the filament temperature as a function of the filament power are shown in **Figure 6**. The sample temperature is assumed to be 200-300K less than the filament temperature and is in good agreement with the calculated temperatures shown in the previous **Figure 3**.

The Si(111) (7x7) surface was not observed using the radiative heater. Instead, large areas with roughness of only ~ 10 Å were observed by STM as shown in the $370 \text{ Å} \times 370 \text{ Å}$ image of **Figure 7** (Si279G). The filament was heated to 1370°C with the pressure in the SP chamber remaining below 5×10^{-9} torr. The pressure rose to greater than 3×10^{-8} torr upon opening to the LS translator. No regular structure is observed in the image, and higher

²⁷Vacuum Generators Internal Quartz Bakeout Heaters (08-102-086), Kurt J. Lesker Distributors, 1515 Worthington Ave., Clairton, PA 15025

resolution scanning on this area produces images that are flat but that also do not exhibit atomic resolution for a number of tips.

In addition, larger-scale roughness was observed for a variety of sample biases. In the 740 Å by 740 Å image presented in **Figure 8** (SI284D), the total height variation in the image is ~95 Å. This sample was subject to a filament temperature greater than 1450°C, and the total pressure remained below 3×10^{-9} torr during the bake. For the variety of samples studied, the full range of surface roughness from nearly flat to large, amorphous bumps were seen with little reproducibility from sample to sample or even from different areas on the same sample.

The probable reasons for the inability to observe the pristine (7x7) reconstruction are relatively straightforward. First, the total pressure of the system would not remain in the 10^{-10} torr range when the tungsten filament²⁸ was heated to the appropriate temperature even after many days of degassing. It is likely that hydrogen within the tungsten or oxygen on the tungsten surface desorbed continuously. Further, although the temperature of the filament is known to within ~50°C, the exact sample temperature cannot be measured with the optical pyrometer because of the intensity of radiation from the filament, which blocks the view to the sample surface. Thus, the temperature of the silicon surface may not have attained the desired range. Furthermore, even if the sample did become clean and the reconstruction did occur, contamination of the sample upon transfer from the sample preparation chamber to the STM chamber is probable as will be discussed in more detail in the following section. The radiative heater was replaced as soon as the resistive heater was completed.

Resistive Heating

Boron Reconstruction on Si(111)

The (7x7) reconstruction was not observed initially on this surface, but a variety of surface morphologies, some similar to those of the radiatively heated surfaces, were seen. In addition to rowlike features and regular mounds, atomic corrugations appeared in the images, but the atomic separation did not correspond to the unit cell spacing of either the bare Si(111)

²⁸R. D. Mathis Company, 2840 Gundry Avenue, P. O. Box 6187, Long Beach, CA 90806 Model H2-.040W design with 0.030 mil diameter wire to minimize power needed

surface or the (7x7) reconstruction. The analysis of this reconstructed surface and the other observed features on the resistively heated silicon are discussed in the following section.

Locating the areas of the clean, reconstructed silicon can be difficult. The STM group at IBM Almaden²⁹ suggests scanning in only the x direction until reproducible, atomically flat scans, typically in a valley, are found. The atomically resolved areas were first detected while examining large, flat valleys such as shown in the 740 Å x 740 Å image presented in **Figure 9** (SI100A). The height variation on the flat planes is limited only by the resolution of the z piezoceramic, voltage-digitization gain set for this image and indicates that the surface is atomically flat. The spacing between adjacent (111) planes in bulk silicon is 3.12 Å, and the surface relaxes away from the vacuum 0.14 Å³⁰. The small steps on this surface correspond to this interplanar spacing. Often observed³¹, multiple-step heights on the Si(111) bulk are also shown in **Figure 9**. The larger steps at 6.7 Å and 9.1 Å in height, are double- and triple-layer steps, respectively, within the calibration of the piezoceramics and tip instabilities.

These atomically flat areas were examined in greater detail. **Figure 10** (SI098D) shows the barrier height image of a 50 Å x 50 Å area of the highly doped silicon surface after degassing at ~700°C for 4 hours and flashing to ~990°C. The image was taken with a 1 kHz modulation to the tip of ~0.3 Å. As explained in the Introduction (*Chapter 1*), the barrier height image contains less noise than the corresponding topographical image because of the nature of the data collection. The centered hexagonal symmetry and stability of the surface suggest a commonly observed reconstruction.

Because the sample was highly doped with boron, the most likely explanation for this atomically reconstructed surface is the migration of dopant atoms to the surface during heating as explained by Bedrossian *et al.*³²

²⁹Dr. Phillip Lippel, private conversation. STM/NANO I Conference, Baltimore, MD, July 1989

³⁰William A. Goddard *Nature of the Chemical Bond: Chemistry 120a*, California Institute of Technology, 8-27 (1986)

³¹P. Bedrossian, K. Mortensen, D. M. Chen and J. A. Golovchenko *Nuclear Instrum. and Methods in Phys. Res. B* 48, 296 (1990)

³²P. Bedrossian, R. D. Meade, K. Mortensen, D. M. Chen, J. A. Golovchenko and D. Vanderbilt *Phys. Rev. Lett.* 63(12), 1257 (1989)

and Thibaudau *et al.*³³ Although other Group III metals such as Al, Ga, and In induce the same ($\sqrt{3}\times\sqrt{3}$) R30° reconstruction as the B atoms on the Si(111) surface, the boron atoms are much smaller (0.8 Å compared to >1.0 Å) and have been shown by high energy He⁺ ion channeling³⁴ and STM^{31,35} to occupy subsurface B₅ sites rather than surface adatom T₄ sites. The boron atom sits beneath a silicon adatom, which reduces three dangling bonds but introduces a new one. The boron atom beneath it has a higher electronegativity, so the dangling bond state of the Si adatom is stabilized by charge transfer to B, thus lowering its apparent height to the STM. For all such flat areas examined on this surface, high-resolution imaging revealed the ($\sqrt{3}\times\sqrt{3}$) R30° B/Si(111) reconstruction.

Salvan *et al.*³⁶ claim that the boron atom actually sits in an MT₄ (also called H₃) site, which gives equivalent geometry to the B₅ site rotated only 30°. They had sufficient resolution in their experiment to verify the inequivalence of each half of the unit cell. Lyo *et al.*³⁵ claim to have imaged the unit cell and observed symmetry between the two halves as did Bedrossian *et al.*³². The majority of papers present evidence toward the subsurface B₅ site, but the controversy has not been adequately resolved. Since the assignment of either of these sites depends on extraordinary resolution or a reference terrace or step, not present in the experiments discussed here, a distinction between the two sites is not suggested. However, the spectroscopic arguments appear to be in agreement with the B₅ site.

A close-up topographic image at -2.0 V and 1 nA and simultaneous barrier height image, both 50 Å x 50 Å, are shown in **Figure 11**. (SI098F) The peak-to-peak variation in height is ~0.5 Å. Plots of height and barrier height are shown in **Figure 12** for the lines drawn on **Figure 11**. The barrier height is plotted in arbitrary units and had measured values less than 0.1 eV. Little interpretation of the meaning of the barrier height measurement has been presented, since few of such images have been published³⁷. However, Binnig

³³F. Thibaudau, Ph. Dumas, Ph. Mathiez, A. Humbert, D. Satti and F. Salvan *Surface Science* **211/212**, 148 (1989)

³⁴Li Luo, G. A. Smith, Shin Hashimoto and W. M Gibson *Radiation Effects and Defects in Solids* **111-112** (1-2), 125 (1989)

³⁵I.-W. Lyo, E. Kaxiras and Ph. Avouris *Phys. Rev. Lett.* **63** (12), 1261 (1989)

³⁶F. Salvan, F. Thibaudau and Ph. Dumas *Appl. Surf. Sci.* **41/42**, 88 (1989)

³⁷B. Marchon, P. Bernhardt, M. E. Bussell, G. A. Somorjai, M. Salmeron and W. Siekhaus *Phys. Rev. Lett.* **60** (12), 1166 (1988), G. Binnig and H. Rohrer, in *Proc. of the 17th Internat. Conf. on*

and Rohrer³⁸ argue that the interpretation is simplified given the assumption of a gap-width independent barrier height. This assumption is valid at larger separations, and then $(d\ln I/ds)$ is proportional to $\sqrt{\phi}$. The barrier height is enhanced if excess electronic charge is present and lowered if there is a deficiency of charge density. Since the image potential tends to lower the barrier height but not produce any local structure at a constant gap distance, the contrast in the barrier height images is primarily a result of charge variations that are an intrinsic property of the localized surface property. Binnig and Rohrer further explain that the anomalously low barrier heights measured, those lowered by up to 50% from expected, can be explained by image potential and corrugation effects (distance modulation is perpendicular to the surface plane but not necessarily perpendicular to the topography at that point). However, the extremely low experimental values a few tenths of an electron volt are still without solid theoretical modeling.

As shown in the line cuts of **Figure 12**, the dark spot in the topographic image corresponds to an atomic area of lowered barrier height. The absence of an atomic feature might be interpreted as a vacancy or missing atom. However, Bedrossian *et al.*³¹ have shown by evaporation of silicon or boron onto the silicon surface that the addition of more boron leads to more of the normal sites, and that more silicon leads to the bright sites. The "boron-free" sites have a silicon atom only in the T_4 site without the subsurface boron atom and can appear up to 1 Å above the subsurface "boron-occupied" sites. Avouris *et al.*³⁹ agree to the assignment of bright and normal sites, but continue to explain that the wave function of the boron-occupied site is less diffuse than the boron-free site, which has a sharp peak in its DOS. Accordingly, the bright sites (brighter than the average atomic height on this surface) correspond to a boron vacancy with a silicon atom in place--it is highly unlikely that the free dangling bonds of this surface are not reacted. The dark spots observed in **Figure 11** and examined in the line cuts of the following figure are thus assigned to be adatoms, the result of a reaction of one of the system contaminants, probably hydrogen, oxygen, water or carbon

the Phys. of Semiconductors, San Francisco, 1984, J. D. Chadi and W. D. Harrison, eds. (Springer-Verlag, New York), 3 (1986) and J. S. Villarrubia and J. J. Boland *Phys. Rev. Lett.* 63 (3), 306 (1989)

³⁸G. Binnig and H. Rohrer *IBM J. of Res. and Dev.* 30 (4), 355 (1986)

³⁹Ph Avouris, In-Whan Lyo, F. Bozso and E. Kaxiras *J. Vac. Sci. Technol. A* 8 (4), 3405 (1990)

dioxide. Interestingly, the barrier height measurement over these sites is also reduced, indicating less charge density and suggesting an adatom over either type of site.

Notice that the large, not atomically resolved, dark areas in the barrier height image of **Figure 11** correspond to bright areas in the constant current image. Presumably, the high topographical areas, greater than 4 atomic layers, are contamination, residual oxide or adsorbed molecules, which have a lower barrier height than the clean surface. Atomic resolution is practically always observed when a strong barrier height signal is measured and never when it is very low.

A positive correlation between barrier height and *z* height is not always observed for atom-sized defects on this surface, and the electronic effects responsible for producing contrast should be considered. As shown in the image of **Figure 13**, sometimes the small, bright "atoms" in the topographic image are dark in the barrier height image (A-negative correlation) and sometimes they are switched to be similar, both bright, in each image (B-positive correlation). These differences are presumably due to the different nature of the defect. The entire row of what appear to be atoms on the topographic image are replaced by "holes" in the barrier height image. This result is consistent with the explanation of unreconstructed silicon in the T_4 position. The silicon has less localized charge density than the boron atom, leaving more delocalized electrons in the dangling bond of the boron-free sites. The reduction of barrier height over these unreacted silicon adatoms follows from these localized properties and describes the negative correlation of sites "A". From the discussion of **Figure 11**, a positive correlation between dark atomic sites is attributed to contamination.

Further support for this assignment comes from the observation of negative differential resistance (NDR), which is highly localized and occurs directly above boron-free positions^{31,39}. In the example of **Figure 13**, these results would imply that the bright spots (A) in the topographic image should correspond to dark spots in the barrier height image because the wave function over "boron-free sites" is more diffuse spatially as well as energetically and thus $d \ln I / d s$ should fall off less rapidly as explained above.

A spatial maximum in the differential conductivity also occurs very locally on boron-occupied sites³⁹. If excess boron is on the surface, the atom could react at an "on-top" site of an already boron-occupied subsurface site.

The strong spatial localization of boron-occupied sites and high charge density of boron are suggested to account for an increased barrier height corresponding to atomic corrugations observed in **Figures 11** and **13** and the positive correlation of bright sites (B).

Additionally, Avouris exposed the boron-rich surface to over 400 Langmuir of NH_3 and saw minimal reactivity indicated by dark spots in the topographic images. This observation would support the ability of the boron-covered silicon surface to remain clean, even in the presence of pressures greater than 10^{-8} torr. The large areas not having atomic resolution that appeared high (bright) when tunneling to unoccupied states in the surface (positive sample bias) and dark in the barrier height image were most likely contamination, characterized by more a diffuse wave function than the crystal surface. Also observed on this surface at various times were current-*versus* voltage curves exhibiting NDR, which correspond to the observations of Avouris and Bedrossian and further support the hypothesis of boron diffusion to the silicon surface.

Finally, a distinction between boron-occupied, boron-free and contaminant atomic sites can thus be determined spectroscopically by comparing topographic and barrier height images. Silicon-occupied sites appear higher than the boron-occupied sites, but the silicon barrier height is low while the boron barrier height is high. Uncharacterized atomic defects appear dark in both barrier height and topographic images.

Topography of Resistively Heated Si(111)

After changing from highly doped silicon wafers to P or As doped, 1 Ω -cm wafers, the atomically resolved, boronated surface was not observed again. Instead, as shown in **Figure 14** (SI164E), some surface images that were similar to those obtained with the radiative heater designs were observed. The sample of **Figure 14** was heated to over 1000°C with obvious areas well over 1100°C . The mounds have a diameter range of 10-50 \AA , slightly smaller than the comparable, radiatively produced mounds but similar in character. Higher-resolution scans of these mounds are noisy and irreproducible in forward to reverse scans. However, returning to the lower resolution, larger area scans do reproduce the small mounds.

A feature not observed in resistive heating but often seen with the radiative heating is the presence of rows as shown in **Figure 15**. (SI277C) The sample was heated to 1100°C. The rows in this image are approximately 20 to 40 Å wide and spread across the entire 740 Å x 740 Å image. These rows may be an artifact of the heating because the sample will often have "hot spots" that appear 100-200 degrees higher than the rest of the sample temperature and may begin to melt.

A transition from rows to isolated mounds was also observed in many images as shown in **Figure 16**. (SI167A)

DISCUSSION

The ability to obtain the clean Si(111) (7x7) reconstruction reproducibly is necessary before the next step of dosing the surface with organic molecules can proceed. How does one explain the inability to observe the desired reconstruction while in other systems, preparation and examination of the surface seem routine? The answer is a combination of inadequate surface analysis tools and a sample translation system that is incapable of maintaining a sufficiently low pressure.

The sample is heated in the sample preparation chamber (SP), which is closed off from both the long stroke translator and the STM chamber by UHV gate valves. With both valves closed, the pressure of the STM chamber is routinely less than 2×10^{-10} torr. During the radiative bake, pressures usually creep into the low to mid- 10^{-9} torr. Resistive heating can be accomplished below the 10^{-9} torr range when the sample is appropriately outgassed. When the gate valve between the sample preparation and the STM chambers is open, the pressure typically does not rise as the STM chamber is usually maintained at a pressure $< 10^{-10}$ torr. However, the long stroke (LS) translator is housed in a thin tube ~ 5 feet long with a 1.5" ID. With both a 20 L/s ion pump and a 80 L/s turbo pump acting simultaneously on the LS, the minimum pressure observed even after a 2-day bakeout period is 8×10^{-8} torr. Two days of pumping on the LS with the ion pump and valves open to the SP chamber, previously near 1×10^{-10} torr has little effect but to raise the pressure of the SP to a minimum of 3×10^{-9} torr. Samples heated both resistively and radiatively in the chamber at this pressure and subsequently transferred to the STM chamber are typically rough as shown in **Figures 13-16**.

When the sample is properly heated above $\sim 1000^\circ\text{C}$, the pressure does not rise into the 10^{-9} torr range. On many occasions, the sample is heated in such a fashion with the gate valves closed. Unfortunately, upon opening the gate valve to the LS, a pressure burst, raising the pressure to the high 10^{-8} torr or even the low 10^{-7} torr, occurs for about 5 seconds with a subsequent drop to the low 10^{-8} torr. At 10^{-7} torr and assuming unitary sticking coefficient on the surface, only ~ 3 seconds are necessary to produce a full monolayer coverage. Furthermore, the pressure may settle eventually to mid 10^{-9} torr only to jump again to 10^{-8} torr or even as high as 1×10^{-7} torr upon moving the translator. By the time the sample reaches the STM chamber, the LS is removed and the gate valve closed, it is highly unlikely to have any contamination-free areas left.

The heater was relocated in the STM chamber to remove the necessity of transfer from the SP chamber. With the constant low pressure, reproducible, clean images of Si(111) (7x7) have been produced. This result suggests that either the resistive or the radiative heater may have been adequate for producing the desired reconstruction, but the constraints discussed above were enough to contaminate the surface during transfer to the STM chamber. The atomically resolved images of boron were presumably the result of boron atoms filling the dangling silicon bonds and reducing the sticking coefficient of the incoming atoms to the surface. As a result, significant areas of the surface retained the clean ($\sqrt{3} \times \sqrt{3}$) R30° B/Si(111) character. If LEED or Auger analyses were available in the sample preparation chamber, the state of cleanliness of the silicon surface after baking but *prior* to transfer could have been determined.

All other options concerning sample contamination and heater malfunction were considered before moving the heater to the STM chamber because of the serious problems with dosing in the presence of Viton and low temperature bakeout materials (refer to doser section). The effects of dosing in the STM chamber should be seriously considered before doing so. Evidence suggests that the surface was properly prepared in a number of instances, but was exposed to higher pressures upon transfer to the STM chamber.

CONCLUSION

The nature of the contaminated silicon surface after 3-5 minutes exposure primarily to hydrogen, nitrogen and carbon dioxide is reproducibly rough, but not always to the same scale. Rows and cloudlike mounds are often seen, and a transition between the two morphologies is also observed. Boron atoms diffusing from the bulk of the silicon upon heating can reduce the reactivity of the surface and protect it from contamination. A comparison of barrier height images and topographic images has been shown to aid in distinguishing between B, Si or unknown contaminants for the first time⁴⁰ and suggests that barrier height imaging may become an important tool for differentiating between elements on a surface.

The preparation of the Si(111) (7x7) surface is relatively straightforward, once the appropriate conditions of highly controllable heating and pressure bursts not exceeding 1×10^{-9} torr can be met. Work is continuing on this project in order to understand molecular contrast mechanisms in the laboratories of Dr. John D. Baldeschwieler.

⁴⁰Shenda M. Baker and John D. Baldeschwieler *Barrier Height Measurements with Scanning Tunneling Microscopy as a Means for Distinguishing Between Species on Silicon*, Manuscript in Preparation

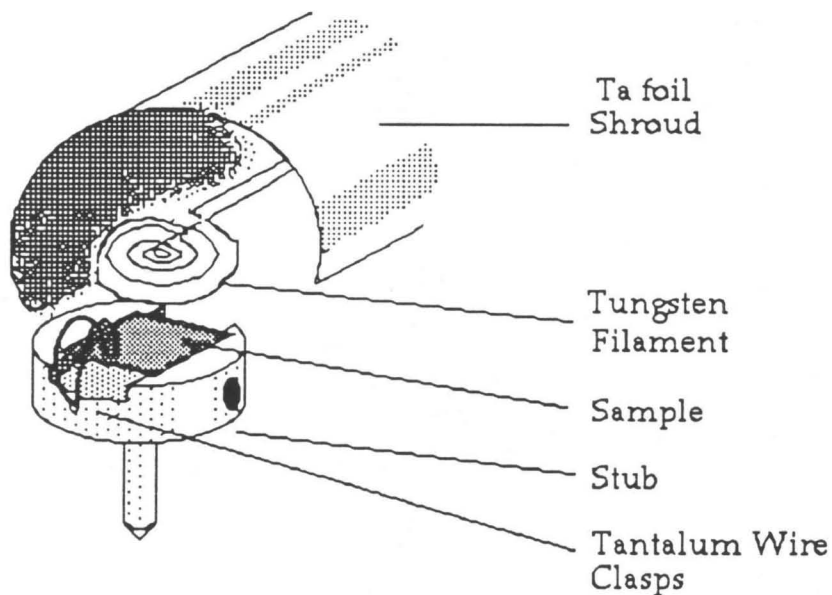


Figure 1: Schematic diagram of the radiative heater. The coiled tungsten filament sits less than 0.5 cm above the sample surface. The entire assembly is surrounded by a highly reflective tantalum foil to reflect the radiation onto the filament and sample. The sample loading area is left open so that the temperature of the filament can be monitored by optical pyrometry. The stub has elevated rails to minimize heat transfer from the sample to the stub by thermal contact. (Drawing by MMJ)

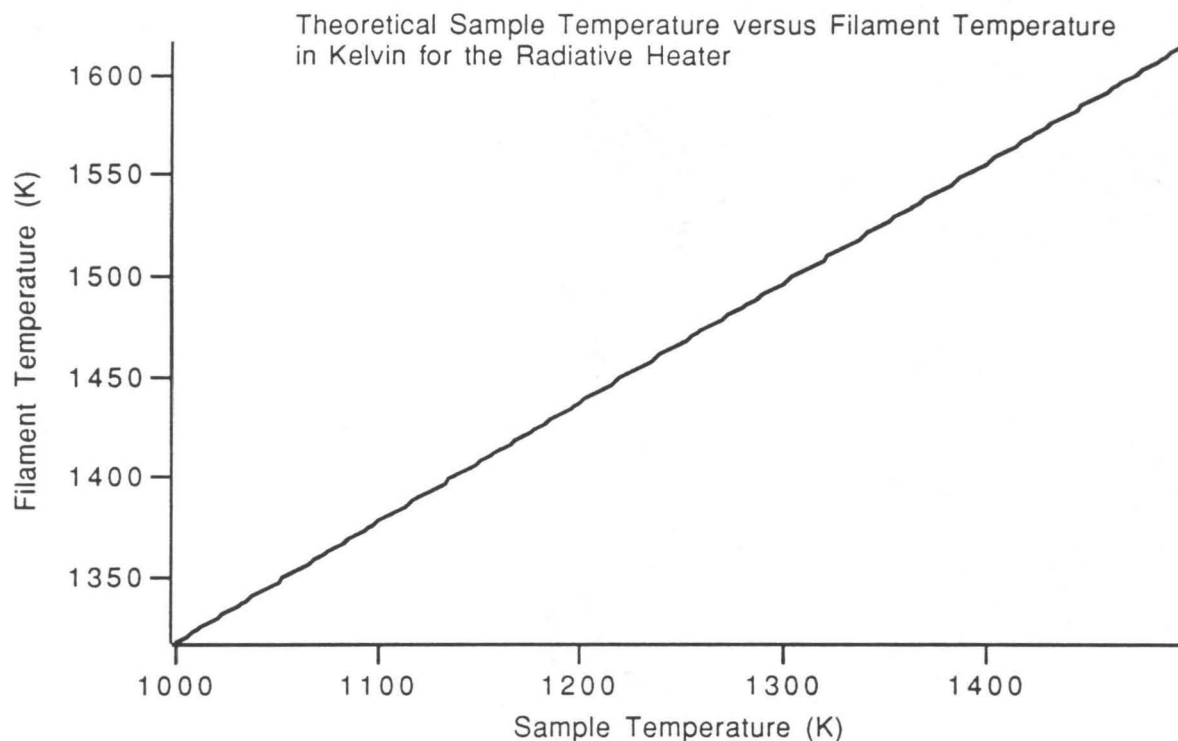


Figure 2: Graph of the filament *versus* sample temperature calculated for the system at equilibrium with the parameters discussed in the text. Note that for this range of temperatures important in the silicon preparation, the sample temperature is 250-300K less than the filament temperature. Since both the sample and filament temperatures are raised to the fourth power, this small area of the curve appears linear.

Power (W) to Raise the Radiative Filament
to a Given Temperature (C or K)

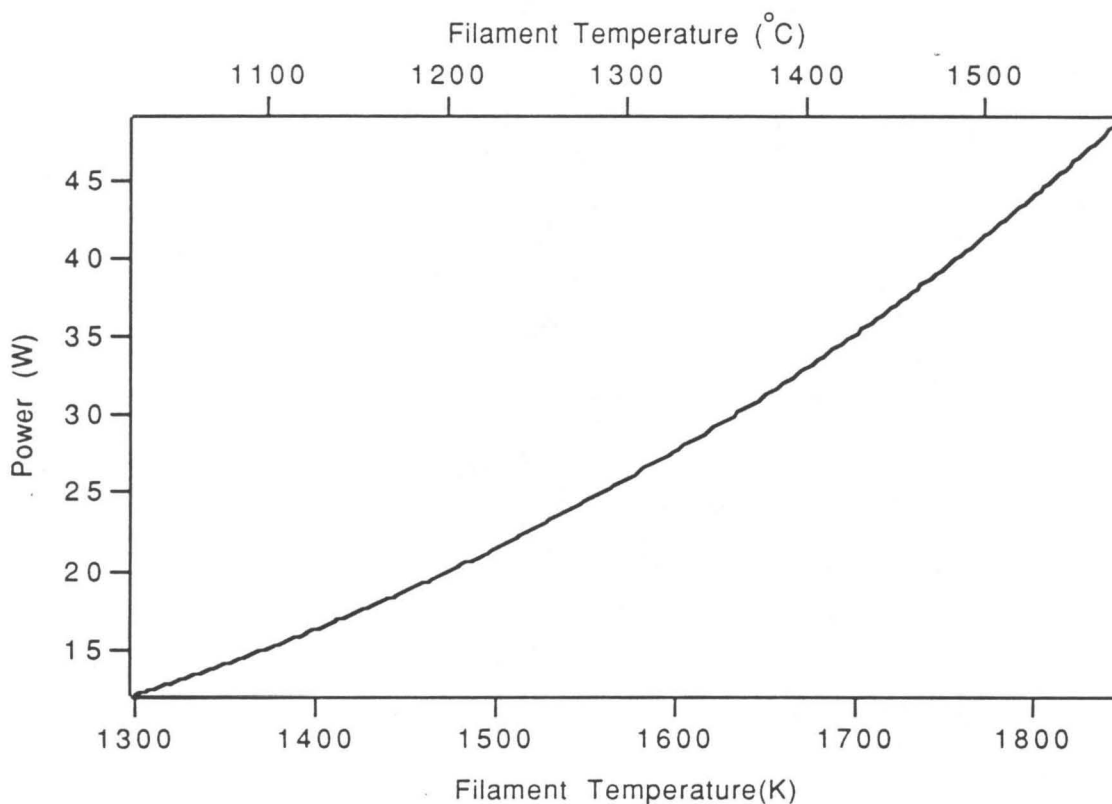


Figure 3: Graph of the power supplied to the filament *versus* the filament temperature calculated as described in the text. The sample temperature is assumed to be approximately 300 degrees less than the filament temperature for the calculation.

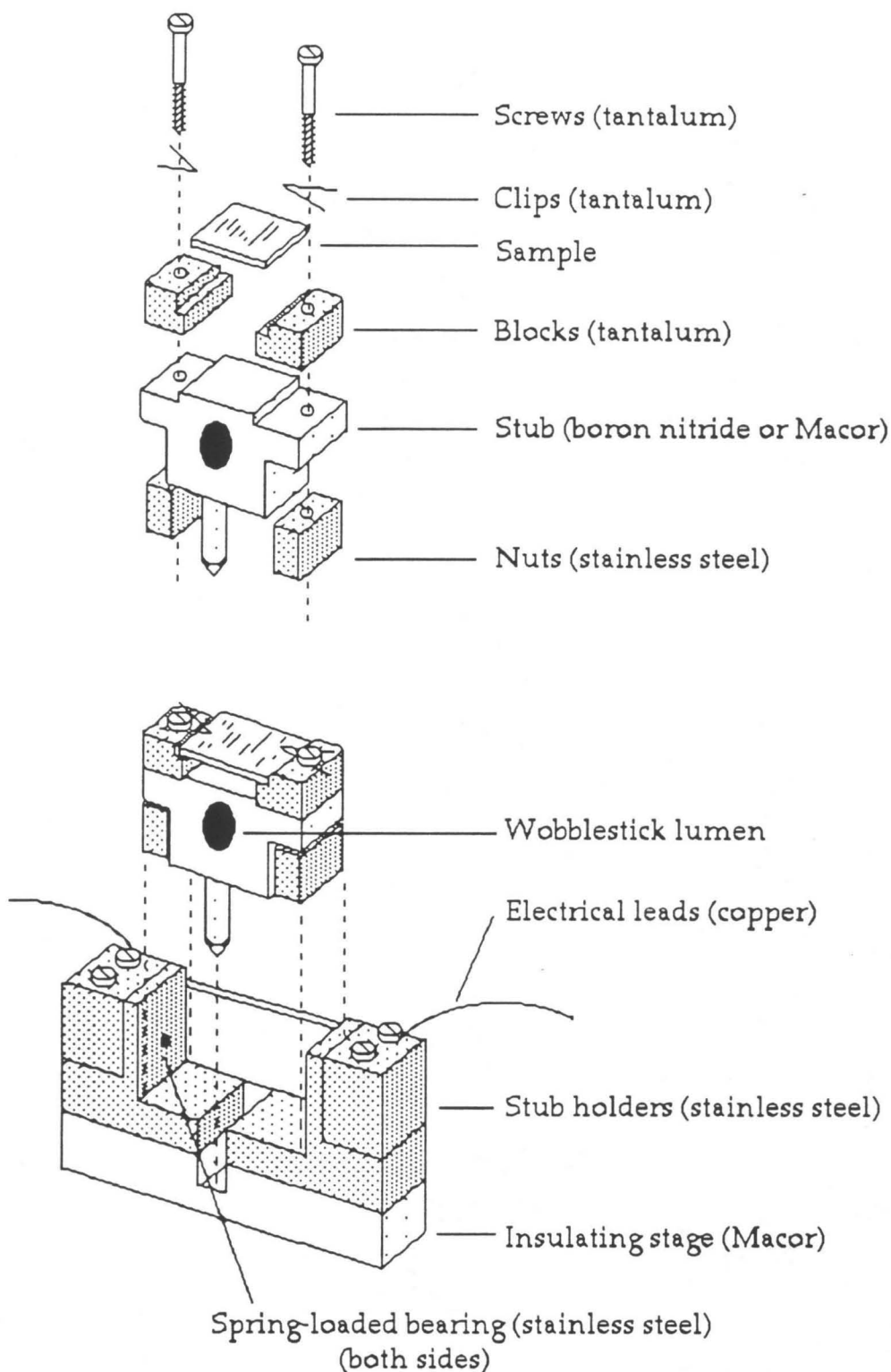


Figure 4: The resistive heater and sample stub assembly (not to scale). The stub is 0.380" wide x 0.250" thick x 0.200" high (stub peg not included). A more detailed description is found in the text. (Drawing by MMJ)

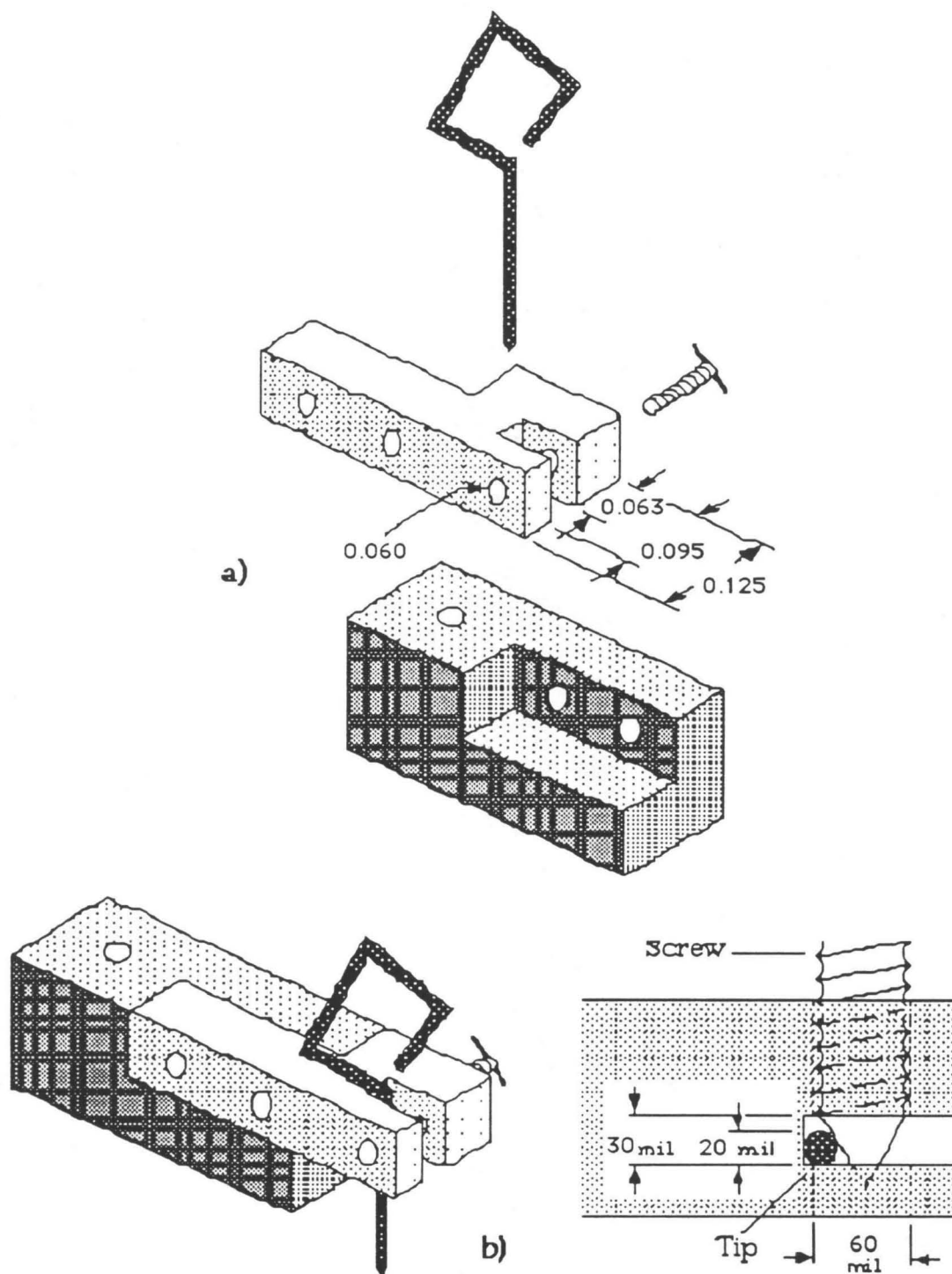


Figure 5: The *in situ* tip-transfer design discussed in the text where a) is unassembled and b) is assembled. The tolerances indicated in b) for the relative positions of the screw and end of tip slot are important for holding the tip firmly in place and are designed for tip shank diameters from 10-20 mil. (Drawing by MMJ)

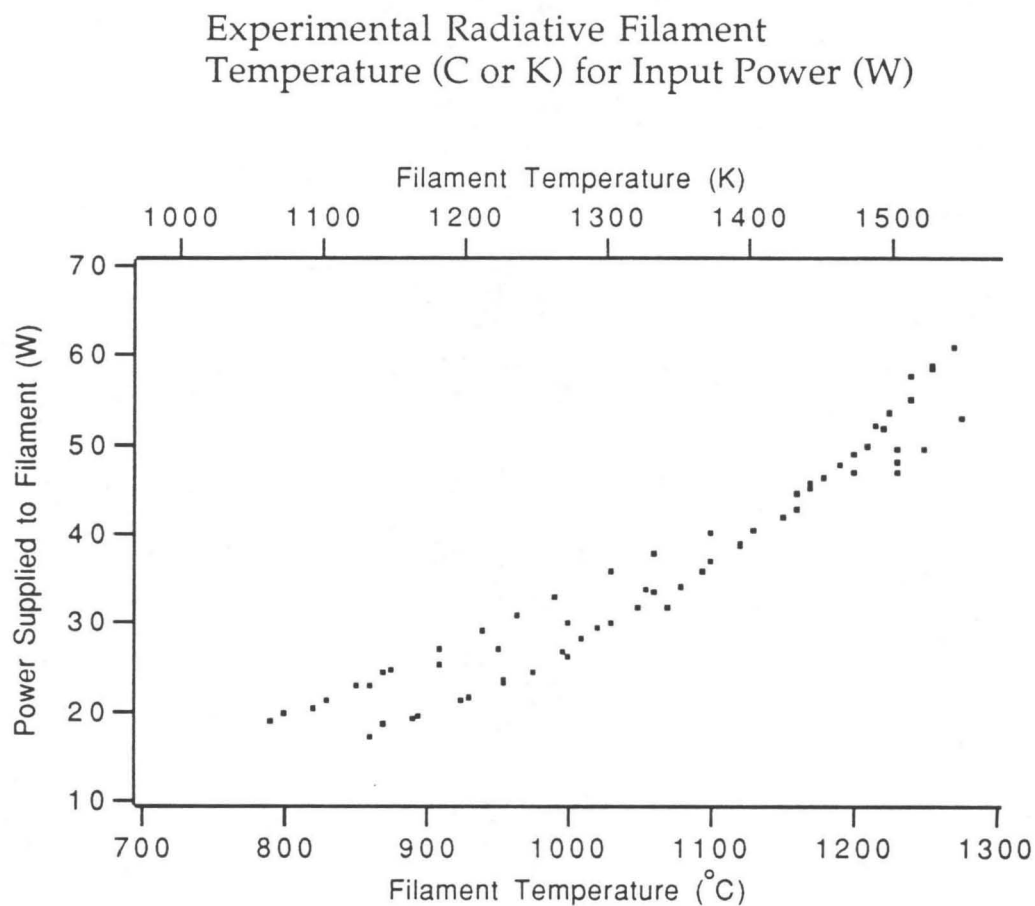


Figure 6: Graph of the experimental values of the filament temperature in Kelvin (top horizontal axis) and °C (bottom horizontal axis) *versus* input power to the tungsten radiative filament. The power was calculated from the measured current and the measured resistance of $0.75\ \Omega$ from I^2R . If the sample temperature is 200-300K less than the filament temperature, these data are in good agreement with the theoretical data of **Figure 3**.

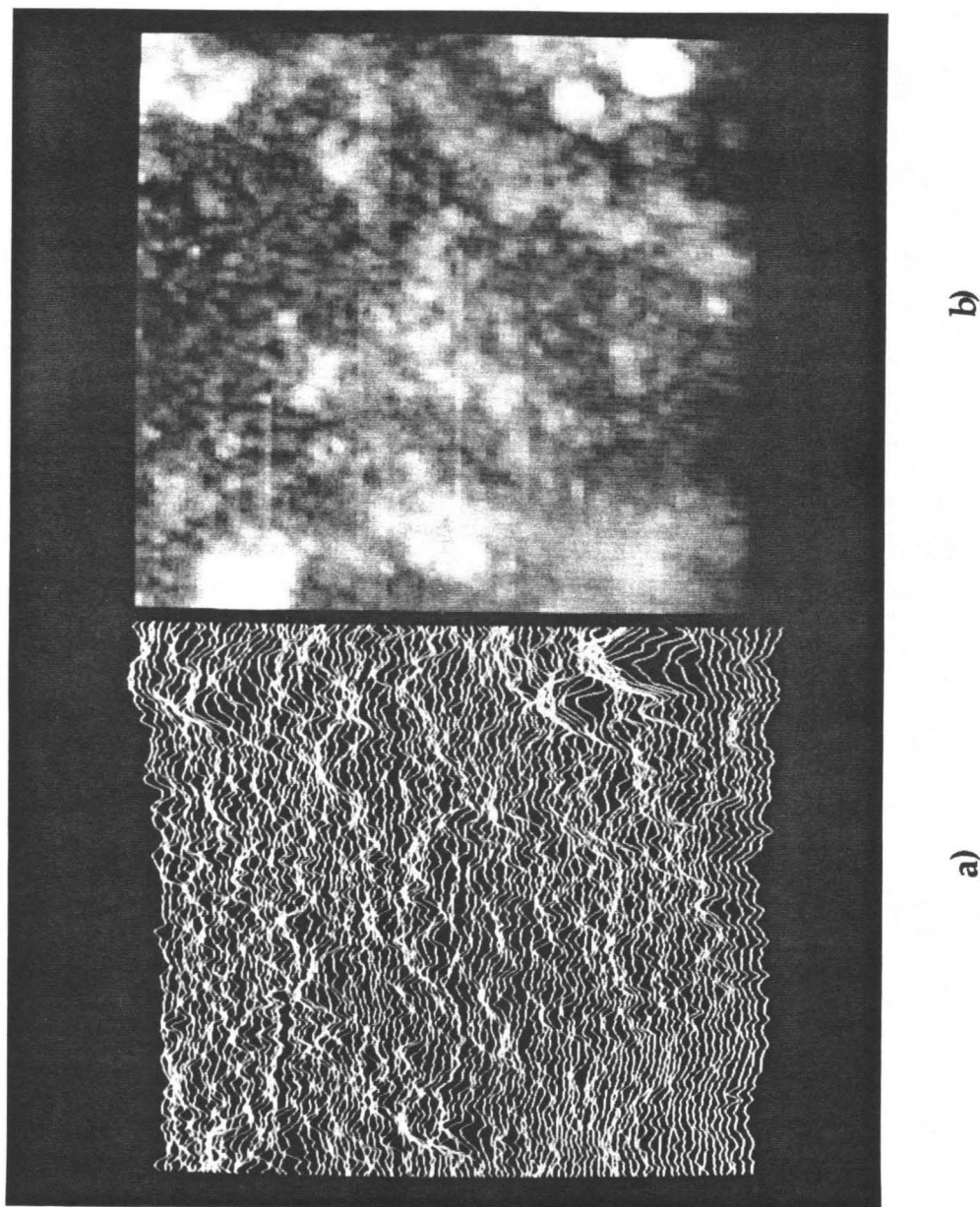


Figure 7: (SI279G) Constant current image as a) line scan and b) gray scale of the silicon surface heated by radiation from a tungsten filament and scanned after 3 days at 1×10^{-9} torr. The image is $370 \text{ \AA} \times 370 \text{ \AA}$ and taken at -2.0 V and 1 nA tunnel current. The total height variation of the image is only $\sim 10 \text{ \AA}$

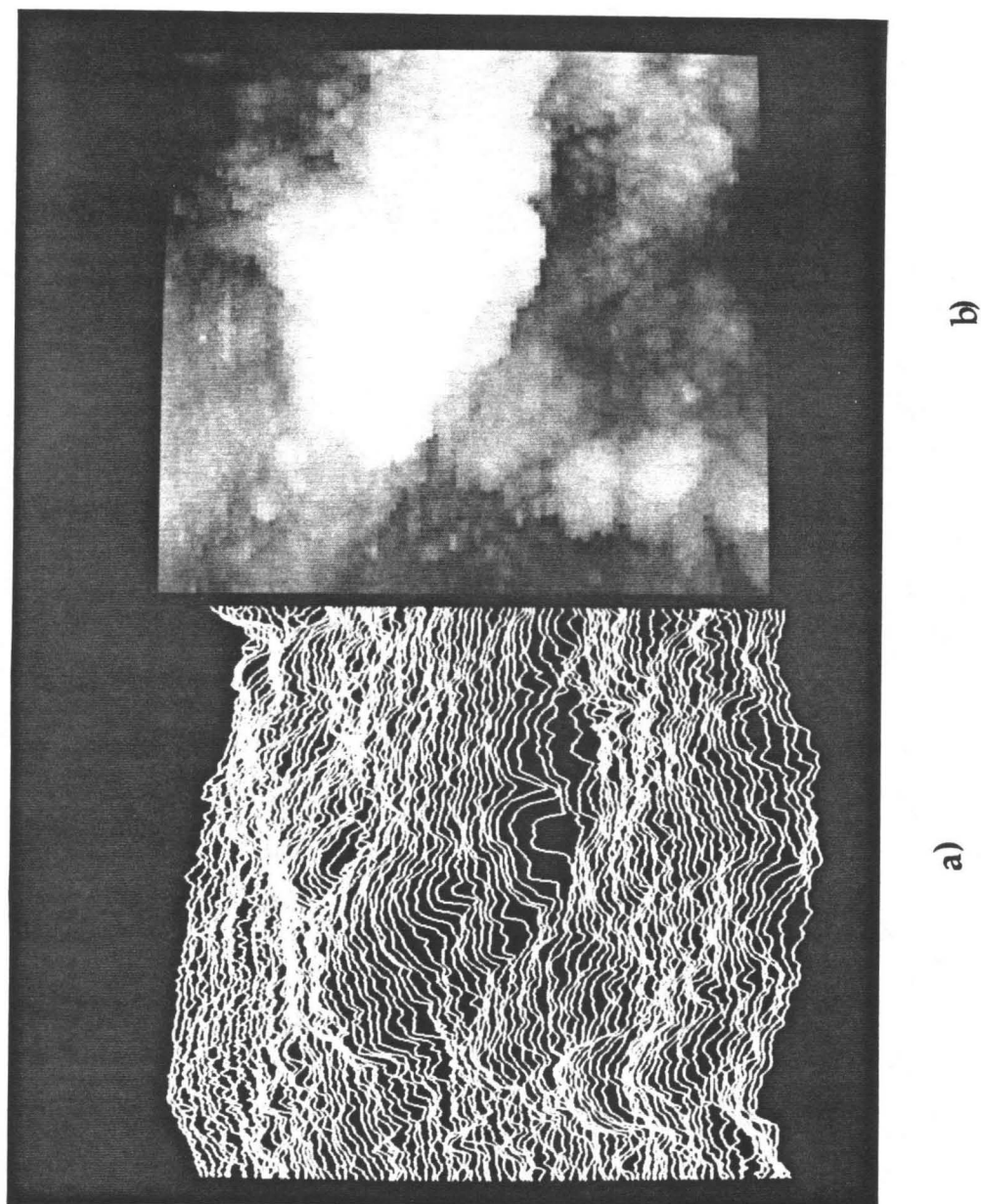


Figure 8: (SI284D) Larger scale $740 \text{ \AA} \times 740 \text{ \AA}$ constant current image as a) line scan and b) gray scale of a silicon surface prepared by radiative heating to a filament temperature $>1300^\circ\text{C}$ with total $P < 3 \times 10^{-9}$ torr. Operating conditions are -3.0 V and 1 nA . Notice, the total height variation is 95 \AA .

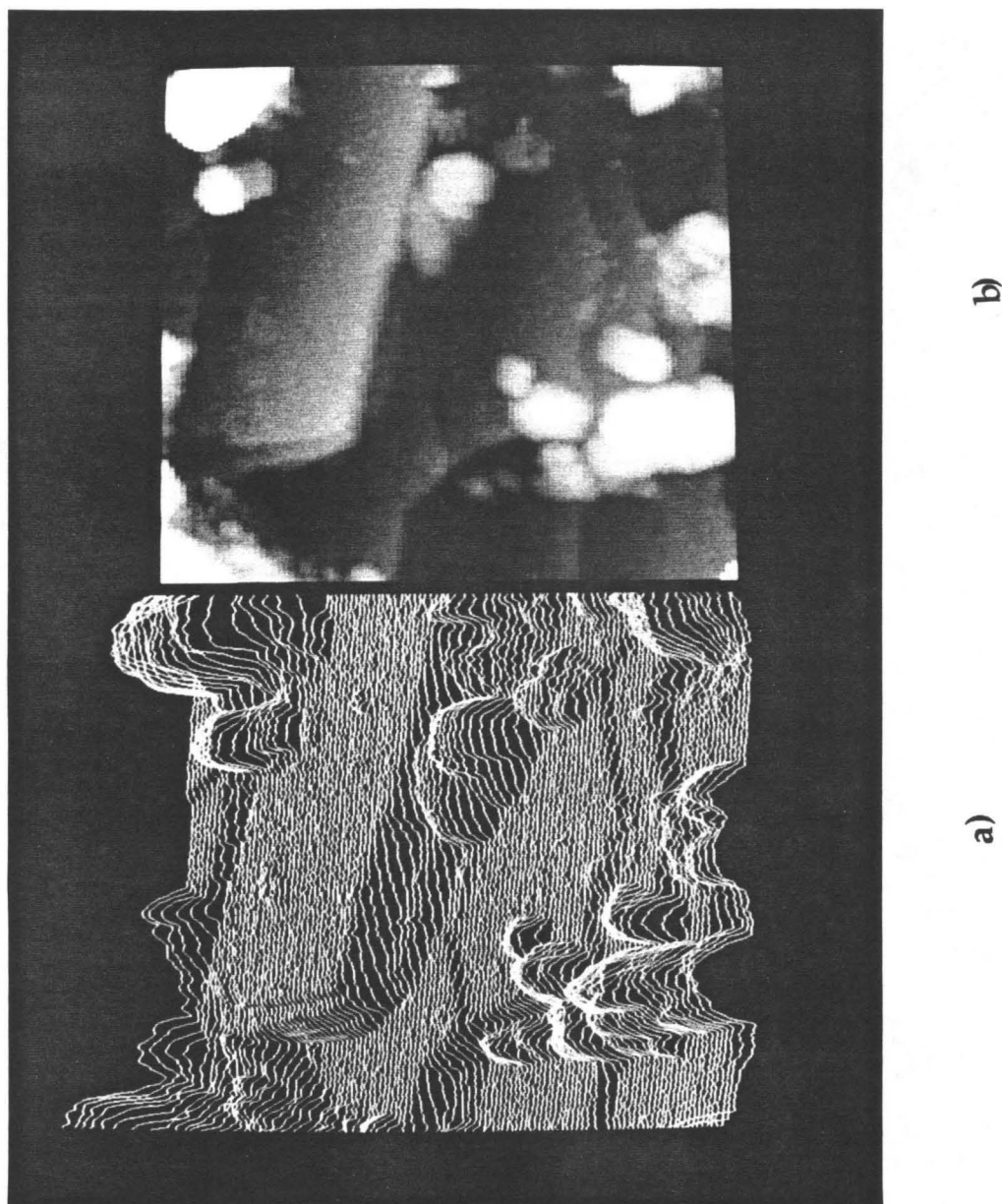


Figure 9: (SI100A) Constant current image as a) line scan and b) gray scale of a 740 Å x 740 Å area on the resistively heated 0.005 Ω-cm, boron doped silicon sample. Total height variation is ~47 Å. The image was taken at +2.0 V and 100 pA. Flat terraces over 400 Å wide are observed.

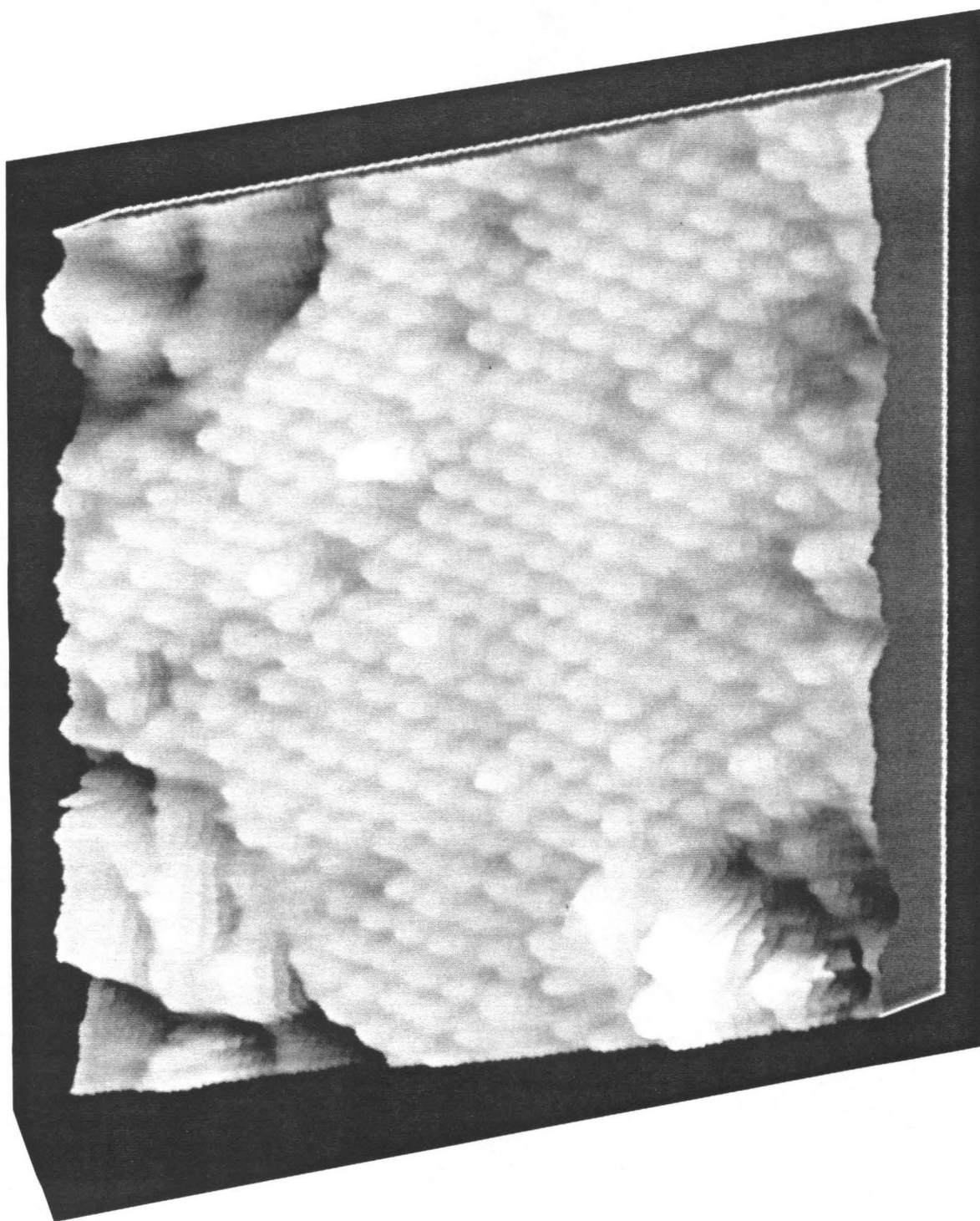
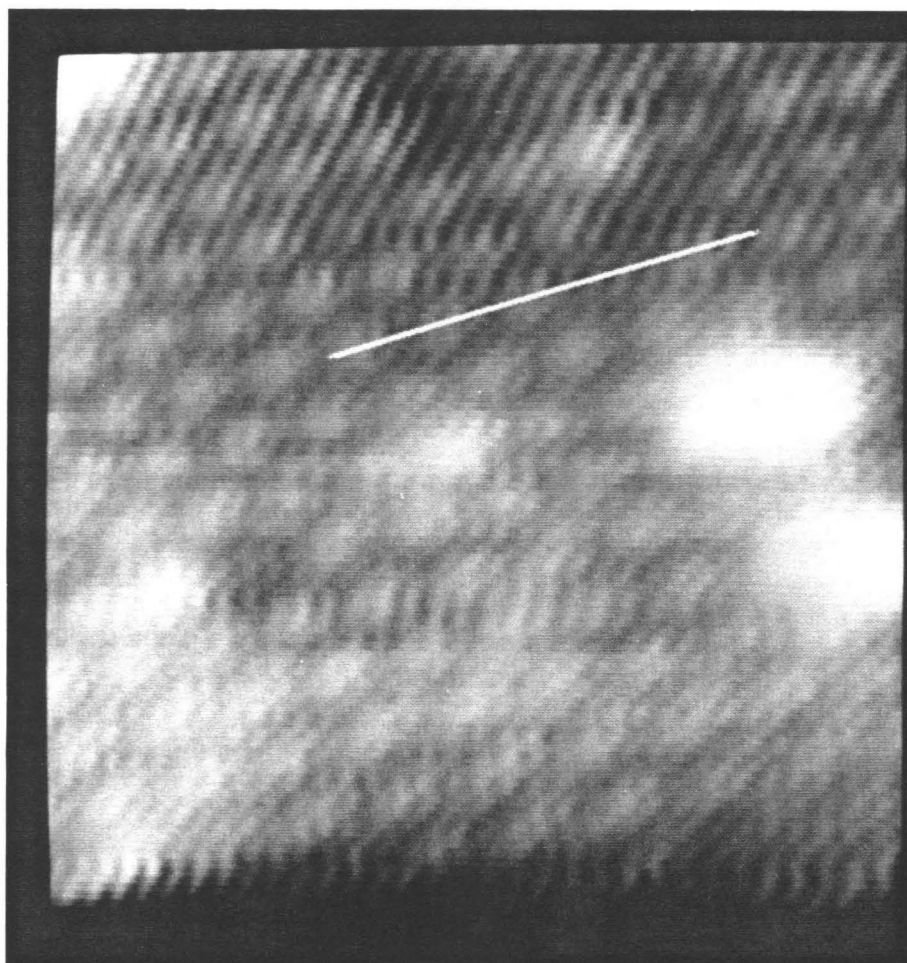


Figure 10: (SI098D) A $100 \text{ \AA} \times 100 \text{ \AA}$ barrier height image, 3-D rendered (shown oriented horizontally on the page) of the highly boron doped silicon surface taken on a flat terrace of the image shown in **Figure 9**. Barrier height modulation was driven at 1 kHz at 30 mV peak-to-peak ($\sim 3 \text{ \AA}$) to the z piezo.



(a)

Figure 11a: (SI098F) Simultaneous $50 \text{ \AA} \times 50 \text{ \AA}$ constant current (a) and barrier height (b-next page) images taken with the same operating conditions as in Figure 10.



(b)

Figure 11b : (SI098F) Simultaneous $50 \text{ \AA} \times 50 \text{ \AA}$ constant current (a-previous page) and barrier height (b) images taken with the same operating conditions as in **Figure 10**.

Plot of Z Corrugation (\AA , diamonds) and Barrier Height (Arbitrary, Circles) for Identical Line Cuts Across the Surface (\AA) for both Topographical and Barrier Height Images

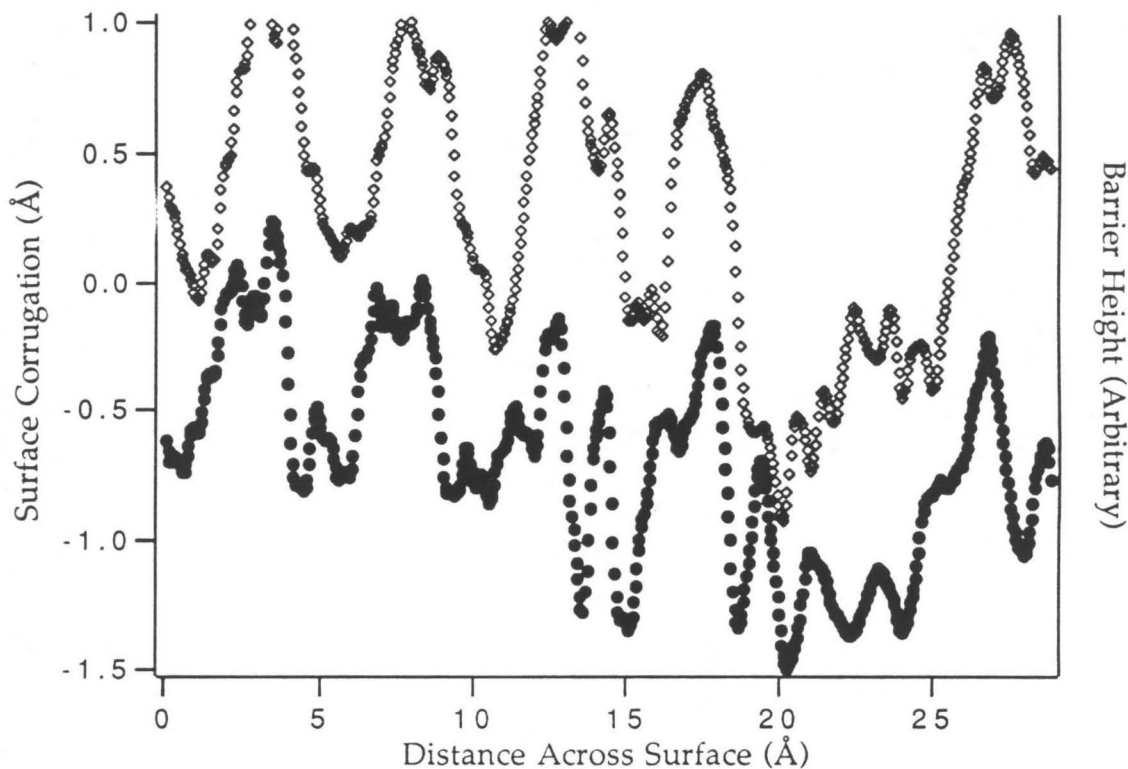
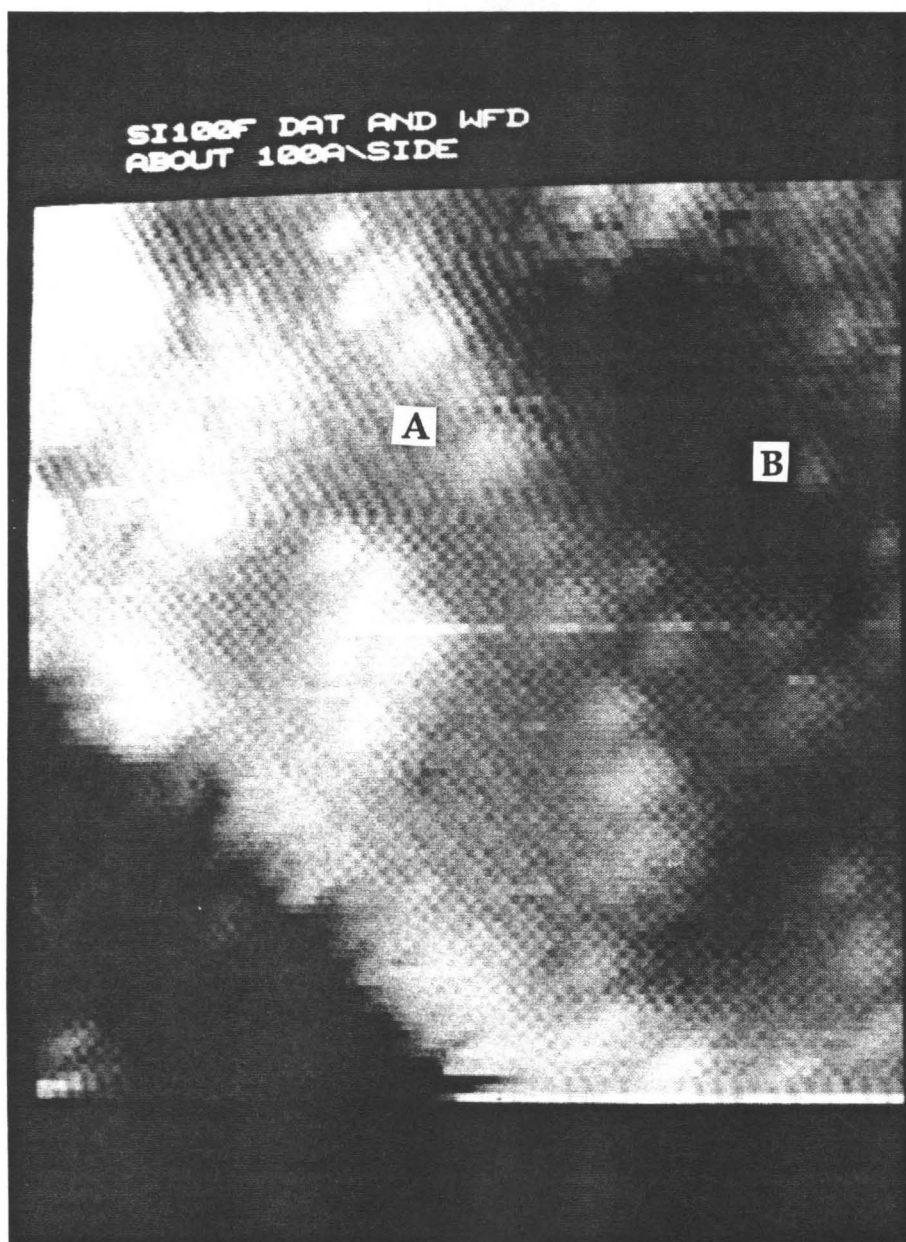
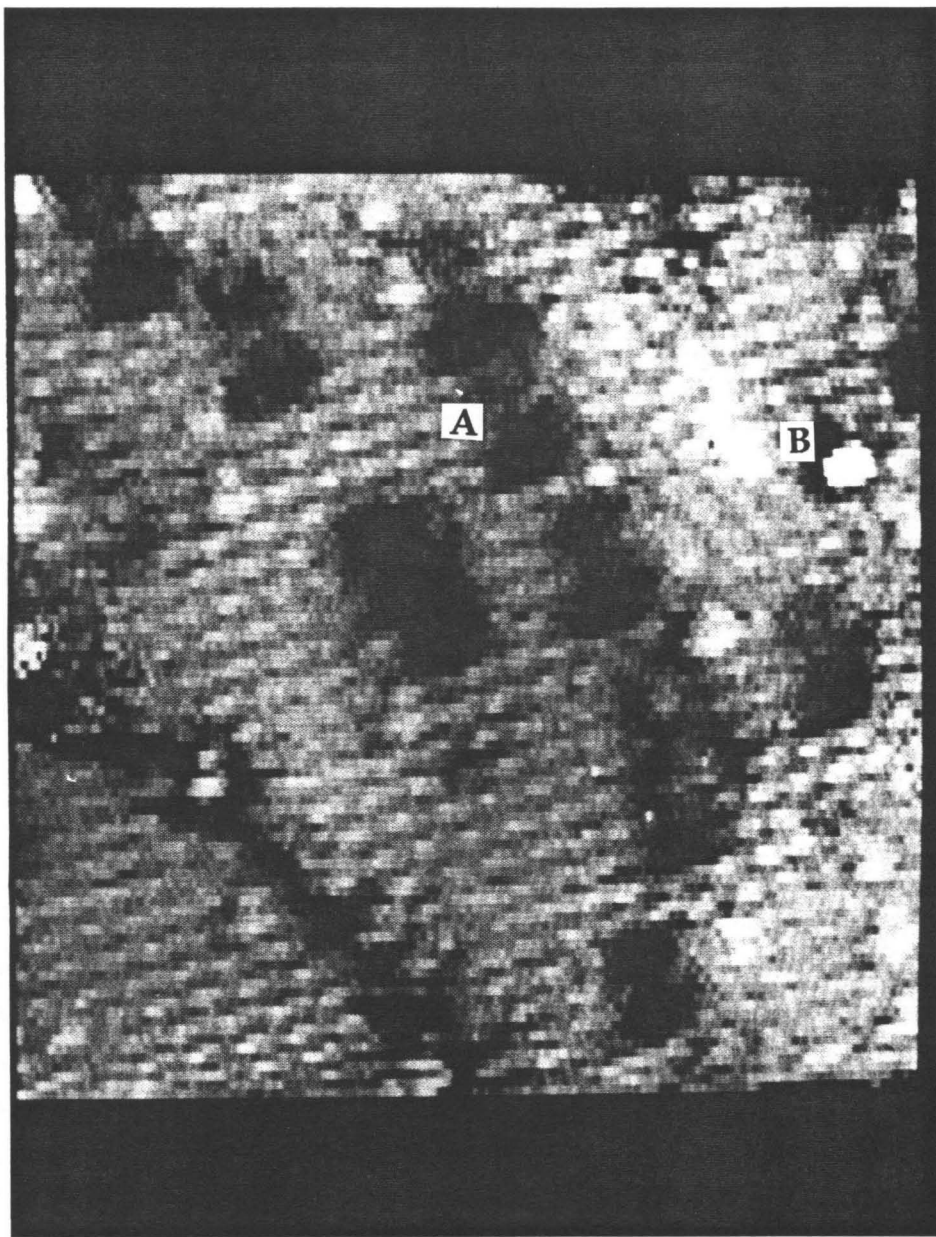


Figure 12: Plots of the topographical height and barrier height measurements taken for the lines through the data shown in **Figure 11**. The barrier height measurement peaks correspond to the topographic peaks, and in this case, the hole appears at a site of decreased barrier height as well.



(a)

Figure 13: (SI100F) Simultaneous $100 \text{ \AA} \times 100 \text{ \AA}$ constant current (a) and barrier height (b-next page) images taken with the same operating conditions as **Figure 9** except that the sample bias was changed to +1.2 V. The difference in brightness between the constant current and barrier height image spots is discussed in the text.



(b)

Figure 13b: (SI100F) Simultaneous $100 \text{ \AA} \times 100 \text{ \AA}$ constant current (a-previous page) and barrier height (b) images taken with the same operating conditions as **Figure 9** except that the sample bias was changed to $+1.2 \text{ V}$.

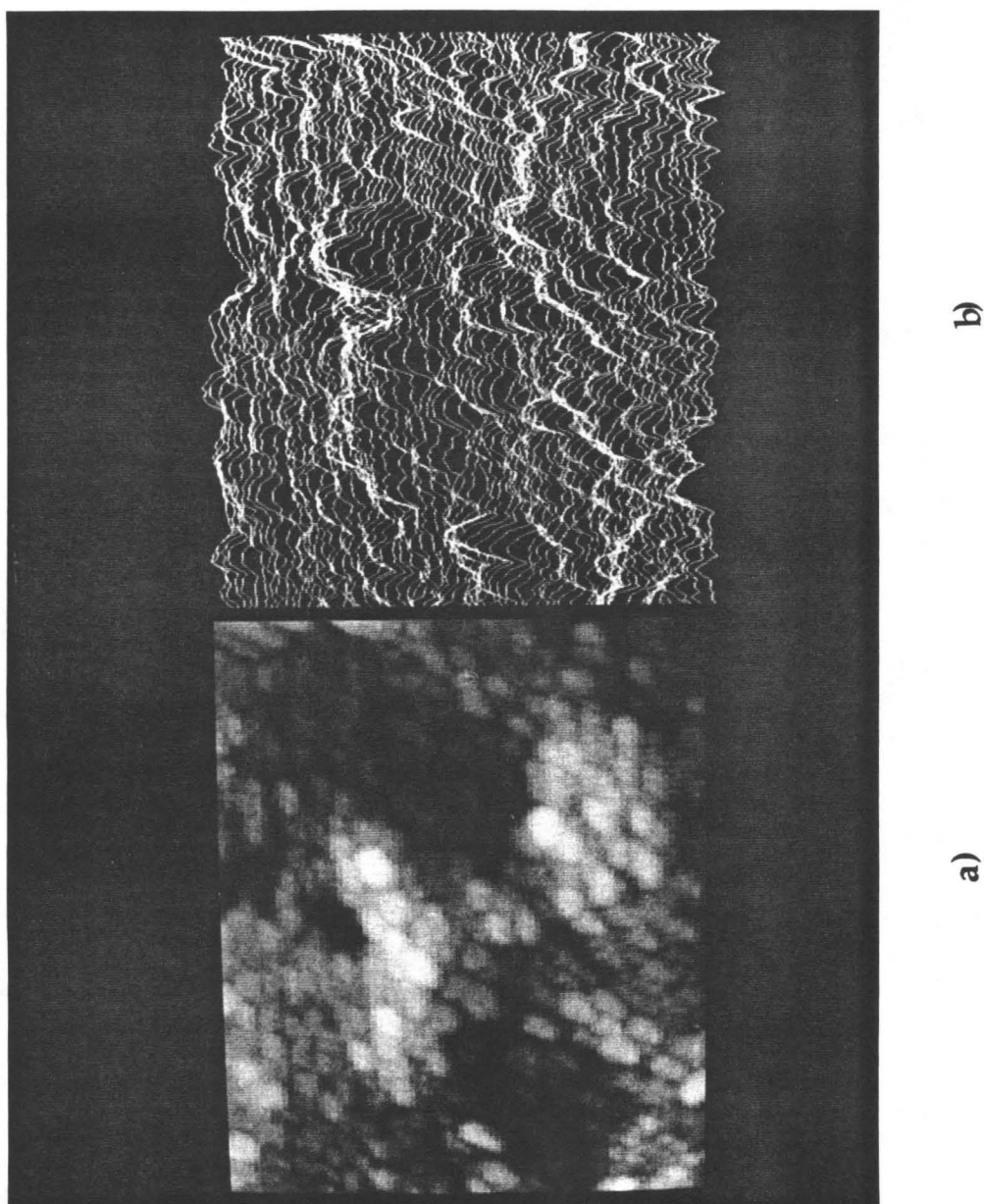


Figure 14: (SI164E) Constant current image as a) gray scale and b) line scan, $1500 \text{ \AA} \times 1200 \text{ \AA}$, of the resistively heated Si(111) surface taken at -1.2 V and 2 nA . The cloud-like mounds are from $60\text{-}80 \text{ \AA}$ wide but appear to the STM to be only up to 10 \AA high. Total z variation in the image is $\sim 40 \text{ \AA}$.

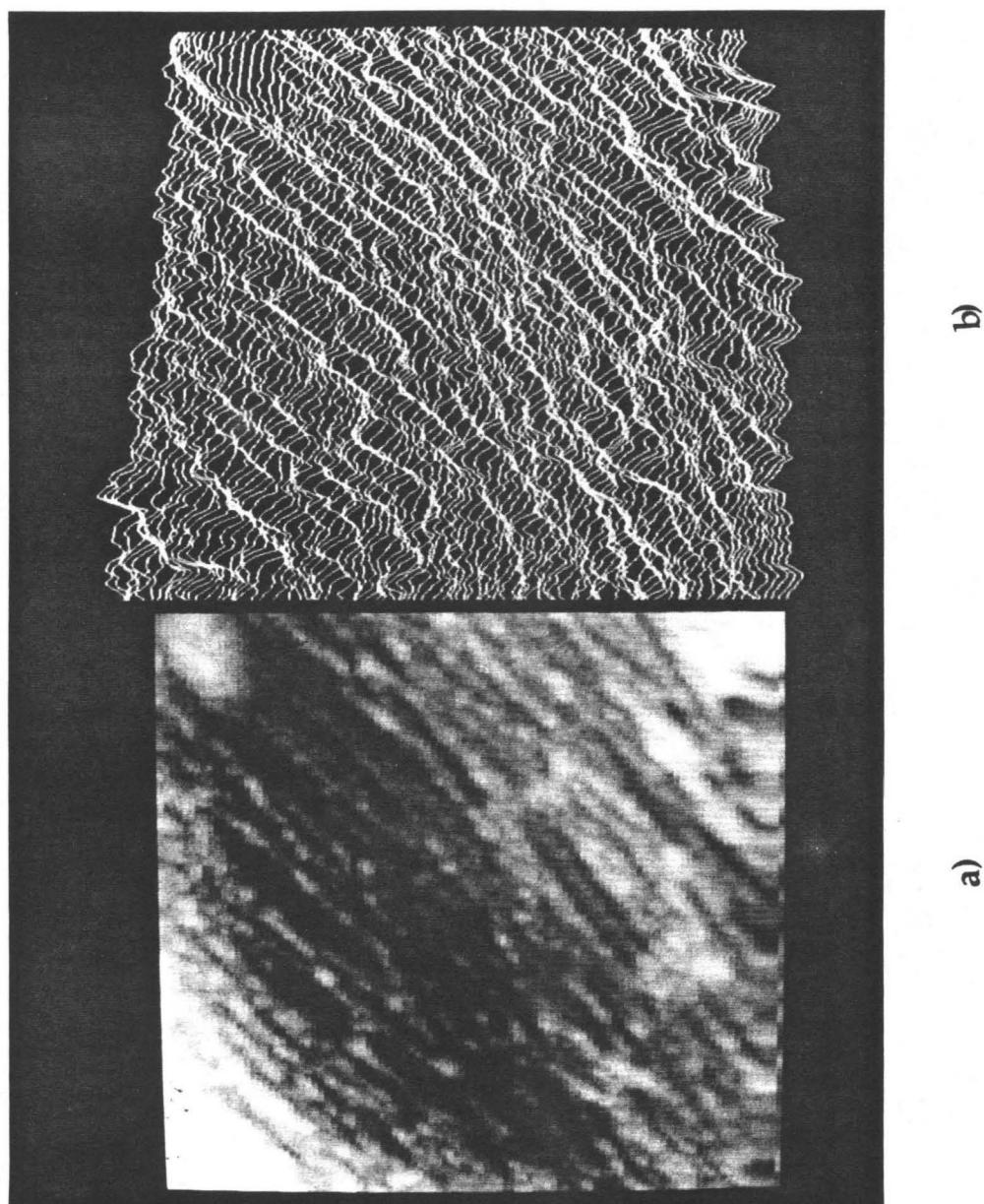


Figure 15: (SI277C) Large 740 Å by 740 Å constant current image as a) gray scale and b) line scan of the 1 Ω-cm (less highly doped) silicon sample after heating to over 1000°C. The image was taken at 1 nA and +1.5 V. These rows are ~350-450 Å wide and are often observed on the surface.

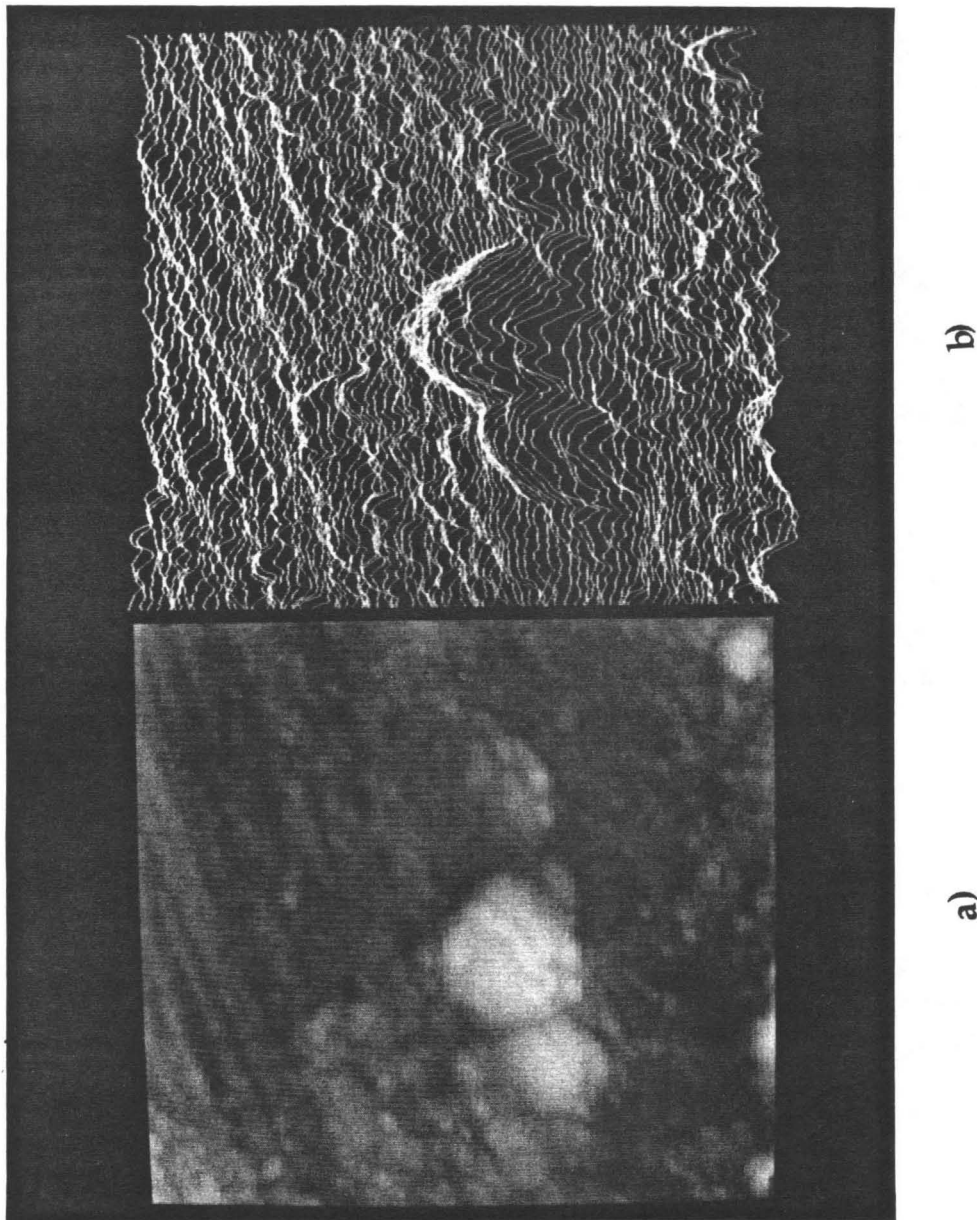
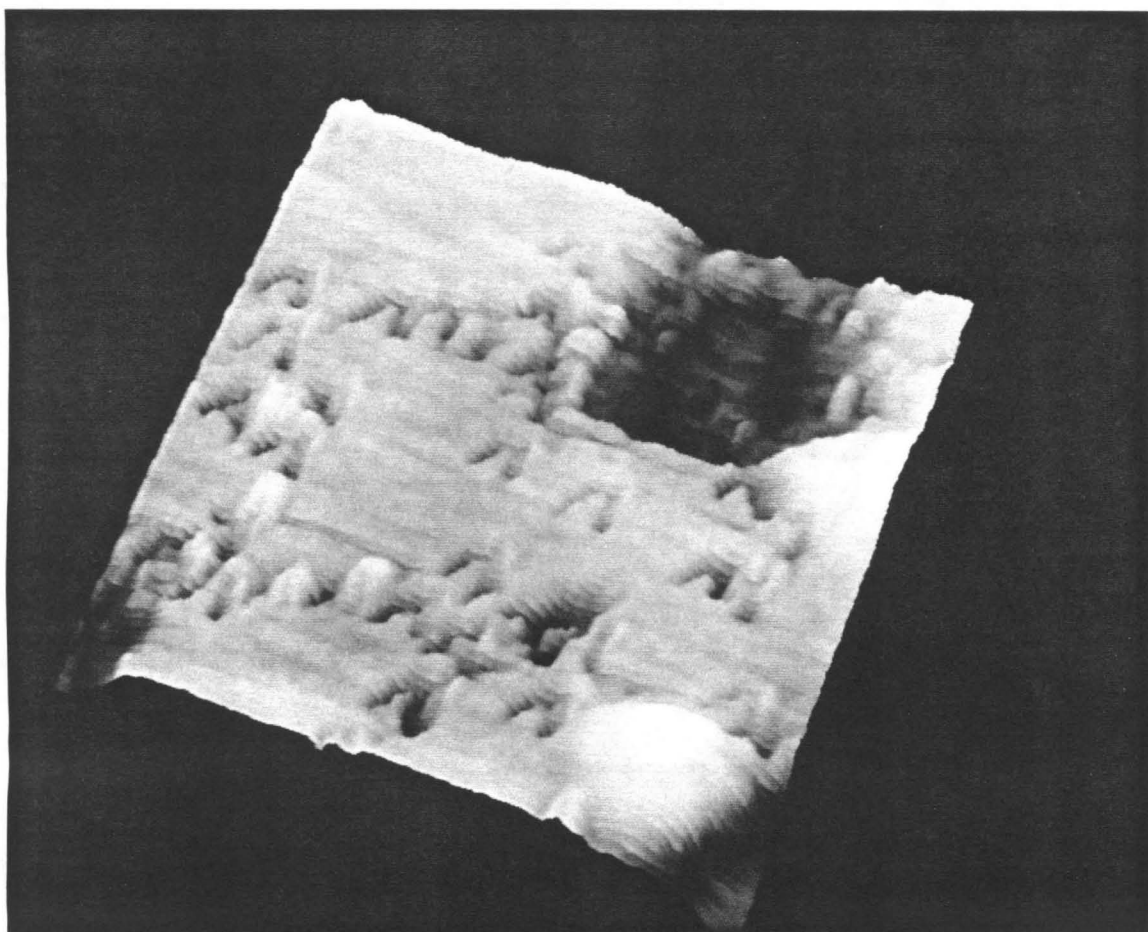


Figure 16: (SI167A) Constant current image as a) gray scale and b) line scan of the resistively heated Si(111) surface showing the transition from rows to mounds. Operating conditions were 1 nA and -3.0 V for the $750 \text{ \AA} \times 750 \text{ \AA}$ image.

Chapter 4

TOPOLOGY, COMPOSITION AND SPECTROSCOPY OF A SYNTHETIC BORON-DOPED DIAMOND



INTRODUCTION

Background

Because of the unique physical properties of diamonds, considerable attention has been given to them for applications ranging from electronics to grinding tools. Interest in these applications has generated research of the basic properties of this semiconductor. The properties of natural diamond include a large band gap with reported values from $\sim 5.4 \text{ eV}^1$ to 5.6 eV^2 , high thermal conductivity ($\sim 20 \text{ W/cm K}$, depending on purity³), a noncorrosive inert surface, high wear resistance and a low dielectric constant of 5.5^4 to 5.66^5 . As with many of the reported physical properties of diamond, the carrier mobility is not an established value, either. The most often reported value for electron mobility is $\mu = 2000 \text{ cm}^2/\text{V s}$ and hole mobility is $1800 \text{ cm}^2/\text{V s}^{6,7}$. Nonetheless, because of its large band gap, diamond is nearly an insulator at room temperature and would consequently be an ideal substance for high-temperature semiconductor applications. With the recent development chemical vapor deposition (CVD) techniques to prepare high-quality diamond films, these properties may be utilized effectively.

Natural diamonds are found in a variety of colors, shapes and purities. The colors range from blue, green, yellow, brown, and chocolate to shades of pink. It is known that boron causes the blue coloration and that nitrogen causes the yellow, but the wide variety of colors resulting from impurity acceptor/donor levels, carbon vacancies, lattice mismatch or defects, are not well characterized. The success of gem-quality diamond synthesis and CVD of diamond thin films should provide samples with known dopants

¹K. Jackson, M. Pederson and J. Harrison *Phys. Rev. B* **41** (18), 12641 (1990) and K. Srikanth, S. Ashok, A. Badzian, T. Badzian and R. Messier *Thin Solid Films* **164**, 187 (1988)

²F. C. Champion *Electronic Properties of Diamond* (Butterworth & Co., Ltd.: London), 25 (1983)

³R. C. Weast and M. J. Astle, eds. *CRC Handbook of Chemistry and Physics* (CRC Press: Boca Raton, FL), E-11 (1981)

⁴K. Srikanth, S. Ashok, A. Badzian, T. Badzian and R. Messier *Thin Solid Films* **164**, 187 (1988)

⁵M. I. Eremets *Semicon. Sci. Technol.* **6**, 439 (1991)

⁶M. W. Geis, D. D. Rathman, D. J. Ehrlich, R. A. Murphy and W. T. Lindley *IEEE Electron Device Lett.* **EDL-8** (8), 341 (1987)

⁷H. Shiomi, H. Nakahata, T. Imai, Y. Nishibayashi and N. Fujimori *J. Jap. Appl. Phys.* **28** (5), 758 (1989)

(impurities), which can be used as a basis for understanding the physical properties.

A classification system for natural diamonds has been established based on measurable properties and is only briefly described here to put this study into the appropriate context. The major division is a distinction between Type I and Type II diamonds. Type I diamonds are transparent, show little internal zoning and may have a slight coloration from yellow to brown. The Type Ia diamonds have nitrogen concentrations up to $4 \times 10^{20} \text{ cm}^{-3}$ primarily found as two or more associated atoms that produce distinct IR absorption at 1282 cm^{-1} and 1365 cm^{-1} and have no paramagnetic properties. The much more rare Type Ib diamonds have single nitrogen atoms that substitute for carbon and act as a paramagnetic center. Qualitatively, the Type I diamonds rarely exhibit large (100) faces, tend to be octahedral or tetrahedral in shape and have *n*-type semiconducting properties⁸.

Type II diamonds tend to be more cubic (rather than tetrahedral or octahedral), and although they often contain small nitrogen concentrations, they do not have the IR absorption line at 1282 cm^{-1} . The Type IIa diamonds have the purest crystallinity and absorb at $\sim 2000 \text{ cm}^{-1}$ ($5 \mu\text{m}$) in the IR. Type IIb diamonds are much more rare and are characterized by a low electrical resistivity. While typical diamonds have resistivities of 10^{11} - $10^{14} \Omega\text{-cm}$ at 25°C , some Type IIb diamonds have a resistivity as low as $\sim 100 \Omega\text{-cm}$ over areas of highly concentrated dopant. Their blue or grey coloration is attributed to interstitially substituted boron atoms that cause the diamond semiconductor to be *p*-type⁹.

Although some of the more common diamond inclusions have been characterized, the location and effect of various impurities and defects on the physical and electronic properties are still not well known. Much interest has been focused on developing synthetic diamonds and diamond thin films in which the physical and electronic properties can be manipulated. General Electric (GE) has developed, in addition to much work on thin-film and isotopically pure diamond preparation, a process to make large gem-quality diamonds by a high pressure, high temperature technique¹⁰. A dopant can be

⁸Yu L. Orlov *The Minerology of the Diamond* (John Wiley & Sons: New York), 141 (1977)

⁹R. H. Wentorf, Jr. and H. P. Bovenkerk *J. Chem. Phys.* **36** (8), 1987 (1962)

¹⁰F. P. Bundy, H. T. Hall, H. M. Strong and R. H. Wentorf *Nature* **4471**, 51 (1955) and H. P. Bovenkerk, F. P. Bundy, H. T. Hall, H. M. Strong and R. H. Wentorf, Jr. *Nature* **184**, 1094 (1959)

added to the metal catalyst melt, which will be incorporated into the diamond matrix as it is grown to provide carriers to the semiconductor⁹.

The electronic properties of diamond are even less well characterized than the optical, morphological and compositional properties because they depend on knowledge of the latter for interpretation and because so few conductive diamonds exist. Current-voltage (IV) spectroscopy is often used in device applications to determine whether the nature of a metal-semiconductor contact is ohmic (having a linear response of the current to applied voltage) or Schottky (having a specific nonlinear response of the current to applied voltage). When the metal and semiconductor are not in intimate contact, as in the geometry of the scanning tunneling microscope, the IV curves demonstrate Schottky properties, given ideal insulating gap characteristics, as described in detail by thermionic emission in metal-insulator-semiconductor (MIS) theory¹¹.

Little is known about the microscopic details of the growth process, either of natural or synthetic gem-quality diamonds, or about the exact location of the dopant in the resultant crystal. However, the need to regulate the carbon flux carefully has been determined necessary to decrease the probability of spontaneous nucleation or surface graphitization¹². The unequivocal determination of the various dopants' location in the diamond lattice (interstitial substitution, segregation or formation of small clusters) would be useful in order to characterize and predict the dopants' effect on electrical properties. Furthermore, macroscopic images of the resultant faces have shown various structures, but the microscopic origins of these structures are not known.

Scanning tunneling microscopy (STM) is a tool that is potentially useful in determining surface growth characteristics and perhaps the actual location of the surface carbon and impurity atoms. Because of the insulating properties of natural diamond at room temperature, STM images of its structure have not been published to date. However, a few rough images of

¹¹S. M. Sze *Semiconductor Devices: Physics and Technology* (John Wiley & Sons: New York) (1985)

¹²H. M. Strong and R. M. Chrenko *J. Phys. Chem.* 75 (12), 1838 (1971)

CVD diamond films, boron-doped¹³, prepared in a hot-filament reactor¹⁴ and perhaps dimer rows on epitaxially grown diamond¹⁵ have been shown. Except for the last reference, these STM images present data that is also available from SEM micrographs.

Purpose

This chapter presents a series of experiments to characterize the topology, composition and current voltage characteristics of semiconducting diamond. Initially, STM imaging of a natural Type IIb diamond was attempted but was not successful because of the low conductivity at room temperature. A significant tunnel current could not be drawn without crashing the tip into the surface. General Electric (GE) loaned Dr. George Rossman a number of highly boron-doped diamonds, and the deepest blue sample with the least obvious flaws and inclusions was chosen for the STM analyses. A photograph of the diamond is shown in **Figure 1**. This diamond will be referred to as the "primary" or "original" diamond in subsequent sections. Segregation of dopants or inclusions was not noticeable on this diamond, and the coloration appeared uniform. This homogeneity was not observed in the other diamonds in the batch that had obvious flaws.

Photographing the primary diamond sample is difficult because of its opacity, but the large, triangular face with cut corners which was examined in this chapter is clearly shown in the figure. This (111) surface was studied by Laue diffraction and optical goniometry and examined by scanning tunneling microscopy and spectroscopy. Further experiments with x-ray photoemission spectroscopy (XPS) on this diamond and secondary ion mass spectroscopy (SIMS) on other Type IIb GE boron-doped diamonds contributed to the compositional analysis.

Scanning tunneling microscopy images of the as-grown face as well as current-voltage spectroscopy of a synthetic diamond surface are presented for the first time. This spectroscopy confirms the rectifying properties of the

¹³M. P. Everson and M. A. Tamor *J. Vac. Sci. Technol.* B9 (3), 1570 (1991)

¹⁴H.-G. Busmann, H. Sprang, I. V. Hertal, W. Zimmermann-Edling and H.-J. Güntherodt *Appl. Phys. Lett.* 59 (3), 295 (1991)

¹⁵Takashi Tsuno, T. Imai, Y. Nishibayashi, K. Hamada and N. Fumimori *Jap. J. or Appl. Phys.* 30 (5), 1063 (1991)

doped diamond and supports recent reports that suggest that the effect of oxygen on the surface is to pin the Fermi level.

EXPERIMENT

Compositional and Orientational Analyses

The surface studied by the STM was examined by Laue diffraction at the Caltech X-Ray Facility. Optical goniometry was used to examine the angles between the adjacent faces.

Secondary ion mass spectroscopy (related to ion microprobe analysis that has higher mass resolution) was performed by Dr. Robert G. Wilson of Hughes Research Laboratories in Cameca magnetic sector instruments to determine the elemental components of similarly prepared GE boron-doped diamonds. The analyzed diamonds are presumed to be less highly boron-doped than the diamond examined by STM because of their obviously less intense and less uniform blue color. The relative sensitivity factor (RSF) for the ionization of elements embedded in a diamond lattice has been determined from implanted standards in natural type IIa diamonds¹⁶ using the incident ions Cs⁺ (measuring negative secondary ions) and O⁻ (measuring positive secondary ions). The quantitative distribution of elements in an uncharacterized diamond sample can be determined from each SIMS analysis using the established RSF's.

A more careful analysis of the H and B concentration was performed using the cesium primary beam and measuring negative secondary ions, again on a diamond of lesser quality, but from the same "batch" as the original diamond examined by STM. Ion milling spot sizes were approximately 60 μm in diameter and 10 μm deep. A matrix density of $1 \times 10^{23} \text{ cm}^{-3}$ is assumed.

XPS studies were performed on the original diamond sample with Dr. Richard Vasquez at the Jet Propulsion Laboratory (JPL). The primary beam of X rays was derived from the Al K α emission at 1486 eV. A gold foil was used to make contact with the surface, and no surface charging was observed as noted by the binding energy of the C1s peak at 284.4 eV. A spot size of 600 μm

¹⁶R. G. Wilson and S. W. Novak *J. Appl. Phys.* 69 (1), 466 (1991)

was used for the large energy window scans (Beam energy (BE) = 0 to 1100 eV) and valence band edge scans (BE = 0 to 33 eV). The scans in the region of the C1s peak (BE = 280 to 295 eV) were taken on a 300 μ m diameter spot.

The surface was examined after each of the following procedures was performed: A) perchloric acid etch and storage in ethanol B) subsequent HF etch with ethanol rinse and C) subsequent Ar⁺ etch of B at ultrahigh vacuum (UHV). A second study was performed on the D) (111) face and E) (100) face after sonicating the diamond in trichloroethylene (TCE), then in ethanol, and boiling it in HF for 2 hours. The diamond was subsequently sonicated in ethanol for 2 minutes and stored in ethanol for transfer to JPL.

Scanning Tunneling Microscopy and Surface Analyses

For the STM studies, the diamond was boiled in HNO₃, H₂SO₄ or HF and kept under ethanol until admitted into the STM chamber under nitrogen flow. For imaging and spectroscopy in vacuum, the diamond was subsequently heated to temperatures up to ~500°C in UHV. Originally, the diamond was mounted on stainless steel, copper or tantalum sample stubs using indium, a vacuum compatible solder. To increase chances of adequate conductivity, a thin indium lead was also drawn to the top of the large sample surface. To insure ohmic contact, the contact medium was subsequently changed to silver paste or a colloidal graphite¹⁷.

STM imaging was done in an ultrahigh vacuum (UHV) chamber with a base pressure <10⁻¹⁰ torr at the time of operation. Tips were made by ac etching 0.020 inch diameter tungsten wire (6 Vac, 10 A). Images were taken at 100 pA or 1 nA tunneling current at the voltages indicated in the images. Each image was taken in both directions (left to right and right to left) to insure reproducibility. The sample was mounted in the STM on a translator (louse) so that a wide area with numerous scan windows could be examined without breaking vacuum.

Current *versus* voltage (IV) spectroscopic scans were taken at UHV and at ambient pressure. A set of IV's are taken at a series of tip-sample separations defined by the set point current and sample bias. In these investigations, the sample bias is the variable parameter, so that an increase in voltage between successive IV scans results in an increased separation.

¹⁷Dr. Brad Pate, Telephone conversation, June 1991 and Yusuke Mori, H. Kwarada and A. Hiraki *Appl. Phys. Lett.* 58 (9), 940 (1990)

IV's were taken using tips of either a cut platinum wire or etched tungsten wire as indicated.

RESULTS

Macroscopic Diamond Characterization

A photograph of the diamond is shown in **Figure 1**. Its shape is cubo-octahedron¹⁸ having both (100) and (110) square-sided and (111) trigonal faces visible, although the square faces are smaller, so its polyhedral character tends toward the octahedral. Optically, it is almost opaque presumably because of the high concentration of boron dopant creating absorption in the visible spectrum. This diamond was grown in a liquid metal melt with GE proprietary catalysts under conditions as reviewed by Strong¹⁹. Thus, a complete compositional analysis from GE was not possible. Results of analyses of similar diamonds from GE are discussed below (presumably, these diamonds are from the same batch as mentioned earlier).

Laue Diffraction and Optical Goniometry

The (111) orientation was confirmed by Laue diffraction. The diffraction pattern shown in **Figure 2** clearly shows the expected three-fold symmetry of the (111) face upon which all subsequent analyses were performed.

Table I: Measured and Reference Angles Between Crystallographic Planes

<i>Identified Plane</i>	<i>Angle Between Plane and (111)</i>	<i>Measured Angle</i>
(110)	35°16'	35°0'
(100)	54°44'	54°42'
(111)	180°0'	180°0'

Clear, sharp cross hairs were observed in the optical goniometer, indicating good reflection and allowing for precise measurement of angles between the planes. The results of the optical goniometry are shown in **Table I**, which presents the identification of the major faces expected by macroscopic

¹⁸Koji Kobashi, Kozo Nishimura, Yosh Kawate and Takefumi Horiuchi *Physical Review B* 38(6), 4067 (1988)

¹⁹H. M. Strong *Am. J. Phys.* 57 (9), 794 (1989) and H. M. Strong and R. E. Hanneman *J. Chem. Phys.* 46 (9), 3668 (1967)

geometric symmetries⁸ and verification of the assigned (111) face. A number of smaller faces were measured, but not identified.

Secondary Ion Mass Spectroscopy

The results of SIMS investigations of diamonds from the same batch but not including the original diamond are shown in **Table II**. These diamonds do not have as deep blue coloration, indicating less boron, but they should contain a qualitative representation of the impurities encountered in the original diamond sample. As indicated, the top 10 μm of the diamond surface are very heterogeneous.

Table II: **Approximate Impurity Densities in a GE Synthetic Diamond by SIMS and Known RSF's in ppm (or %)**

<i>Impurity</i>	<i>"clear" spot</i>	<i>"dark" spot</i>	<i>"dirty" spot</i>
H	1000	-	3
B	15	150	1500 (0.15)
O	200	-	3000 (0.3)
Na	0.1	4	6
Mg	-	18	10
Al	30	40	400
Si	2	500	2000 (0.2)
Cl	-	-	50
K	0.005	2	2
Ca	0.004	0.4	0.5
Ti	0.004	1	500
Fe	-	400	(35)
Co	-	1	4000 (0.4)
Ni	-	1	100
Cu	-	5	6
Zr	-	0.01	0.5
Ba	-	-	0.002
W	-	0.07	0.2
Pt	0.2	-	50
C	(100)	(100)	(64)

Aluminum, which is often considered a *p*-type dopant in diamond, is also present in most spots analyzed and may contribute to the blue coloration. In natural diamond, aluminum is found primarily as an oxide in large

inclusions⁸. Its precise location in the synthetic diamond lattice is not known. However, careful analyses by Collins and Williams²⁰ suggest that the aluminum atom is too large to fit into the crystal lattice and have shown it to be electrically and optically inactive, despite its apparent role as a compensating "getter" for nitrogen. They further suggest that their previous work can be better explained by the presence of boron rather than aluminum as the acceptor. This idea is supported by the theoretical work of Eremets but is still controversial⁵.

Oxygen was a prevalent contaminant in most of the spots examined. The spots were ion milled to sufficient depth to ensure that the detected oxygen was not merely a surface adsorbate. Because of the presence of multiple metal catalysts in the synthesis of the diamond, oxidized metallic inclusions may be the primary source of the oxygen observed. The presence of oxygen on the surface is also discussed in the section on XPS.

Because the hydrogen, oxygen and boron content are of particular interest, another set of SIMS analyses was taken to complement the initial results. The oxygen signal was too great and saturated the detection electronics at the resolution required for boron and hydrogen. The results of the hydrogen and boron analyses are presented in **Table III**. The analysis was performed on 3 "clear" spots and 3 "dark" spots for comparison.

Table III: Approximate Hydrogen and Boron Densities in a GE Synthetic Diamond by SIMS and known RSF's in ppm (or %)

	<i>Area</i>	<i>H</i>	<i>B</i>
Clear	1	300	4
	2	160	13
	3	130	3
Dark	1	(1.9)	30
	2	(0.5)	(0.1)
	3	(1.2)	40

²⁰A. T. Collins and A. W. S. Williams *J. Phys. C: Solid State Phys.* **4**, 1789 (1971)

X-ray Photoelectron Spectroscopy

The XPS studies of the original gem-quality diamond used in the STM studies were unable to detect many of the elements found with SIMS. XPS has a depth resolution of only ~ 100 Å and thus gives information pertaining to the first few surface layers. Oxygen was determined to be the primary surface impurity. The Fermi level position relative to the valence band edge was also investigated. The results of the XPS in the ESCA (electron spectroscopy for chemical analysis) mode are summarized in **Table IV**.

In Experiment A, the diamond was boiled in perchloric acid and stored in ethanol prior to XPS analysis. Surprisingly, the surface did not become charged as was determined by observing the position of the C1s peak. Most natural diamonds show a charging of up to 6 eV²¹. This acid etched surface contained large oxygen peaks in addition to the standard C1s and 2p orbital energies in addition to peaks that correspond perhaps to chlorate, silicon and nitrogen. The activation energy of the boron acceptor levels on other GE diamonds has been reported to be $\sim .35$ eV²⁰ and 0.38 eV²² above the valence band edge and confirmed to be in the same range on other type IIb natural diamonds²³. Determination of the presence of boron is beyond the resolution of the XPS instrument because the acceptor level is too close to the valence band edge. Furthermore, the dopant concentration is presumably less than 1 atomic percent and is thus undetectable by this technique.

In a nitrogen-filled glove box attached to the XPS vacuum system, the diamond surface was subsequently etched by hydrofluoric acid (Experiment B) without exposure to atmosphere. The oxygen peaks were still present, although smaller. The etching removed the chlorate peak but left the chlorine peaks. The C1s peak characteristic of diamond remained, and peaks corresponding to several other impurities became apparent.

In order to determine if the oxygen was a surface contaminant or a deeper impurity, the sample was ion etched ~ 10 Å with Ar⁺ at 4500 eV (Experiment C). All contaminants were reduced to below detectable levels. However, argon was detected, and the location of the C1s peaks also shifted

²¹F. R. McFeely, S. P. Kowalczyk, L. Ley, R. G. Cavell, R. A. Pollak and D. A. Shirley *Phys. Rev. B* **9** (12), 5268 (1974)

²²G. H. Glover *Solid State Electronics* **16**, 973 (1973)

²³A. Halperin and J. Nahum *J. Phys. Chem. Solids* **18** (4), 297 (1961)

and broadened, suggesting that an amorphous or graphitized carbon had been formed during the sputtering²⁴. The transformation of a clean diamond surface to a graphite layer by argon ion etching at appropriate energies has been observed previously²⁵ by Auger electron spectroscopy and is consistent with these results.

In Experiment D (because GE would not permit destructive polishing of the original diamond) the (111) and another face (Experiment E) of the diamond were examined after a sample preparation that did not involve oxygen-containing acids. The samples were sonicated in trichloroethylene and then in ethanol, boiled in HF for 1 hour and resonicated with ethanol before introduction into the XPS vacuum chamber. This preparation resulted in the repeated observation of argon on the (111) face and a large oxygen peak in addition to a small peak indicative of fluorine.

The sample was etched again in HCl (Experiment E) and turned to another face where no argon but some oxygen was detected. Because the faces have slightly different work functions, the location of some of the peaks was slightly shifted relative to those obtained on the (111) face. Fluorine was observed on both faces, but other contaminants were not discernible.

Table IV: X-ray Photoelectron Spectroscopy Results on Boron-doped Diamond

Atomic Percent					
<i>Experiment</i>	<i>Carbon</i>	<i>Oxygen</i>	<i>Nitrogen</i>	<i>Fluorine</i>	<i>Other*</i>
A--HClO ₄	85	12	3	--	--
B--HClO ₄ + HF	91	7	1	--	--
C--B + Ar ⁺	98.5	1.5	--	--	Ar
D--HF (111)	85	10	--	3	Ar, Na, Si, Al
E--HF + HCl (100)	85	9	--	4	Si, Al, Na
*Total may be greater than or less than 100% because of roundoff errors and/or sum of "Other". Atomic percent of elements in "Other" is less than or equal to 1%.					

²⁴F. R. McFeely, S. P. Kowalczyk, L. Ley, R. G. Cavell, R. A. Pollak and D. A. Shirley *Phys. Rev. B* 9 (12), 5268 (1974)

²⁵A. Hoffman, P. J. K. Paterson and S. Prawer *Nucl. Instrum. and Methods in Phys. Res B* 52, 63 (1990)

Scanning Tunneling Microscopy

The microscopic features observed by the STM on the diamond (111) face resemble the macroscopic features observed by other techniques and could be the origins of the larger topography. The atomic detail of the (111) face has a centered, hexagonal symmetry. A variety of trigonal features have been observed by electron microscopy on natural diamond (111) faces²⁶, on (111) surfaces of diamond crystals prepared by the hot-filament CVD method²⁷ and on other GE prepared synthetic diamonds²⁸.

Three distinct features dominate the types of structures observed on this surface. **Figure 3** (BD022B) shows an STM image $\sim 100 \text{ \AA} \times 100 \text{ \AA}$ of what appear to be small, pointed horseshoes cut into the surface. These features will be subsequently referred to as "vees". The image was taken at a sample bias of +4.0 V and set point current of 100 pA. Since the exact crystallographic orientation of the diamond in the STM sample holder cannot be set, the direction of the similarly oriented vees cannot be determined. However, the common orientation of the vees suggests the existence of a preferred etching or growth direction. The features are $\sim 10\text{-}12 \text{ \AA}$ in both length and width. The legs of the vees are $\sim 3 \text{ \AA}$ wide with depths varying from 0.1 \AA to almost 1 \AA , depending on the width. It should be noted that depth of narrow features has little meaning because of the macroscopic geometry of the tip.

Figure 4 shows a higher resolution image about $50 \text{ \AA} \times 50 \text{ \AA}$ of the lower right-hand quarter of the image in **Figure 3** with the same imaging conditions. (BD022C) This area was reproducibly examined for an entire afternoon, but because of an earthquake (4.5 Richter scale with 4.3 aftershocks), the tip "crashed" and the area was not found again.

An observed, hexagonal feature is shown in **Figure 5**. (BDMD006) This feature was observed at +6.0 V and 100 pA. The feature is $\sim 22 \text{ \AA}$ across the long diagonal and $\sim 21 \text{ \AA}$ across the perpendicular axis. The height relative to the background is between 1.2 and 3.0 \AA , depending on the reference area (the background is not uniform and the feature appears to be in a trench). Of particular interest is the apparent straightness of the sides of the hexagon. If the feature were merely contamination, the parallel lines and hexagonal

²⁶Michael Seal *Gems and Gemol.* 10 (10), 309 (1962)

²⁷Keiji Hirabayashi and Noriko Iwasake Kurihara *Jap. J. Appl. Phys.* 29 (10), L1901 (1990)

²⁸A. R. Patel and S. Ramanathan *Physica* 29, 889 (1963)

symmetry would not be expected. This feature was observed only once, and the data were lost (hard disk error) so further analysis could not be performed.

Abrupt changes in surface height, or "steps," were also observed on the surface. An example of one such step is observed in **Figure 6**. (BD019E) The image was taken at 1 nA and -2.5 V. A series of images shows that the step is not an artifact of the tip. The step changes character after a kink and the bump, used as a reference, retains its position and relative size upon changing the magnification scale of the image. This step is most likely one of a number of steps too fine to be observed with electron microscopy (EM) but which build up the sloped terraces and sawlike steps²⁹ that can be observed by EM.

Many less organized areas were also observed on the surface of this and other GE synthetic diamonds. The regular protrusions about 45 Å in diameter that are shown in **Figure 7** (BD021G) were observed at a surprising sample bias of -5.0 V and 100 pA. These conditions suggest the presence of a surface contamination layer, since current at negative sample bias is very rare. The mounds were stable and regular, and they may appear smoothed (rounded) because of the nature of the tip rather than their natural character.

Many images were featureless and often not reproducible from scan to scan. A natural Type IIb diamond and a few less highly doped GE diamonds were examined, but produced few reproducible scans. Tip approaches were difficult on most areas. For feedback currents of either 0.1 nA or 1.0 nA, sufficient current could not be drawn using a sample bias of 4-6 V without crashing the tip into the surface. The relative number of "good" images on the original diamond may be attributed to its higher doping.

Scanning Tunneling Spectroscopy

No current is observed for negative sample bias on any of the IV curves taken on the original *p*-type diamond for both the tungsten and platinum tips used when reproducible spectroscopic curves were obtained. This complete rectification is expected for the limited range of voltage probed by the STM. However, the detailed nature of the curves obtained for the diamond in UHV were much different from those observed in air. Shown in **Figure 8** (BD258A-H) are a series of IV curves taken at 1 nA in UHV (low 10^{-10}

²⁹Hisao Kanda, Toshikazu Ohsawa and Shinobu Yamaoka *J. Crystal Growth* **99**, 1183 (1990)

torr), using a tungsten tip at different tip-sample separations. The absolute separation between tip and sample is not known, but the change in separation between successive scans increases as the feedback bias is increased or decreases as the bias is decreased.

As the separation increases, the rate at which the current rises also increases for each successive scan. The same results were observed on separate occasions at 100 pA feedback with a tungsten tip as shown in **Figure 9** (BDIV217C-J). The vacuum pressure was in the 10^{-9} torr range, but all other factors, including the use of a tungsten tip, were identical. Thus, for one order of magnitude range of current and a ± 7 V range of sample biases, the nature of the IV spectroscopy appears similar and has been observed on numerous occasions.

However, current-voltage data taken in air have a completely different character. **Figures 10 and 11** (BD137 and BD136) show a series of IV curves at an initial feedback current set to 100 pA. The data were taken in air with a platinum tip and electrical contact to the stub with Ag paste. No current is observed below a very consistent threshold at +3.8 V sample bias for each separation. **Figure 10** is the series from 4-6 V, while **Figure 11** shows 7-8 V range. Other types of IV curves such as those shown in **Figures 12 and 13** are also obtained at atmospheric conditions. For all of the IV data collected in air, the scans were entirely reproducible at each site but variable between sites.

Ohmic contacts can be made to the surface with colloidal graphite or silver paint as suggested by Moazed *et al.*³⁰ Ohmic contact was verified by a two spot contact measurement. Indium contacts were shown to have a resistance less than those used in the STM imaging experiments.

DISCUSSION

The following discussion is divided into three sections. First, the oxygen and boron content as determined by XPS and SIMS is discussed since those elements directly affect the electric properties of the diamond. Next, the surface features observed by STM are discussed. Finally, the character of the IV spectroscopy is related to the surface oxygen and explained in terms of Schottky analysis and tunneling theory.

³⁰K. L. Moazed, J. R. Zeidler and M. J. Taylor *J. Appl. Phys.* 68 (5), 2246 (1990)

Contaminants and Dopants in Semiconducting Diamond

Oxygen was the major contaminant observed by XPS analyses of the diamond surface. Although the oxygen was removed after the Ar⁺ sputter in Experiment C, oxygen was detected for the second set of XPS experiments on both faces examined. This result is surprising because the diamond was not exposed to any oxygen-containing acids. In fact, oxygen persisted on both faces even after boiling in HF and rinsing with HCl in a controlled nitrogen environment. Since oxygen was observed in large quantities on the as-grown diamond examined by SIMS, the lack of oxygen after sputtering may be indicative only of the heterogeneity of the sample rather than an actual cleaning. It should be noted that oxygen was not observed on the one "dark" spot.

Consequently, oxygen could be a tenacious surface contaminant that was not removed, but was simply not present in quantities sufficient for detection on the one spot that was examined with XPS after the sputter. Pate³¹ has observed that oxygen is the primary surface contaminant on the as-grown diamond surface, even after sample heating to greater than 500°C. The diamond surface is highly inert unless extreme oxidation conditions are used, but any resident oxide is very difficult to remove.

The oxygen peak observed in the XPS peaks obscured the direct identification of the Fermi energy. As a result, the Fermi energy was estimated by measuring the shift of the C1s peak relative to the valence band edge compared to the data presented by Pate, and is assigned ~1eV above the valence band edge. This assignment is tentative as it is difficult to measure the center of the C1s peak. It was hoped that a definitive E_f could be determined. However, the Fermi energy can be very different on differently prepared surfaces. For example, Pate observes the Fermi level to be between 0.2 eV and 0.6 eV on a polished 1x1 surface and ~1.4 eV on a reconstructed 2x2/2x1 surface.

The SIMS analysis, although unable to give chemical bonding environment information, proved to be an extremely useful technique for determining dopant density near the surface, as it has a much greater sensitivity than the XPS for detecting quantities of elements in quantities less

³¹Brad. B. Pate *Surface Science* 165, 83 (1986)

than 1 atomic percent. As shown in Table III, hydrogen is clearly present in the diamond in large quantities (from 0.01 to almost 2.0%). The distribution of metal and other (K, Na, Ca, Ba, Si, and Cl) impurities is heterogeneous. Presumably, the wide variety of observed metal impurities have some function in the diamond growth process or diffuse from the containment cylinder of the diamond press.

The boron component ranged from 3 to 1500 ppm (0.15%) in various sites on the diamond surface. From the diamond matrix density of 10^{23} cm^{-3} , the dopant level thus ranges from 3×10^{17} to $1 \times 10^{20} \text{ cm}^{-3}$ in this sample. The following simple calculation provides an order of magnitude estimate of the number of intrinsic carriers per unit volume in a pure diamond at room temperature. Since the density of free holes, ρ , is

$$\rho = 2 \left(\frac{2\pi m_p kT}{h^2} \right)^{\frac{3}{2}} \exp \left(\frac{-(E_f - E_v)}{kT} \right), \quad (1)$$

where h is Planck's constant, k is Boltzman's constant, m_p is the effective hole mass, E_f is the Fermi energy, E_v is the energy at the top of the valence band, and assuming the location of the Fermi energy to be $\frac{E_g}{2}$, the relationship $n_i = \sqrt{np}$ can be used to calculate n_i , where n is the density of free electrons and n_i is the number of intrinsic carriers². At room temperature, the intrinsic carrier density per unit volume is $\sim 10^{-60}$ as opposed to $\sim 10^6$ [Ref 11], 10^{13} and 10^{10} for gallium arsenide, germanium and silicon, respectively. Nearly all natural diamonds have carrier densities much greater than the ideal intrinsic value because of inevitable impurities. The measured range of doping should provide sufficient carriers to exceed the intrinsic carrier concentration in diamond, despite boron's deep acceptor level at $\sim 0.38 \text{ eV}$.

Imaging Diamond by Tunneling Electrons

Although the sample was more highly doped than any naturally occurring diamond, it is still not very conductive. For examination by the STM, a highly conducting sample is necessary so that charge does not build up on the sample and considerably increase the barrier to tunneling. As long as

the resistance in the sample is less than the resistance of the tunneling gap (typically $\sim 4 \times 10^{10} \Omega$ in these experiments), imaging should be possible.

The diamond sample was heterogeneous with regard to the conductivity observed by the STM on the surface. Because some areas were practically insulating, sufficient current could not be obtained without ramming the tip into the surface. Numerous areas were scanned where no stable tunneling was observed. Other sites had stable tunneling and reproducible images. By using a higher sample bias (4-5 V) than traditionally used in STM, images could be obtained. Occasionally at low biases, inadequate current was obtained, even after "crashing" the tip.

As suggested by the IV curves, no states were available in which to tunnel until the bias was over ~ 3.80 V. The tip, unable to draw a current, would move toward the surface until contact was made and the feedback current was obtained. Although tunneling was not verified as the only current producing mechanism (field emission is not likely to contribute significantly since the barrier height is so large), the response of the feedback circuit to small changes in topography indicates that when a stable current and reproducible scans were obtained, the major contribution to the current was tunneling. Furthermore, the exponential character of the IV curves suggests that tunneling is the major current contribution.

Under good tunneling conditions, steps, hexagonal and veelike features were observed on the surface. Analysis of the step shown in **Figure 6** shows a height of $\sim 2 \text{ \AA}$ and is assumed to be a single step, because the interplanar spacing on the (111) surface is 2.1 \AA ¹⁸. Dissolution (etching) of flat faces often occurs layer by layer to produce microlamination and typically starts at the corners of a macroscopic diamond or at previously started discontinuities. Although interference of tip geometry is minimized when imaging flat planes, the tip morphology is still apparent on the step. The small indent in the step is probably a feature on the tip that is imaged as it passes over the sharp step edge.

Although few examples of hexagonal features have been observed on a larger scale than that of the STM images, most features are trigonal. The image in **Figure 5** could be a growth facet that perhaps grows to become a larger trigonal feature by disproportionate growth rates along different directions.

The vees are definitely the most interesting feature discovered on the diamond surface. A similar orientation is nearly always observed for similar features on a macroscopic scale⁸. Rows of trigonal features are often etched along glide lines or near defects. Dislocations generated by inclusions deeper in the diamond but emanating to the surface tend to make a close-packed pattern of etch triangles. It would be gratifying to say that the boron component has produced the inclusions or local defects, but the evidence suggests that a number of other metal inclusions could be responsible. Interestingly, the macroscopic trigonal features are always of a very regular size for a given region as observed here. Presumably, the etchant attacks areas on the surface and reacts with a similar rate. The vees could grow together to become etch "trigons" (inverted pyramids), but the number density would, of course, decrease.

The effect of the tip geometry on imaging surfaces is always a concern³². The possibility that any of the presented vee features are a result of multiple tips or a result of a rough surface imaging a smooth tip were discounted for the following reasons: 1) The scans were reproducible in both the forward and reverse directions; 2) the scans were reproducible for multiple images at multiple image sizes; 3) for inverse imaging (surface imaging of the tip), the vees would have to be present on the tip, lying flat, and would necessarily be imaged by a very sharp protrusion on the surface. A large, flat area such as one necessary to contain a vee of the observed size on the tip would tend to produce smoothed images of all areas of the scanned surface. This smoothing was not observed; 4) the observed vees have thin legs, requiring a sharp imaging probe. The diamond surface is not likely to maintain such features, especially after a boiling in acid, and finally 5) this trigonally shaped feature is expected on the diamond (111) face and not on an etched tungsten tip.

The observed surface morphology seems to mimic the macroscopic morphology. It is reasonable to assert that the small vees are the beginnings of etch pits, perhaps enhanced by impurities and/or defects in the diamond structure. A single step would be a logical member of a larger number of steps comprising the sloped surfaces observed in EM. Hexagonal and trigonally

³²O. Nishikawa, M. Tomitori and F. Iwawaki *Mat. Sci. and Engrng.* B 8, 81 (1991)

symmetric features are common on the diamond surface and could originate from features such as these.

Current-Voltage Spectroscopy

Surface Potential Screening and Reduced Band Bending

Although other techniques can measure IV's at a given electrode separation, only the STM allows for a systematic examination of a variety of metal-diamond separations, thus insuring the same interface (gap) properties for each successive measurement. The magnitude of the current depends on two factors: 1) the tunnel transmission probability, which in this discussion is assumed to be dependent primarily on the tip-sample separation and be bias independent and 2) the thermionic emission that is proportional to the term $[\exp(-qV_d/kT)-1]$, where V_d is the surface voltage potential in the semiconductor which can be measured as the difference in potential of the conduction band edge at the surface and the bulk, q is the charge, k is Boltzman's constant and T is the temperature. With the STM flexibility, the relative contribution or lack of effect of distance and band bending can be compared or at least noted.

The characterization of the electrical properties of this diamond are based primarily on the IV curves measured and on the observation that sufficient current to image with the STM occurs at only positive sample bias. The boron content analysis is consistent with these results. Unfortunately, Hall measurements could not be taken of the diamond because of its irregular geometry. Although the surface resistance can be measured with an ohmmeter, the value is meaningless since it varies from measurement to measurement and depends primarily on surface contamination. The measured surface resistance was always below $500\ \Omega$ both across the (111) face and across the diamond. Since surface conduction may dominate, this value is not a measure of bulk resistance.

The exponential character of the IV curves can be examined by a simple plot of $\ln(I)$ *versus* sample voltage as shown in **Figure 14** for the data of **Figure 8**. An ideality factor or "n factor" (n), for a Schottky barrier can be

calculated as explained by Card and Rhoderick³³. For sample biases greater than $3kT/q$ ($=0.077$ V), n reduces to

$$\frac{1}{n} = \frac{kT}{q} \times \frac{d \ln(I)}{dV}. \quad (2)$$

The calculated n values from the data of **Figure 14** range from 6 to 12 for the data taken from a lower set point voltage (closer to surface) to higher voltage (farther from surface).

The IV curves cannot be explained by an ideal Schottky barrier, which is defined for intimate contact for which $n=1$. The observed ratio of current change per volt is less than would be expected for the voltages applied when operating at physical separations conducive to tunneling. This result implies that the semiconductor is experiencing less applied voltage than would be expected for the bias applied to the tip. Although less bias would be the result of a very large tip-sample separation, the separation necessary would not provide the required tunnel current, and the feedback circuit would compensate accordingly. However, a mechanism for reducing the field at the semiconductor surface can be produced if the potential were screened by surface states on the semiconductor surface or by localized traps in the gap..

On the basis of the calculations of Cowley and Sze³⁴, Card and Rhoderick extend their analysis of the ideality factor to include the effect of surface states on the IV characteristics for a metal-insulator-semiconductor

junction. For a given tip-sample separation (s), depletion width ($W = \sqrt{\frac{2\epsilon_s \epsilon_0 V_d}{qN_D}}$), dopant concentration (N_D), semiconductor dielectric constant (ϵ_s), density of surface states (D_{sc}) and the vacuum permittivity ($\epsilon_0 = 8.854 \times 10^{-12}$ F/cm), then the ideality factor can be expressed as

$$n = 1 + \frac{s}{\epsilon_0} \left(\frac{\epsilon_s}{W} + qD_{sc} \right). \quad (3)$$

Using average values for V_d , doping levels from the SIMS analysis (10^{17} - 10^{20} cm⁻³), and diamond's dielectric constant, the surface state density was

³³H. C. Card and E. H. Rhoderick *J. Phys. D: Appl. Phys.* 4, 1589 (1971)

³⁴A. M. Cowley and S. M. Sze *J. Appl. Phys.* 36 (10), 3212 (1965)

calculated to determine if reasonable, physical values emerged. The results are shown in **Figure 15**. The surface charge density calculated does fall within a reasonable range of values (10^{13} - 10^{14} V⁻¹cm⁻²) and appears to depend primarily on the separation (s) and the permittivity of the sample, which in the case of diamond is very low. As is apparent from the graph, the depletion width has much less effect on the calculated surface charge density than does the tip-sample separation. However, since the depletion width depends on the tip-sample separation and doping level, both of which are not known in the STM experiment, the graph was plotted for a large range of values. Interestingly, for the range of n factors observed, the resultant D_{sc} value is reasonable.

On a synthetic diamond, Geis *et al.*⁶ calculated an ideality factor of 2 and a barrier height of 1.3V from I-V measurements at 580°C, where most of the acceptors are ionized. They suggest that deep traps in the diamond are responsible for hysteresis in IV curves with tungsten contacts. No hysteresis was observed in our spectroscopic studies.

The assumptions used in this calculation are that the tunneling probability is constant over the range of biases used for each separation, s , and that the contribution to the current of minority carriers (electrons) to the forward bias current is minimal. The latter assumption is likely assured by the diamond's properties. Because the first assumption is not entirely valid in this system, the slight curvature in the $\ln(I)$ *versus* V plots is not unexpected. The band bending in the semiconductor *does* have a nonlinear voltage and distance dependence that becomes greater at larger separations³⁵. This band bending, V_d , can be expressed as

$$V_d = V_{d0} \{ [(c+1)^2 - V/V_{d0}]^{1/2} - c \}^2, \quad (4)$$

where c is defined as $(\epsilon_s s/W)$, and W_0 and V_{d0} are the depletion width and surface potential as described before but in the limit of zero separation. As observed in **Figure 14**, the curvature increases at larger s values (from left to right), consistent with tunneling theory for finite separation.

³⁵L. D. Bell, W. J. Kaiser, M. H. Hecht and F. J. Grunthaner *Appl. Phys. Lett.* **52** (4), 278 (1988)

Pinning of the Fermi Level

The IV curves for the diamond surface in air (**Figures 10 to 13**) show no such exponential dependence but display a strong threshold voltage and a nearly linear increase in current afterwards. Because the diamond was exposed to the highly oxidizing conditions of hot perchloric acid before spectroscopic analysis, the presence of an oxide on the surface is likely despite the stability of the diamond surface to oxidation at ambient conditions. The XPS results verify the presence of tenacious oxygen after such a treatment. Although the oxidation of the surface may not be complete, the small area probed by the STM tip may be sufficiently oxidized to change the electrical properties.

The threshold voltage seen in the IV curves of **Figures 10 and 11** does not change upon changing the bias set point of the tip (thus changing the tip-sample separation for a constant current set point) suggesting that the Fermi level is pinned and that the band bending is small. The minimal band bending is consistent with the lack of exponential dependence of current on the voltage as would be expected for thermionic emission of a Schottky barrier. Instead, the threshold voltage is consistently measured at 3.8 V positive sample bias. With diamond's 5.5 eV band gap, the Fermi level is thus observed to be pinned at 1.7 eV above the valence band.

Studies using other techniques on Type IIb diamonds have suggested the location of the pinned Fermi level. Glover²² has made Schottky contacts on a GE boron-doped diamond by sputtering gold on the surface after cleaning the diamond by boiling in HNO₃ and H₂SO₄. A zero-bias Fermi level is measured to be 1.77 eV above the valence band maximum (the reference point for all future discussions), which agrees with the one-third band gap rule of Mead and Spitzer³⁶. Pate³¹ discusses theoretical diamond surface states arising from the clean, unreconstructed (111) face having dangling bonds that pin the Fermi level at 1.7 eV. However, his XPS measurements reveal Fermi levels from 0.2 eV to 1 eV, which he suggests is a result of hydrogen termination of the surface. The similarity between Glover's diamond, preparation and results with those in this STM study suggests the same Fermi level pinning.

³⁶C. A. Mead and W. G. Spitzer *Phys. Rev.* **134**, A713 (1964)

It should be noted that the spectroscopic results in air are not reproducible over different sites on the surface. As shown in **Figure 12**, the IV's are not exponential and have a constant threshold voltage which is greater than +4.0 V. The two curves taken at a feedback bias less than +4.0 V (two farthest left) are different and are presumably represent tip contact with the surface. The variability in these scans may be a result of any of the metal or other impurities near the surface at the tip site.

The effect of oxygen on the diamond surface is of great interest, especially in the attempt to preserve ohmic metal-diamond contacts. Mori *et al.*³⁷ have demonstrated that an oxide layer changes previously ohmic contacts to Schottky-like contacts and that the Schottky dependence on the metal electronegativity disappears. They suggest that the oxide pins the Fermi level, thus changing the electrical properties of the metal-diamond interface.

The importance of oxygen on diamond semiconductor properties at high temperatures is clear and may be better understood by room temperature analyses such as these. The highest operating temperature for transistors and diodes yet achieved⁶ has been performed on a GE Boron-doped synthetic diamond at 700°C. Above that temperature, the diamond surface is attacked by oxygen, and presumably the desired properties disappear. Above 800°C in an argon environment, the surface and diode performance degrades. Only diodes formed with silicon carbide come close to this high operating temperature with a maximum operating temperature of ~600°C.

For both types of IV's observed on the diamond surface, the current is rectified for essentially all negative sample biases. The only negative current observed is shown in **Figure 13**. Again, the threshold voltage is over 4.0 V, suggesting that surface conduction may be responsible both for the negative current and screening the potential bias.

For the relatively unpinning surface observed in vacuum, rectification is expected because although the reverse bias is increased, the tip Fermi level never catches up to the bending band edges. For a pinned Fermi level, one could expect filled states in the sample valence band to be observed at negative sample biases in the diamond over 1.8 eV. However, the complete

³⁷Yusuke Mori, H. Kwarada and A. Hiraki *Appl. Phys. Lett.* 58 (9), 940 (1990)

rectification is *not* surprising, given basic tunneling theory, especially for the diamond whose band gap is greater than any semiconductor ever studied by the STM.

The probability that an electron will tunnel on the basis of the WKB approximation for a smoothly varying potential, when reduced to a simple square barrier, can be expressed by the barrier-penetration factor D^{38} ,

$$D = \exp(-\alpha\sqrt{\phi - eV} \text{ s}), \quad (5)$$

where $\alpha \sim 1\text{V}^{-1/2}\text{\AA}^{-1}$, and ϕ is the average work function of the tip and sample. For positive sample bias, the electrons at or near the Fermi energy of the tip tunnel to unfilled states in the sample as shown in the top of **Figure 16**. As the bias is increased positively, these same electron levels close to the Fermi energy probe higher energy states on the sample. The electrons with energies much less than the Fermi energy will contribute to the current, but with an intensity exponentially less than the electrons having higher energies.

When the sample is biased negatively, the potential energy of the electrons in the sample are raised relative to those of the tip, and electrons will tunnel from filled states near the Fermi energy of the sample to the tip. As this bias is increased (**Figure 16**, bottom half), the tunneling probability of the lower lying electrons decreases as they experience a tunnel barrier greater than the higher energy states. Their contribution to the tunnel current is exponentially less than those near the Fermi energy.

Filled states have been observed by the STM on small band gap semiconductors such as silicon³⁹ and gallium arsenide⁴⁰. One explanation is that these surface states may extend into the gap, and although the height of the barrier (energy) seen by the lower energy filled state electrons has increased, the barrier width decreases. Alternately, and more consistently, the rectification is a result of the magnitude of diamond's band gap relative to these other semiconductors. The probability to tunneling through the barrier presented by a 5.5 eV gap is very low.

³⁸C. B. Duke *Tunneling in Solids* (Academic Press: New York), 61 (1969)

³⁹R. Wolkow and Ph. Avouris *Phys. Rev. Lett.* 60 (11), 1049 (1988)

⁴⁰P. Mårtensson and R. M. Feenstra *Phys. Rev. B* 39 (11), 7744 (1989)

CONCLUSION

In order to understand the difficulties in imaging and interpreting STM images of diamond, the nature of the surface properties must be considered. The large band gap of the diamond insures that there are few carriers in the conduction band at room temperature. Problems of surface charging were not encountered in the XPS investigations on areas larger than 300 μm in diameter; however, the areas probed with the STM are only a few hundreds of \AA on a side. Because of the heterogeneity of the diamond, localized areas could have insulating properties as indicated by the inability to draw significant current on numerous occasions. Although stable tunneling could never be achieved on the natural and lesser-quality, synthetic Type IIb diamonds, regions of stable tunneling were encountered on the highly doped synthetic diamond surface.

The features observed on the surface by scanning tunneling microscopy mimic those observed on natural diamond surfaces by electron microscopy. Atomic resolution with the STM was not seen; however, the necessity to image at higher biases than typically used in STM experiments can account for this fact. At such high biases, the tip is probably at a distance from the surface where the variations in local density of states is much less than at smaller tip-sample separations.

Current-voltage spectroscopy not only reveals the electronic nature of the diamond surface, but also helps to determine the appropriate conditions for successful STM imaging operation. Clearly, since no current was obtained below +3.8 eV in air or at any negative sample bias, the voltage set point should be maintained above that value. While this result is true on the original diamond, it is probably not representative of other diamonds.

The presence of persistent oxygen on the surface is thought to account for some of the charge screening observed in the vacuum spectroscopy. The unpinning character is reproducible, and the density of surface charges has been shown to produce "ideality factors" measured from the IV curves. The diamond spectroscopy observed at atmospheric conditions does not exhibit an exponential dependence of the current on the voltage. The threshold voltage observed in air is consistent with pinning the Fermi level at ~ 1.8 eV, but is not reliably observed. This barrier height of 1.8 eV is in agreement with the

one-third band gap rule of Mead and Spitzer³⁶. The original oxide layer observed in vacuum by XPS with additional adsorbate states acquired from air contamination provide sufficient surface charge density to pin the Fermi level. Surface conduction and metal impurities close to the surface may have a considerable effect on the heterogeneous nature of the localized electrical properties.

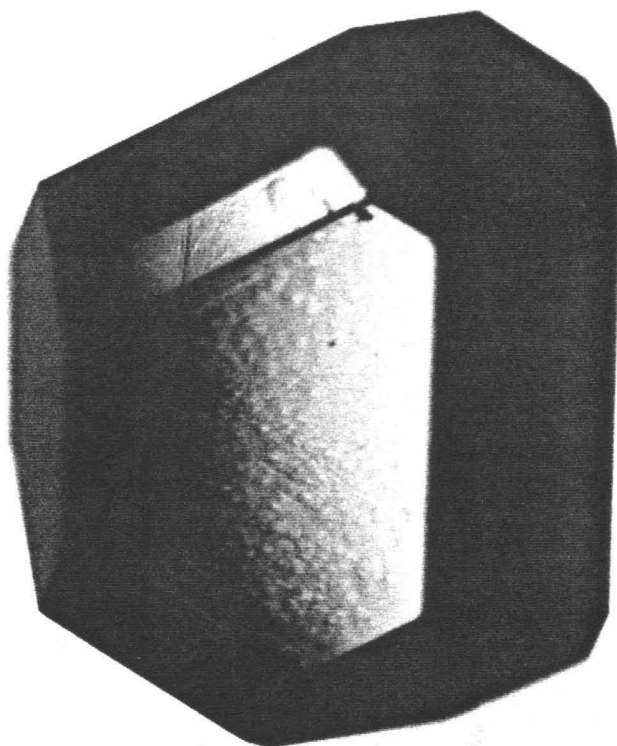


Figure 1: Photograph of the boron-doped, synthetic, gem-quality diamond used for these investigations. The diamond measures $\sim .5 \text{ cm} \times .5 \text{ cm} \times .4 \text{ cm}$ and is a deep, navy blue color when held to the light and otherwise appears nearly black. The trigonal face was examined by scanning tunneling microscopy and spectroscopy.

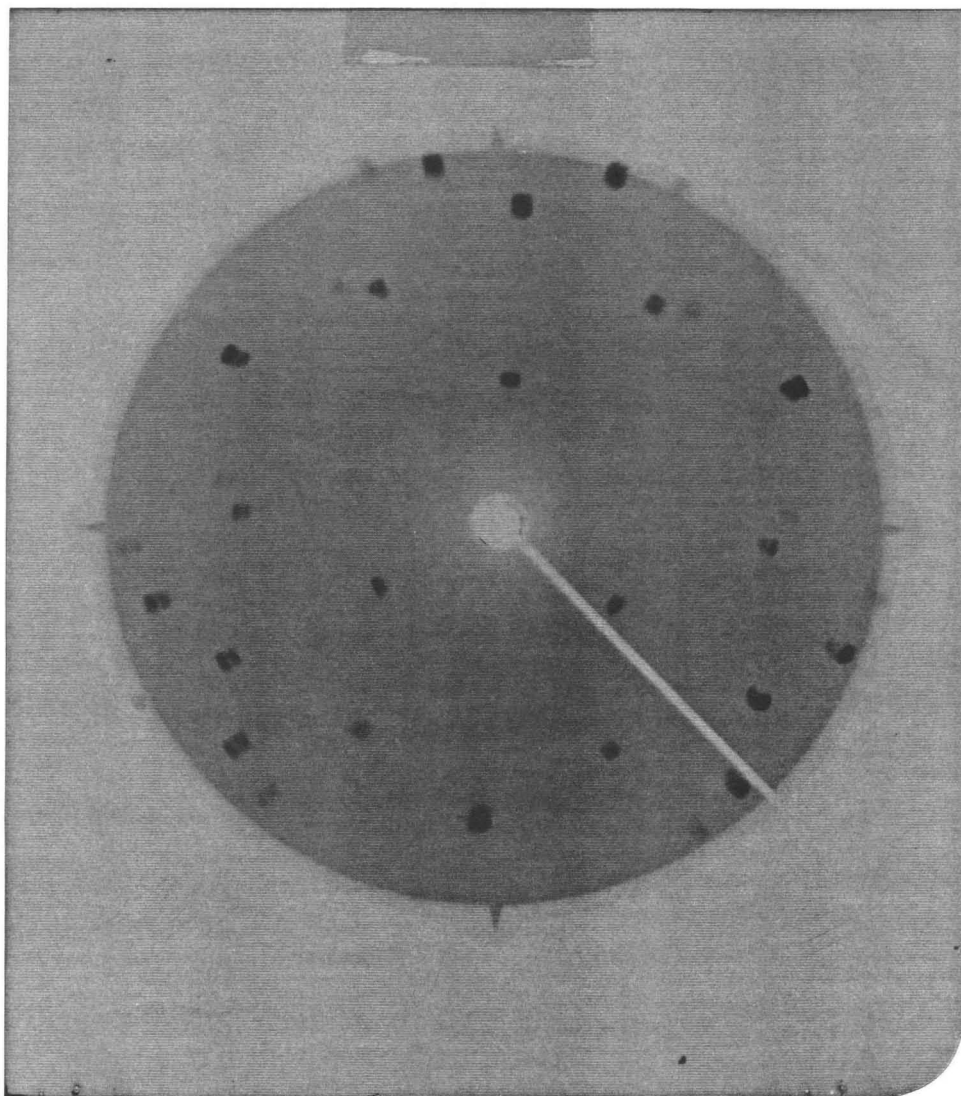
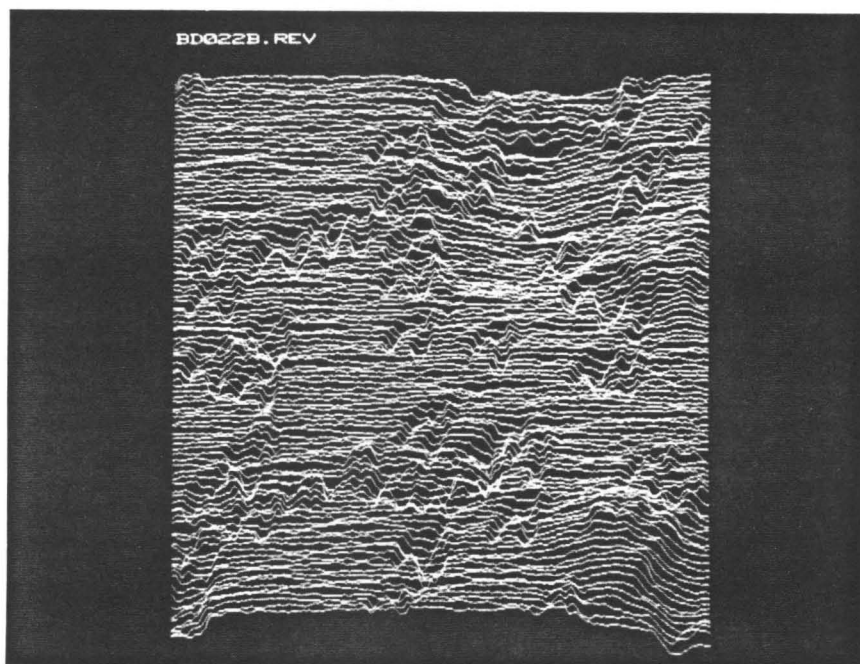


Figure 2: Laue diffraction pattern showing the trigonal symmetry of the $[111]$ direction through the (111) face.

a)



b)

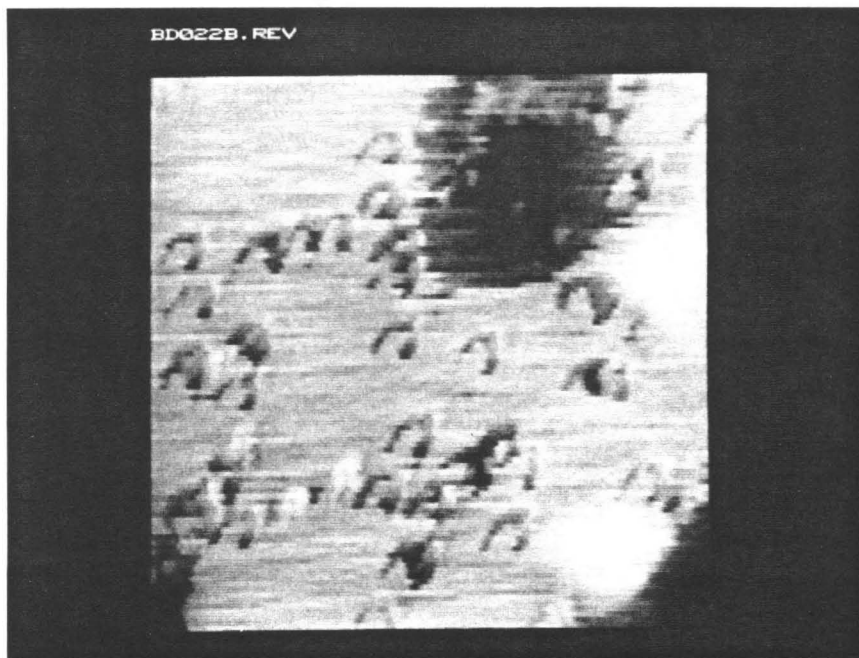
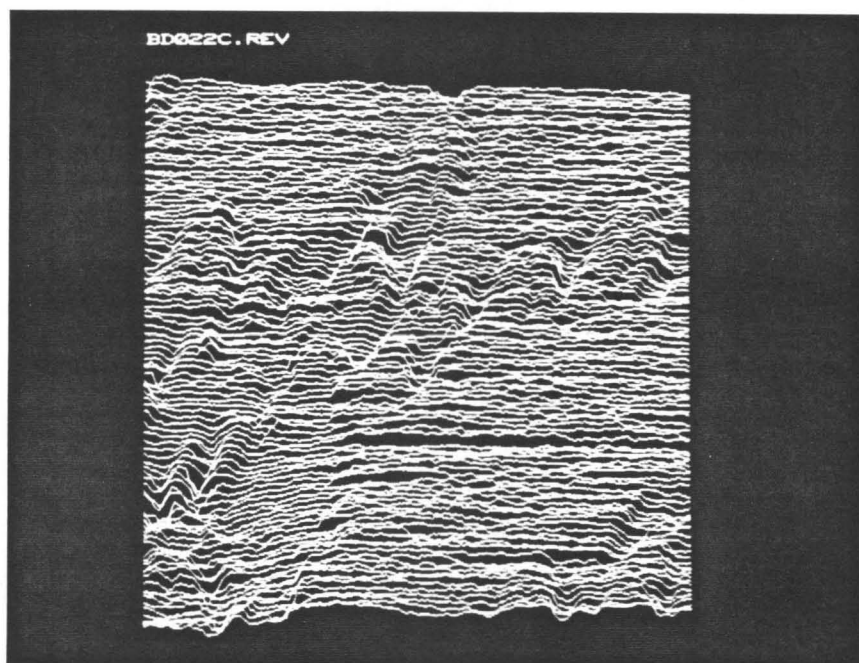


Figure 3: (BD022B) STM constant current image presented as a) line scan and b) gray scale of a 100 \AA by 100 \AA area showing the vees discussed in the text. The image was taken at $+4.0 \text{ V}$ sample bias and 100 pA .

a)



b)

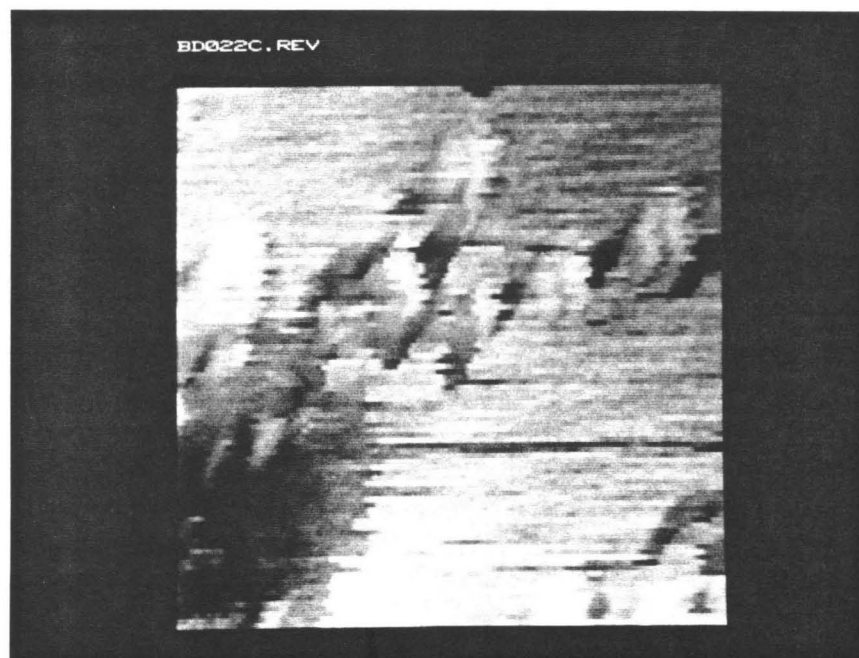


Figure 4: (BD022C) Higher resolution image $50 \text{ \AA} \times 50 \text{ \AA}$ presented as a) line scan and b) gray scale of the right-lower quarter of the image in **Figure 3** taken with the same STM parameters. Notice that the features of the previous figure are reproduced.

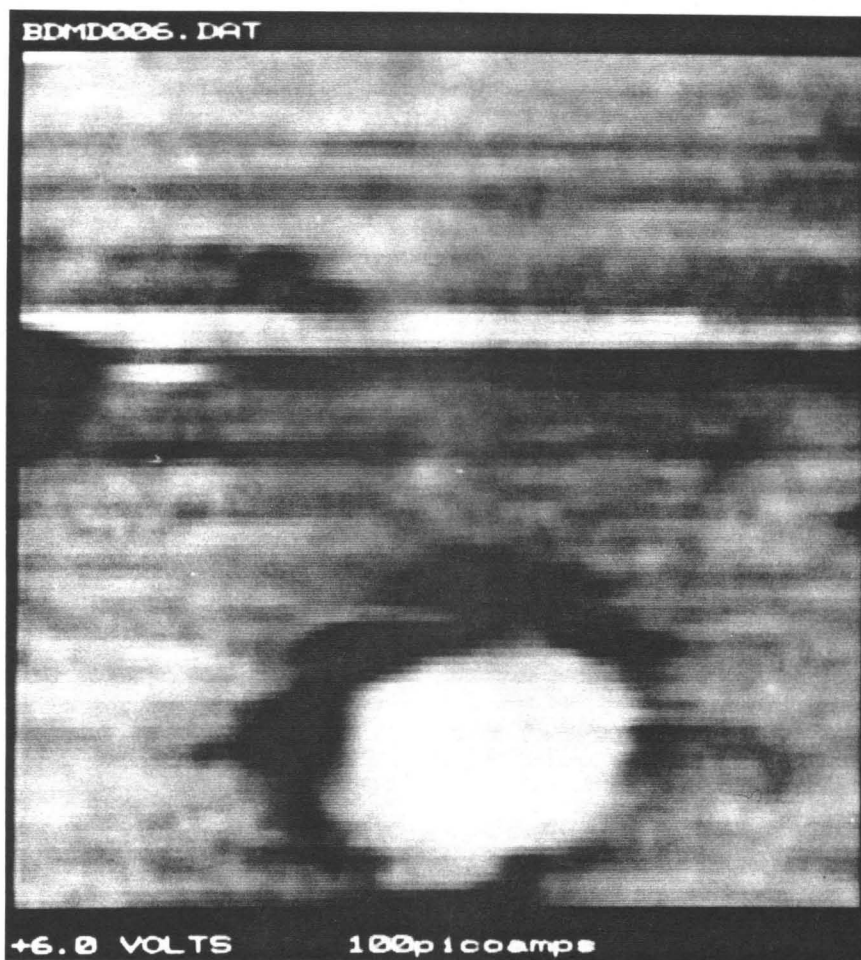
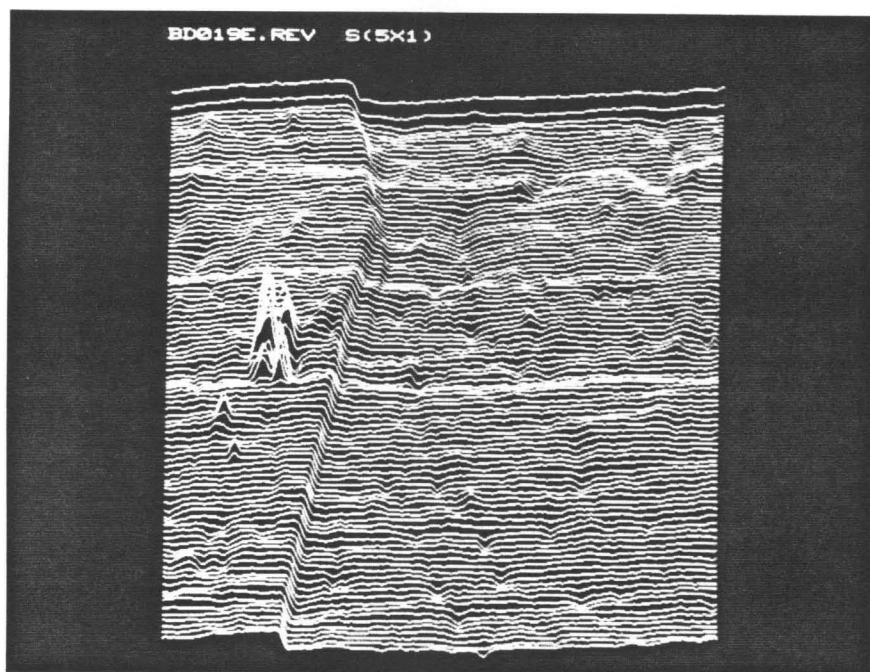


Figure 5: (BD006) STM constant current image presented in gray scale showing a hexagonal feature observed on the surface. The image is $915 \text{ \AA} \times 915 \text{ \AA}$ and taken at $+6.0 \text{ V}$ sample bias and 100 pA .

a)



b)

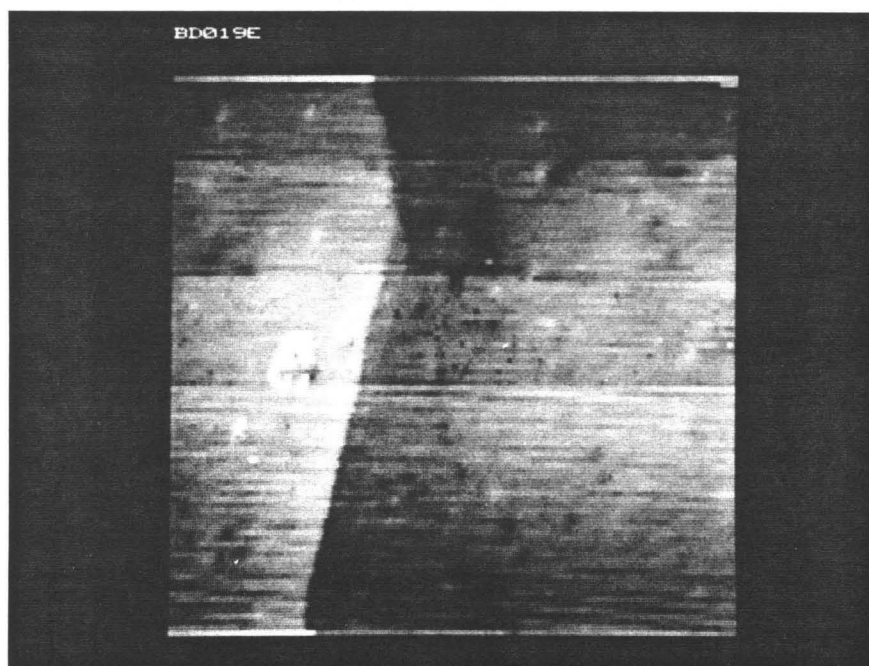


Figure 6: (BD019E) STM constant current image shown in a) line scan and b) gray scale of a $100 \text{ \AA} \times 100 \text{ \AA}$ area of the diamond surface taken at 2.0 V and 100 pA. The step height corresponds to a single layer step.

a)



b)

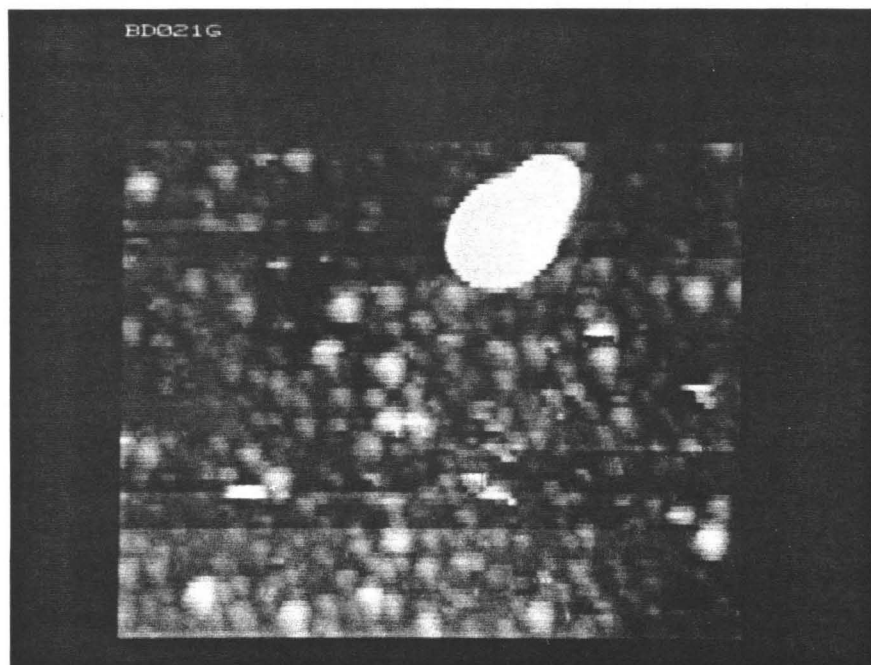


Figure 7: (BD021G) A large $915 \text{ \AA} \times 915 \text{ \AA}$ area STM constant current image presented in a) line scan and b) gray scale. The image was taken at -5.0V and 100 pA . The observed mounds are $\sim 45 \text{ \AA}$ in diameter.

IV Curves of Boron-doped Diamond with a Tungsten Tip at 1nA Feedback Current

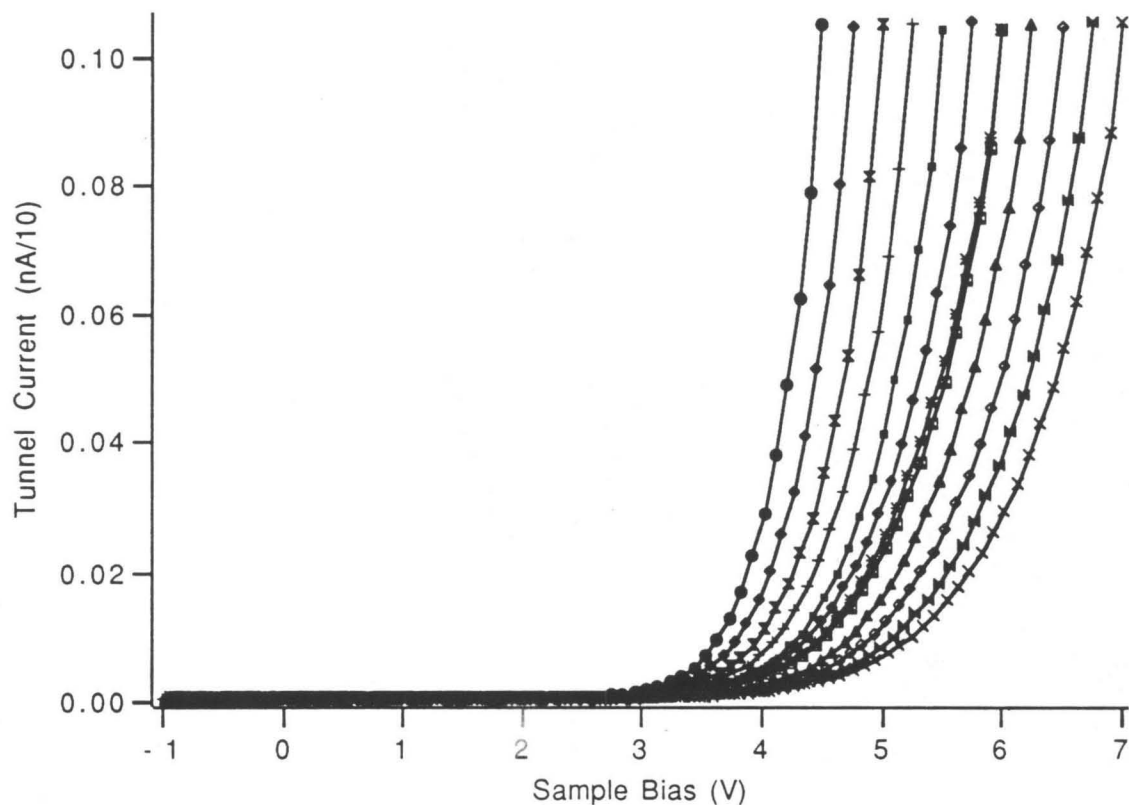


Figure 8: (BD258A-M) A series of IV curves at different tip-sample separation on boron-doped diamond in 10^{-10} torr. The feedback current was 1nA and original set point biases were 7.00, 6.75, 6.50, 6.25, 6.00, 5.75, 5.50, 5.25, 5.00, 4.75 and 4.50 V, respectively, from right to left curves (from farther from the surface to closer). The tip was tungsten, and electrical contact was made to the stub and the top of the diamond with indium.

IV Curves on Boron-doped Diamond at a Feedback Current of 100pA

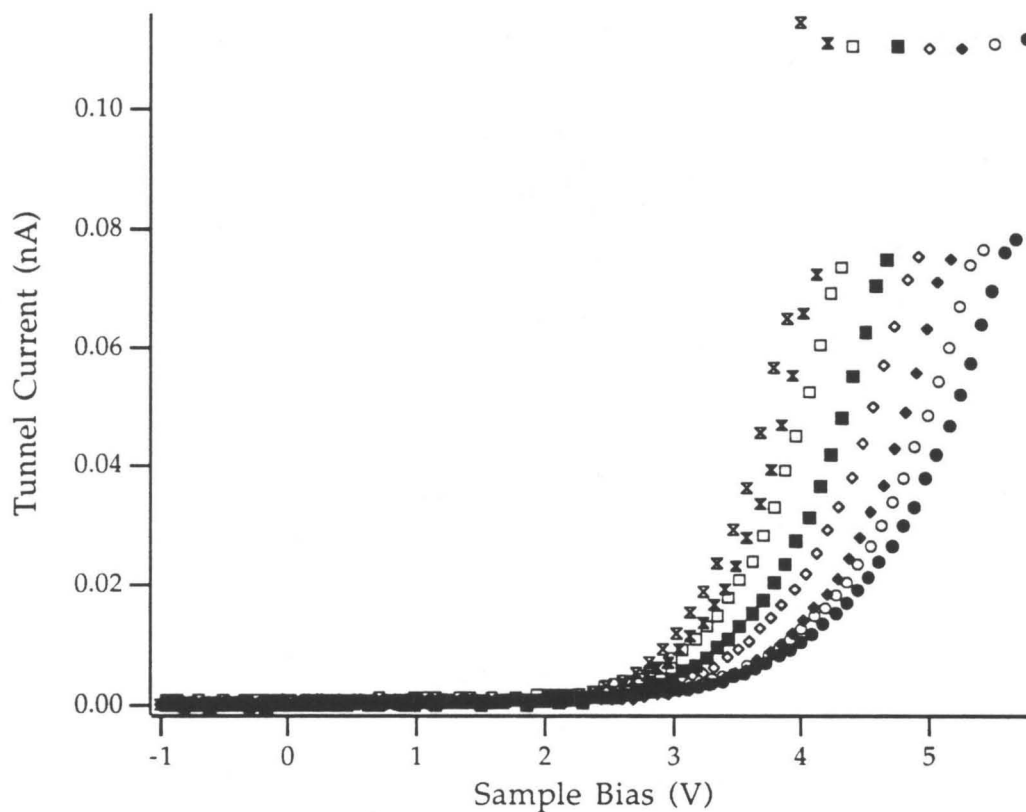


Figure 9: (BDIV217C-J) Series of IV curves taken at different, tip-sample separations. The data were taken at 10^{-9} torr with indium contact and a tungsten tip. These IV's were taken at original sample biases of 4.0, 4.2, 4.75, 5.0, 5.25, 5.5, and 5.75 V.

Current-Voltage Curves for Boron-doped Diamond With a Feedback Current of 100 pA

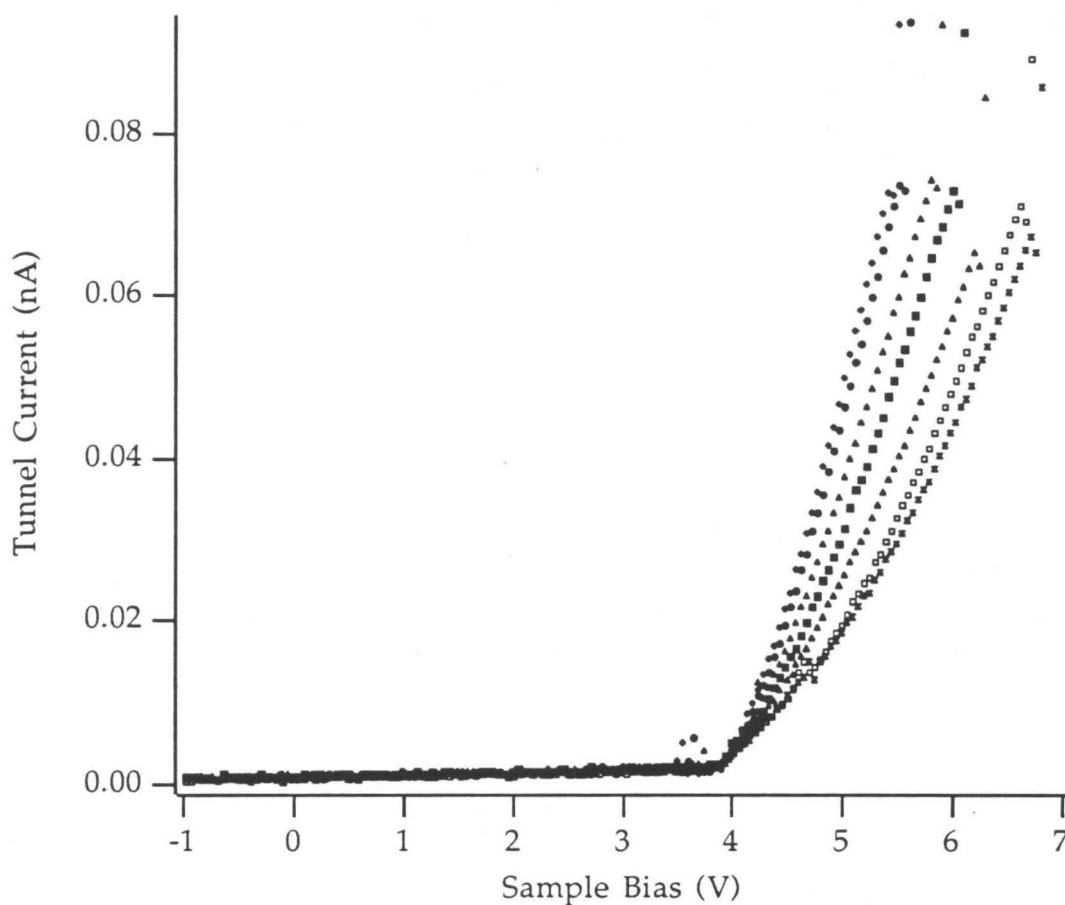


Figure 10: (BDIV136I-N) A series of IV curves at different, tip-sample separations established by different sample bias set points. IV's were taken with a cut platinum tip at atmospheric pressure in air. Electrical contact was made to the stub with Ag print. Original feedback voltages are, from left to right, 5.5, 5.6, 5.9, 6.1, 6.3, 6.7, and 6.8 V.

IV Curves on boron-doped Diamond at a Feedback Current of 100 pA

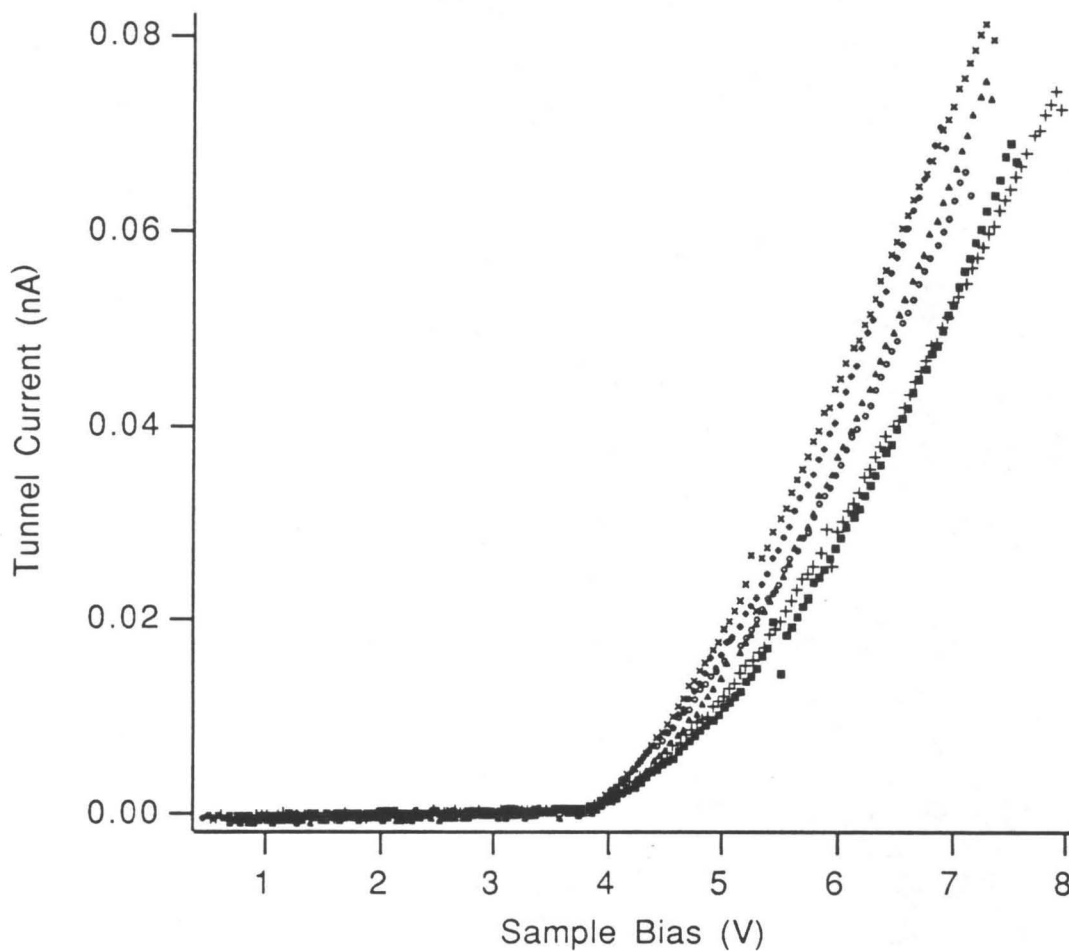


Figure 11: (BDIV137A-G) A series of IV's taken at different, tip-sample separations established by a feedback of 100 pA and original sample bias feedback voltages were 7.0, 7.2, 7.4, 7.6, 7.8, and 8.0 V. The data were taken in air with a cut platinum tip. Electrical contact was made with the sample stub by Ag print.

IV Curves on Boron-Doped Diamond Taken in Air at 1 nA Feedback Current

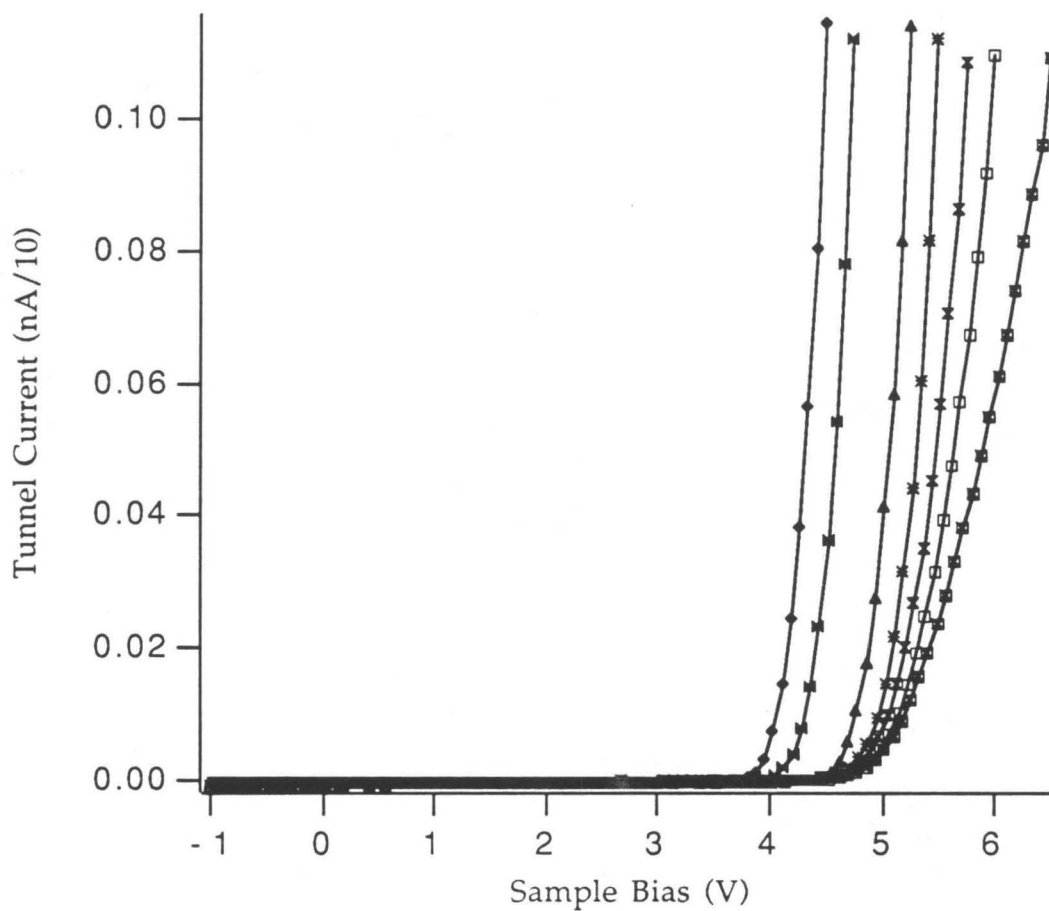


Figure 12: (BIV006A-H) Series of IV curves at different tip-sample separation for feedback to 1 nA. The data was taken in air with a tungsten tip after the diamond had been boiled in perchloric acid and rinsed with ethanol. Electrical contact was made with colloidal graphite.

**Current-Voltage Curves of a Boron-doped Diamond
Taken in Air With a Tungsten Tip at 1 nA Feedback Current**

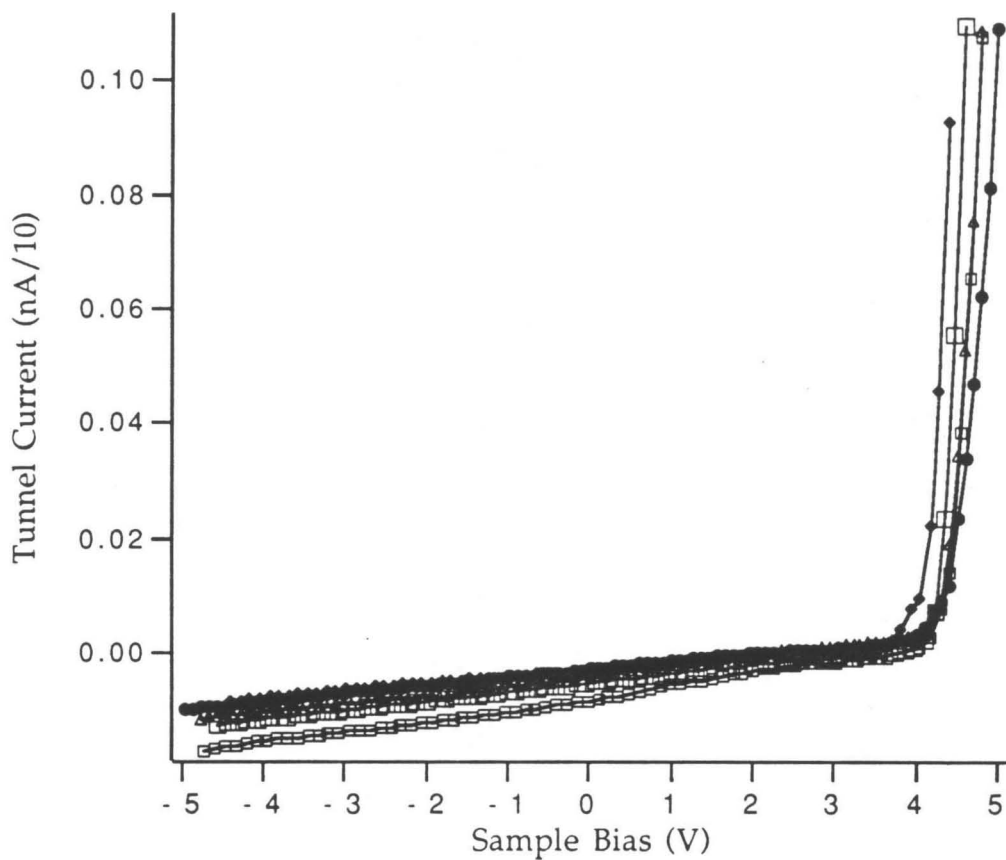


Figure 13: (BDIV067A-E) Series of IV curves at different tip-sample separation for feedback to 1 nA. The data was taken in air with a tungsten tip. Electrical contact was made to the stub with indium.

Natural Log of the Current as a Function of
Bias Voltage and the Corresponding
Linear Curve Fit for a Series of IV Spectra Taken at UHV

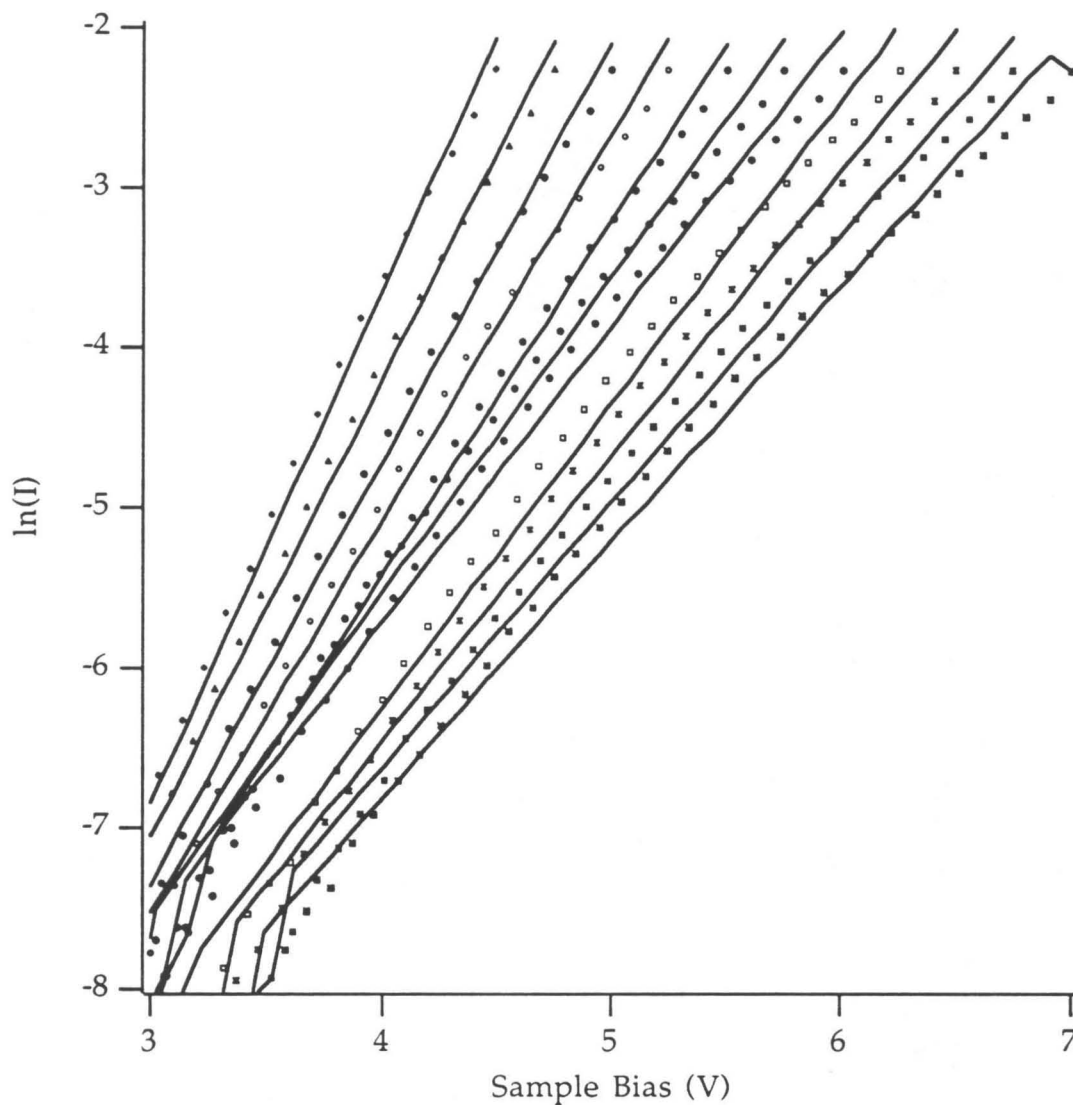


Figure 14: (BD258A-M) Graph of natural log of the current *versus* sample bias for the data of **Figure 8** shown by the points. Also included are linear fits to the data as solid lines. (The fits were performed only over the region above the noise, and thus the line beneath -7.5 appears jagged)

**Graph of the Calculated Surface Charge Density
as a Function of "n values"
for Various Depletion Widths and Tip-Sample Separations**

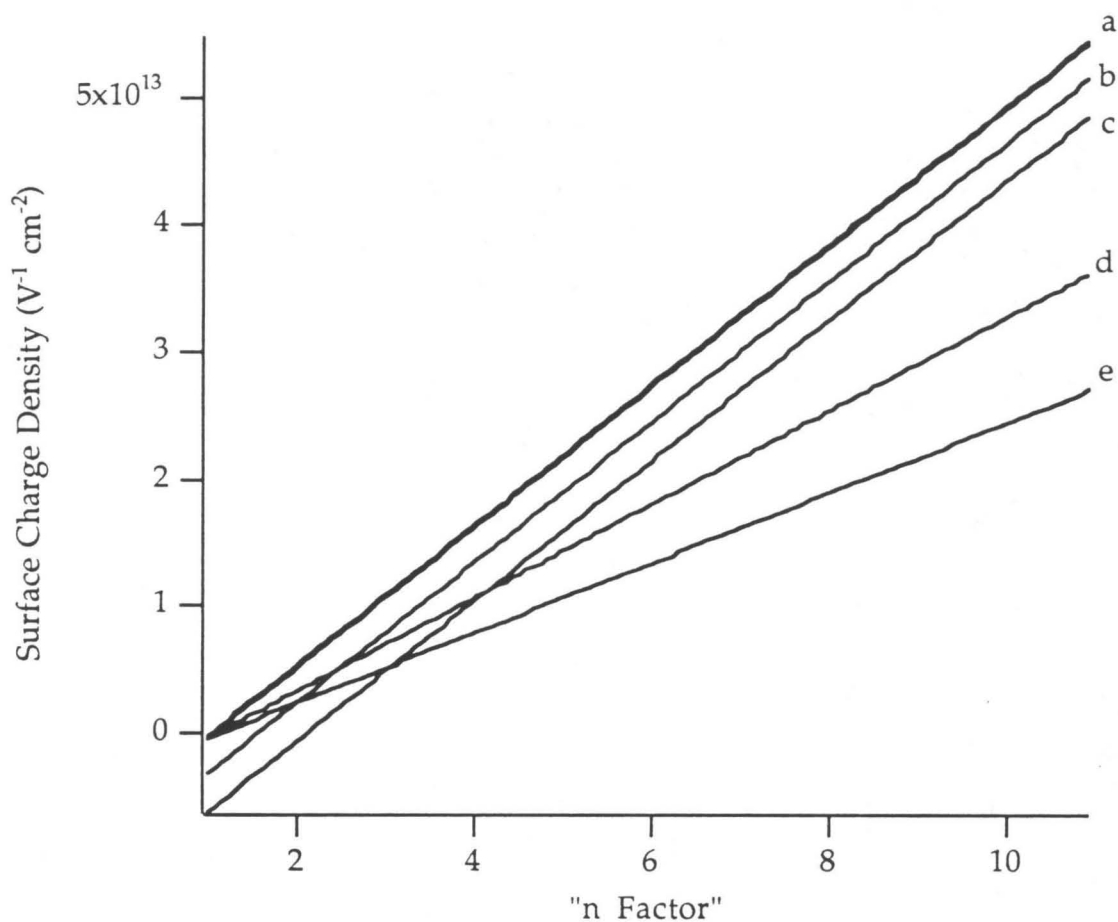


Figure 15: Calculated surface charge density required to give the measured "n factors" observed in the data of **Figure 14**. The plots correspond to constant values of the depletion width (W) and separation (s), both in Å identified as (W, s) for : a) (W ≥ 1000, 10), b) (100, 10), c) (50, 10), d) (1000, 15), e) (1000, 25).

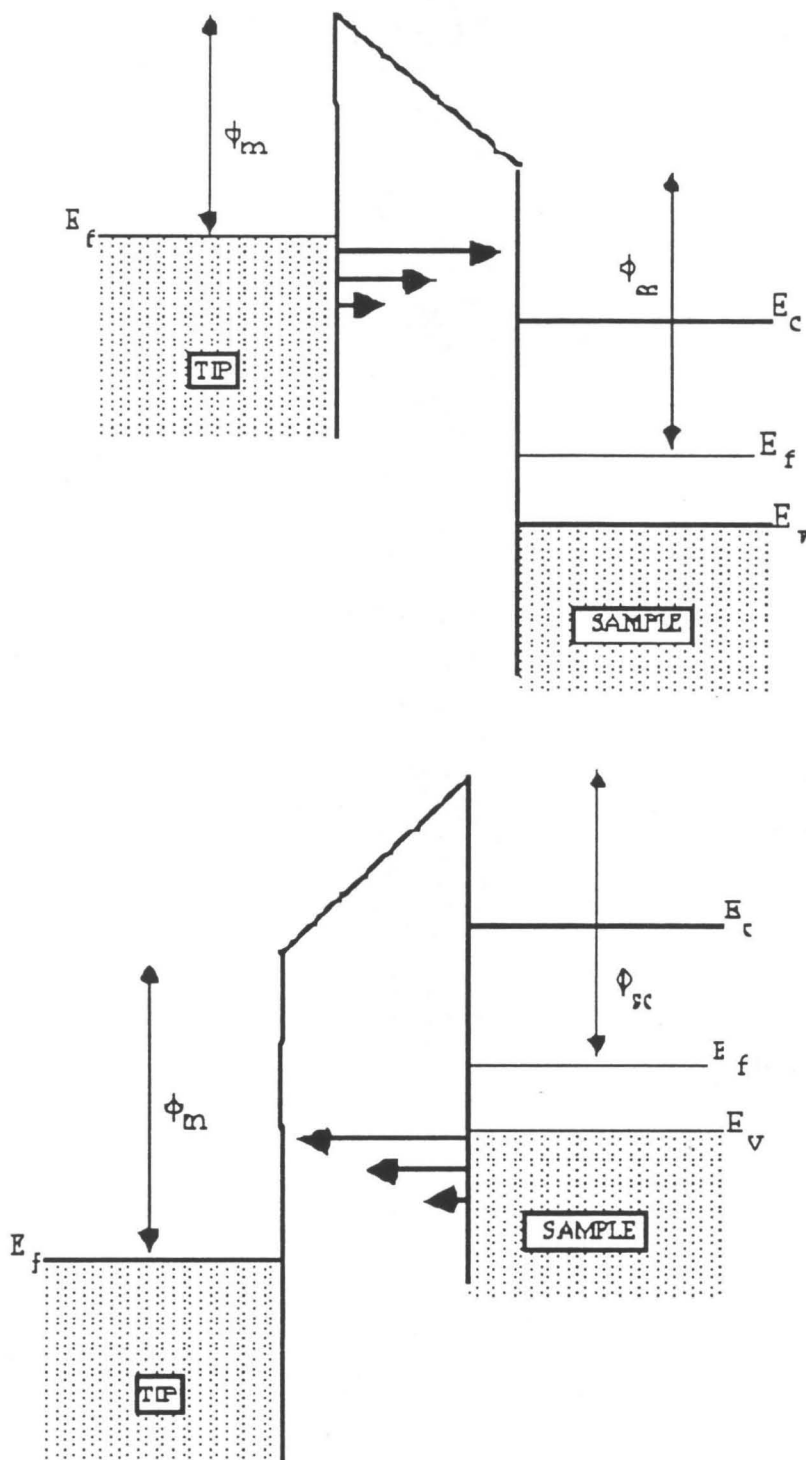


Figure 16: Comparison of tunneling probabilities to examine unfilled states (top) and filled states (bottom) of a semiconductor sample with a metal tip. The inability to see filled sample states because of the increased barrier felt by the electron at lower energy is discussed in the text. ϕ_m and ϕ_{sc} are the metal and semiconductor work functions. E_c , E_v , and E_f are the conduction and valence bands and the Fermi energy, respectively.

Appendix A

*DESIGN AND CONSTRUCTION OF AN
ATMOSPHERIC SCANNING TUNNELING
MICROSCOPE*

INTRODUCTION

Interest in studying biological molecules in their native environments has generated a new generation of STM construction. Although vibration isolation and electronic shielding are still important constraints in the design of an STM to be operated at atmospheric pressure, fewer constraints exist for sample mounting, and transfer, tip mounting and tip to sample approach than in traditional ultrahigh vacuum systems.

The system described in this *Appendix* is simple enough that it could be built and used by undergraduate students, given the appropriate guidance and sufficient time, and is robust enough to provide atomic resolution with easily accessible components. With that in mind, the approach of *Appendix A* will be somewhat tutorial in hopes that future students may use it accordingly.

A simple, rigid STM with a cantilever design for tip to sample approach and linear, analog feedback control of the tunneling gap was designed and built at Caltech. The original design was provided by Dr. William Kaiser of the Jet Propulsion Laboratory¹ and modified to provide more rigidity. This STM was used for all of the work described in *Chapter 2* of this thesis. The design considerations and subsequent operating parameters will be discussed. The actual designs for the STM are also included in *Figures 2-21* and are discussed in the text.

INSTRUMENT DEVELOPMENT

Vibration Concerns

Tantamount to the construction of an operable STM is the consideration of appropriate vibration isolation. Because the tip to sample distance must be resolved to less than 1 angstrom, the STM and vibration-isolation systems must be designed with consideration of both external and internal perturbations. The external vibrations are generally on a slow time scale from 1-100 Hz and are due primarily to building vibrational modes, acoustic noise and general seismic activity. Suppression of the transmission of these vibrations is accomplished by decoupling the STM from its

¹W. J. Kaiser and R. C. Jaklevic *Surface Science* 181, 55 (1987)

surroundings. Internal perturbations are primarily a result of the movement of the piezoceramics. Maximum stiffness and rigidity of the core STM is necessary to increase the natural frequencies beyond the internally generated vibrations and those of the environment.

Two quantitative factors regulating design parameters are the transmissibility and the stiffness of the system. These factors are discussed in detail in the thesis of John A. Kramar (Caltech, 1990) and will not be further discussed here. To summarize briefly, the STM should be isolated from low frequency oscillations by isolating the STM from the vibrations with an appropriate material—one with a resonant frequency as low as possible. Long springs and Viton elastomers are typically excellent choices. Moderate frequency perturbations that cannot be reduced by damping can be limited by internal stiffness of the STM. These vibrations are attenuated by a stiff material which, if used to fabricate a small, rigid STM structure, can have a resonant frequency well above a few tens of kilohertz.

The original STM designs used elaborate vibrational decoupling through magnetic levitation² and three-stage systems with two sets of springs in addition to eddy current damping³. Recent systems have been successful with damping on a stack of stainless-steel plates with viton spacers⁴ or a single-stage spring support⁵. With increasingly small STM design, merely suspending the STM from Viton o-rings has resulted in adequate stability⁶. Apparently, an ultrasmall STM produces sufficient rigidity to permit atomic resolution. The design of the Caltech atmospheric STM is both rigid and compact.

Tip Effects

The role of the tip structure in STM remains an unresolved question. The geometry of the tip has a significant effect on the vertical and horizontal resolution^{7,8}. Anomalous changes in image appearances have been attributed

²G. Binnig, H. Rohrer, Ch. Gerber and E. Weibel *Appl. Phys. Lett.* 40, 178 (1982)

³G. Binnig and H. Rohrer *Helvetica Physica Acta* 55, 726 (1982)

⁴Gerber, Binnig, Fuchs, Marti and Rohrer *Rev. Sci. Instrum.* 52 (2), 221 (1986)

⁵G. R. A. Van de Walle, J. W. Gerritsen, H. van Kempen and P. Wyder *Rev. Sci. Instrum.* 56(8), 1573 (1985)

⁶D. W. Abraham, H. J. Mamin, E. Ganz and John Clarke *IBM J. Res. Develop.* 30 (5), 492 (1986)

⁷Y. Kuk and P. J. Silverman *Appl. Phys. Lett.* 48 (23), 1597 (1986)

to "tip reconstruction"⁹. Although various studies of the tip structure and STM image have been endeavored^{7,8} correlation between the actual geometry and experimental STM results has still not been fully established.

Several theories have been proposed for the high lateral resolution. Tunneling is suggested to occur from the outermost atom of "minitips"¹⁰ or from a faceted cluster with a singlemost top atom¹¹. Debate continues as to whether a long, narrow tip allowing excursion into deep crevices is more favorable than a minitip which has much greater inherent stability¹². Any protruding structure on the gross tip can become the primary area of tunneling provided that it contain the nearest atom to the surface. Its effect will decay exponentially as the tunneling atom moves away from the surface. Ideally, the atom closest to the sample at a given time will effectively control the tunneling current. Methods for tip preparation vary and include grinding, cutting or chemically etching tungsten, gold, platinum or platinum-iridium wire with further processing by field desorption/evaporation, indirect electron bombardment, sputtering and annealing. Currently, a good tip is merely defined as one which gives a highly resolved image without reference to the actual tip structure.

Despite the lack of conclusive experimental data, theoretical calculations¹³ indicate that a tip radius of $<10 \text{ \AA}$ is necessary for such high resolution. J. Griffith¹⁴ claims to have compared tunneling from a single and double-atom tip and concludes that resolution is uniformly degraded with the two-atom tip. Kuk⁷ has shown, using FIM (field ion microscope) images of STM tips, that vertical resolution is also dependent on the size of the tip cluster. Characterization of the effects of tip geometry may well be one of the more important contributions to be made for the advancement and understanding of STM. Some of the importance of the tip can be gained by examining *Chapter 2*.

⁸C. Julian Chen *J. Vac. Sci. Technol. A* 9 (1), 44 (1991)

⁹J. Soler, A. Baro, N. Garcia and H. Rohrer *Phys. Rev. Lett.* 57 (4), 44 (1986)

¹⁰A. Baro, G. Binnig, H. Rohrer, Ch. Gerber, E. Stoll, A. Baratoff and F. Salvan *Phys. Rev. Lett.* 52 (15), 1304 (1984)

¹¹T. E. Teuchtwang, P. H. Cutler and N. M. Miskovsky *Phys. Lett.* 99A (4), 167 (1983)

¹²H. W. Fink *IBM J. Res. Develop* 30 (5), 460 (1986)

¹³J. Tersoff and D. R. Hamann *Phys. Rev. B* 31 (2), 805 (1985) and *Ibid. Phys. Rev. Lett.* 50 (25), 1998 (1983)

¹⁴J. E. Griffith (preprint) "Tunneling Images of a Tunneling Tip"

Operational Modes

Topography of surfaces or molecules is observed using two basic operational modes: slow and fast scan.

Slow Scan (Topographical or Constant Current Mode)

This method of operation was the first to be developed and is probably the technique most commonly associated with the STM. As the tip moves horizontally across a surface, the current, I_t , between the tip and substrate is kept constant by means of a feedback circuit. The feedback compensates for changes in I_t by expanding or contracting the z piezo ceramic. In this manner, the tip follows the surface contours and changes in LDOS. Since the current is exponentially proportional to the distance, s , from the surface, a small change in s causes a large change in the tunneling current. This change is reflected in the voltage required to return the operating current to the reference I_t . [Figure 1a]

This mode is functional for scanning at rates where the feedback circuit can keep up with the motion of the tip. Typically, a scan taken at a rate less than 100 Å/second is considered slow, but depends on the time constant of the amplifiers and electronics or sampling rate of the computer used. In order that the tip not "crash," the slow scan is the only feasible method of data collection for surfaces that are not atomically flat and for topology of large molecules. Unfortunately, molecular motion and isolation from instrumental and external vibrations become extremely important factors affecting the acquisition of interpretable data.

Fast Scan (Constant Height Mode)

In this mode of operation, the vertical position of the tip does not change relative to an average height above the surface, and the variations in tunneling current are measured directly. This mode is a more qualitative approach because the interpretation of the topography depends on a knowledge of the barrier height over the entire surface. The tip is rastered over the surface at a high enough frequency that the feedback circuit cannot follow the surface contours. Typically, a scan rate greater than 1000 Å/second is considered fast, but this rate depends on the bandwidth of the feedback

circuit of each system. The gain is minimized and the feedback time constant is maximized. Alternately, the feedback can be simply disconnected for samples with a very low barrier height. The changes in current resulting from the variation in distance between the tip and surface are used to build up the surface topographical and electronic image. [Figure 1b]

Methods to Characterize the Barrier Height, ϕ

From the basic equation for tunneling from a tip to an ideal planar surface, a series of related experimental modes can be constructed to evaluate the barrier height, current dependence on distance and gap resistance. The tunneling current for a planar metal-insulator-metal junction can be defined for the ideal 1-D case as

$$I_t = V_b \exp(-A\sqrt{\phi} s), \quad (1)$$

where $A = 2\frac{\sqrt{2m}}{h} = 1.025 \text{ eV}^{-1/2} \text{ \AA}^{-1}$, where h is Planck's constant and m is the mass of the electron. The measured current is $I_t = V_b R_g$, where R_g is the resistance of the gap. Thus, there are three ways to determine ϕ . By holding one variable constant, ϕ can be measured from the relationship between the remaining two variables. These types of experiments will give only an approximate barrier height since tip density of states¹⁵ and the image potential¹⁶ may affect the experimental results. Accordingly, ϕ is more accurately described as an average effective barrier height, although the average work function between the two electrodes is often an adequate approximation.

1. Constant Current $(dV/ds)_I$

By maintaining I_t with the feedback circuit, V_b is ramped and the gap resistance is measured. Experimentally, this quantity is reflected as a change in the z ceramic, which is converted to relative distance. Since $\ln V_b = A\phi^{1/2}s - \ln(I_t)$, ϕ can be determined.

¹⁵R. M. Feenstra, J. A. Stroscio and A. P. Fein *Surface Science* **181**, 295 (1987)

¹⁶John A. Kramer, Michael Weimer and J. D. Baldeschwieler *Phys. Rev. B* **39** (8), 5572 (1989)

2. Constant Bias Voltage $(dI/ds)_V$

The sample bias is preset and I_t is measured as the tip to sample distance is varied. Experimentally, the voltage across the z ceramic is ramped, and these data as distance are plotted versus the $\ln(I_t)$ observed. The barrier height, ϕ , can be calculated from the slope.

3. Constant Gap Resistance $(dI/dV)_s$

For the voltages used in STM, I-V curves are usually ohmic. This technique relies on a series of I-V measurements keeping a constant distance (s) between tip and sample for each curve. The feedback is disconnected so that the z ceramic is stationary. Distance is not absolute, so s must be determined from sequential experiments. I_t is measured while V_b is ramped for a series of gap resistances, $R_g(s)$. Recalling that $\ln(\frac{I_t}{V_b}) = -\ln R_g = -A\phi^{1/2}s$, the barrier height can be calculated from a plot of $\ln R_g$ versus Δs .

INSTRUMENT DESIGN

Core STM

The core STM built was adapted from the original design of William Kaiser and J. C. Jaklevic¹. This design is ideal for applications at ambient temperature and pressure studies because it has a manual mechanical approach that can easily be converted to computerized control by the use of stepper-motors. Controlling the tip-sample spacing and minimizing vibrations are difficult with previous designs such as a "louse" because the tip and sample are on two separate structures. In the Kaiser design, the tip and sample are mounted on a single stage so that vibrations are felt equally. Also, the large voltages associated with clamping the louse feet are avoided. The modifications made to Kaiser's design include adding another support bar for the coarse adjust screw and a "T" across both bars in order that maximum stability of the system is attained when adjusting the coarse screws. [Figure 2] The complete design is found in Figures 3-9.

The coarse approach of the sample to the tip relies on a simple cantilever mechanism. The tip is located between the two coarse adjust screws (4-40) and protrudes through an aperture in the quartz plate resting on the screws. Held in a 22-gauge needle shaft within an 0-80 alumina tube, the tip is

mounted atop the z piezo. [Figure 10] At the opposite end of the STM, a fine adjust screw (0-80) supports the other end of the plate. A small stainless-steel crank is spot-welded to the end of this screw so that fractional turns are easily performed.

The sample to be studied is placed on the quartz plate over the aperture and lowered to the tip by turning the coarse adjust screws. The approach is monitored optically with the naked eye or a microscope. When the tip and sample are "close" (within $\sim 1\mu\text{m}$), the fine adjust screw is turned to lower the sample to the tip where the feedback circuit will keep the tip within tunneling range. Demagnification of the z motion through this cantilever configuration results in the ability to approach in steps $< 100 \text{ \AA}$.

Crashless approaches are consistently made. Often this involves lowering the fine adjust screw full range without tunneling, retreating full range with the fine adjust screw, turning the coarse adjust screw $< 1/4$ turn and attempting the fine approach again. This process is repeated until successive iterations place the tip and sample within tunneling range. The major advantage of this design is that changing samples is facilitated by easy access. One can "back off" the tip from the original sample with the fine adjust screw, replace the sample while remaining very close to tunneling range. The approach time is thus minimized.

Piezoelectric Ceramics

The piezoelectric ceramics used are cut to specifications shown in Figure 11. The material, PZT-24050-4 discs from Vernitron Piezoelectrics, is a lead zirconate-lead titanate (PZT), polycrystalline ceramic that expands or contracts when an electric field is applied across it¹⁷. Because the ceramic is very brittle, cutting the x-y translator is tedious, and care must be taken to avoid snapping the piece.

For piezo-ceramics used here, the expansion coefficient has been calibrated at 10 \AA/V for the x-y translator and 16 \AA/V for z by optical interferometry¹⁸. The resonant frequency, f_{res} , of the y piezoceramic was tested by sweeping the frequency of scanning the x piezoceramic and

¹⁷Vernitron Piezoelectric, GRU Associates, 1105 E. Commonwealth Ave., Fullerton, CA 92631

¹⁸Dr. William Kaiser, Jet Propulsion Laboratory, Pasadena, CA. Private communication. Summer, 1986.

determining the frequency at which the y amplitude was enhanced. The same test was performed for the x ceramic. Both x and y ceramics had $f_{\text{res}} > 6$ kHz and are comparable to proven STM systems at the time of its construction¹⁹.

Thermal drift and hysteresis are common annoyances associated with these piezoelectric ceramics. Thermal drift is on the order of a 4-6 Å/min and is thus not a problem for the fast scans. In slow scans, a large drift could place the atoms out of register but can be corrected in data processing as long as the drift is constant. The problem of tip hysteresis is minimized by collecting data in only one direction. These effects can be characterized and further corrected in computerized data analysis and manipulation.

Vibration Isolation and Shielding

Vibration isolation is accomplished using a single stage, three-spring stand. Specific design specifications are found in **Figures 12-13**. The inner ring stage is designed so the STM can be solidly bolted onto the stage, which is suspended from three springs and damped with Viton. Aluminum rods 1/2" in diameter and threaded on each end are used as supports and mounted in a solid baseplate. The body of the core STM is composed entirely of 304 stainless steel and is of minimum size so that maximum rigidity is maintained. The resonant frequencies of a stiff structure of these materials and size are consistent with established parameters for effective gap stability²⁰.

The experimental resonant frequency, f_{res} , of the undamped springs is 0.88 Hz with a quality factor $Q = 650$. Because the enhancement at resonance of the transmitted vibration is proportional to Q , the experimental Q should be small. By weaving Viton strips through the springs, damping is introduced, which slightly raises the f_{res} to 0.93 Hz, but lowers Q to 8.

Viton proves to be an excellent material for providing vibration isolation for the entire structure. Viton bands holding the stage near the support rods damp the horizontal modes. The stage is completely decoupled vertically from the support structure by Viton o-ring suspension. [**Figure 14**] The rods supporting the structure are seated in o-rings placed on silicone

¹⁹P. Muralt, D. Pohl, W. Denk *IBM J. Res. Develop.* 30 (5), 443 (1986)

²⁰Dieter Pohl *IBM J. Res. Dev.* 30(4), 417 (1986)

rubber pads. Acoustic shielding is provided by placing the entire system in a cardboard box with corrugated foam interior.

Vibrational studies on the STM work space in Room 17 Noyes indicate significant building vibrations. Using an ss-1 Ranger Seismometer and spectrum analyzer, the resonant frequencies with the largest amplitudes on the floor were found at 6-12 Hz and 20 Hz, each at 1.2 μm vertical amplitude. Analysis of the workbench upon which the STM was initially located indicated a 10-fold increase in amplitude in vibrations at 20 Hz. These amplitudes at 6-12 Hz and 20 Hz were 1.3 μm and 12 μm , respectively. The STM was relocated on the floor.

Electronics

In the construction of electronic circuits both to control and to monitor currents in the nanoampere range and submillivolt potentials, special care must be taken to reduce internal capacitance, inductance, and coupling as well as any outside electrical interference. The need for a common ground separate from chassis ground (or power ground) has been well established²¹. In order to avoid any ground loops that create differences in the reference ground seen by different components of the system, *each* circuit was constructed with ground to an isolated common. This common was then pulled to a single ground.

The STM vibration isolation frame is grounded to avoid creating a potential around the tip and preamp. The core STM and stage are electrically isolated from the stand by the insertion of Viton o-rings between the plate and washers and by suspending the springs from the insulating rings [see **Figure 14**].

The overall design for the electronics system is sketched in **Figure 15**. Modular NIM crates were chosen in order to insure compatibility with both William Kaiser's group at JPL and the UHV STM at Caltech. The NIM power supply used had acceptable peak-to-peak (p-p) noise < 100 mV on the ± 12 and ± 24 V supplies. This noise was reduced on all boards with filters and better grounding. The 24 V supply was down-regulated to 15 V to power the RCA3140 operating amplifiers (op amps). The noise associated with the

²¹Ralph Morrison *Grounding and Shielding Techniques in Instrumentation* (John Wiley & Sons, Inc.: New York), (1977)

tunneling current, with power turned on to all circuits but with no tunneling from tip to sample, was 20 pA. This deviation represents < 1% of normal operating current. The specific circuit diagram for each board is located in **Figures 16-21**. Some special features of the circuits are described as follows:

Feedback: [Figure 16] The main function of this circuit is to allow a constant tunneling current to be maintained between the tip and the sample. This result is attained by comparing the measured current to an externally established reference current and compensating for any differences by varying the voltage across the z piezo. By establishing a constant I_t and V_g , a constant gap resistance is maintained, which corresponds to a certain impedance between tip and sample. Monitoring the voltage applied on the z piezo to maintain the constant current distinguishes topographical or electronic features on the surface. Other features of this circuit include a variable gain, variable time constant (RC), polarity reverse switch for the ability to tunnel from tip to sample or sample to tip, and room for a sample and hold integrated circuit for future computer interfacing²².

Preamp: The amplifier is mounted directly on the core STM to minimize any capacitance coupling between the electrical lines. The preamp is a noninverting amplifier and has a gain of 10. The tunnel current is measured as the voltage dropped across a 10M Ω resistor. Normal operating range is 2-10nA which corresponds to 2-10 mV.

High Voltage Board: [Figure 17a] The x, y, and z piezos all have the ability to scan a bipolar 150V range that corresponds to 3000 Å for x and y and 4200 Å for z. Power is supplied to Burr-Brown 3584JS high voltage operating amplifiers using DATEL BPM-150/20 modular supplies, which make the STM electronics not only more compact but also less expensive and easier to repair than if common, regulated bipolar supplies are used. The DATEL's are adequate for the present applications. Future studies on large molecules with the need for micron-range scan abilities could require the use of bimorphs, piezoelectric ceramics that have greater expansion coefficients and greater power demands or x-y translation stages.

²² Dr. William Kaiser, JPL, provided the initial circuit design and subsequent consultation.

Sample Bias: [Figure 17b] This board allows either a positive or a negative bias to be put on the sample. An external port provides the ability to perform I/V and time-dependent studies.

X and Y Offset: [Figure 18] This circuit provides the ability to move the viewing window on x and y by adding a dc offset to the scan range parameters. The use of this board was extended to give manual control of the z ceramic for studies when feedback is disconnected.

Contrast/Blanking/Brightness: [Figure 19] This board provides a means to display the data collected in a fast scan mode on a variable-persistence storage oscilloscope by modifying the monitored I_t . The intensity of the signal on the oscilloscope depends on the magnitude of the voltage received. Contrast is modulated with a variable gain amplifier, brightness by a variable dc offset and blanking by sending a 10 V shutoff signal when x is scanning in the negative direction.

Integrator/Summing Amplifier: In the slow scan mode, the integrator [Figure 20] adds an offset to the y axis after each scan in the x direction. X is blanked in the negative x direction. The summing amplifier [Figure 21] adds an operator-chosen, weighted ratio of z to y in order to produce line scans of axes x vs y+z.

Operating Parameters

The high voltages associated with driving the piezos can create electrical pick-up on the proximal preamp. The electrical noise was tested by examining ac coupling to the preamp. The x and y ceramics were driven at 350 Hz with a triangular waveform 20 V p-p. The preamp pick-up from x and y were 0.9 mV and 0.7 mV p-p, respectively, in a square waveform because of the derivatization of the input by the stray capacitance. The output amplitude was proportional to the frequency of the input. To decrease the effect of the driving voltages, a small aluminum plate was placed over the ceramics to act as an electric shield. The preamp pick-up from the x and y ceramics was reduced to <0.5 mV and <0.1 mV p-p, and is within operating limits

To test the leakage or ac coupling between the piezoceramics themselves, a triangle waveform at 250 Hz, 20 V p-p was placed across one ceramic, and the induced voltage of the second was monitored. X and y affected each other similarly, giving 30 mV noise at the same frequency as the

input with a slightly altered waveform that was due to the RC effect. This 1.5% pick-up is within tolerable operating limits.

Data Collection

Two methods of data collection corresponding to the two modes of operation are used. For the slow scan, graphs of x vs $y+z$ are directly plotted on an XY chart recorder. Alternately, the scans are displayed on a permanent-storage oscilloscope where a Polaroid picture could be taken.

Fast scan data is collected as grey scale data, where x and y are the axes and Z is displayed as brightness (where the brighter spots correspond to higher tunneling currents and higher points on the surface) on a Tectronix 7633 variable-persistence storage oscilloscope. Data were recorded on a Panasonic PV 4560 VCR and displayed on a Magnavox Computer Monitor 80. The VCR has special features for high picture stability on slow playback and freeze-frame without drift for clear polaroid pictures. VCR images can be "captured" from the frozen screen by "Image Ace" software and subsequently analyzed by any image processing techniques available.

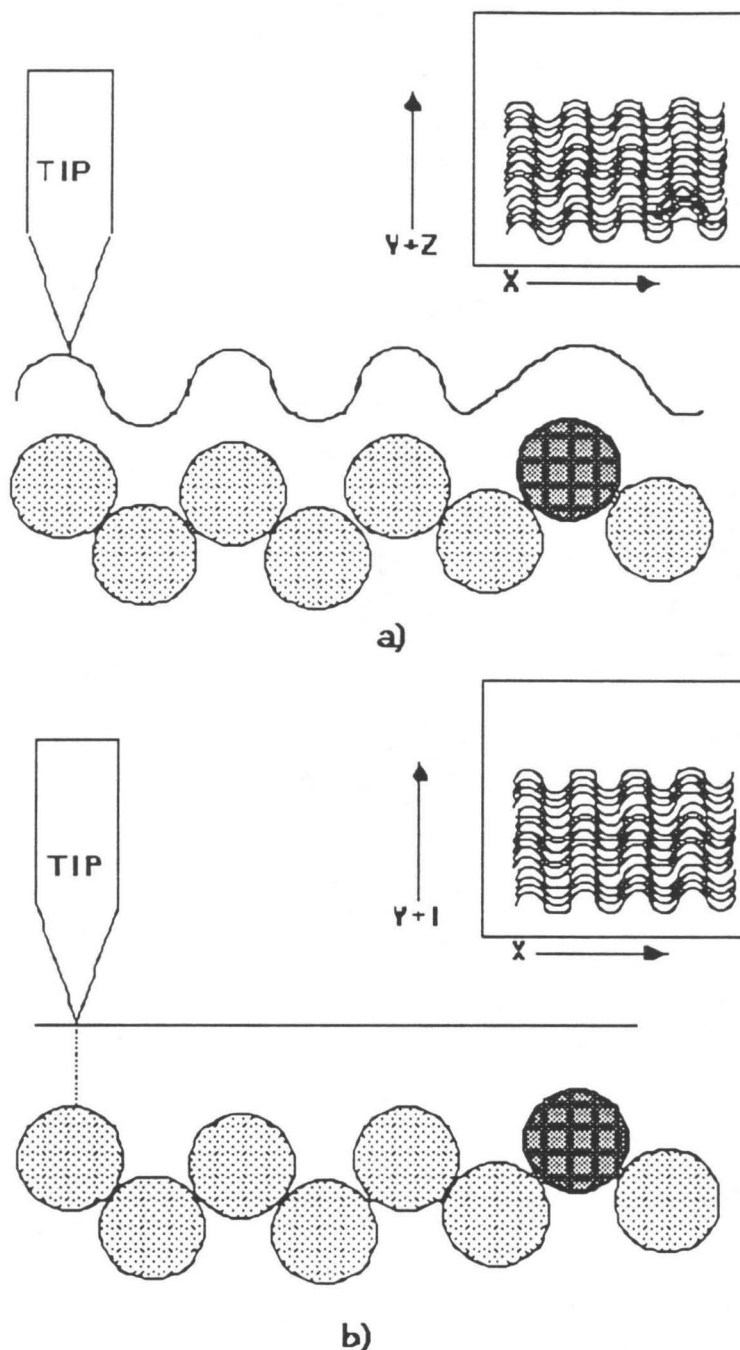


Figure 1: a) Slow scan or constant current mode (often called topographic mode). The feedback is set to a constant current so that the tip follows the surface contours and is sensitive to changes in electronic density that are due to adsorbates or surface anomalies. The height variations in the image are derived from the voltages used to move the z piezoceramic. b) Fast scan or constant height mode. The feedback time constant is set so that the tip cannot respond to the small variations in height. The resultant variation in current measured by the tip is used to provide the image contrast.

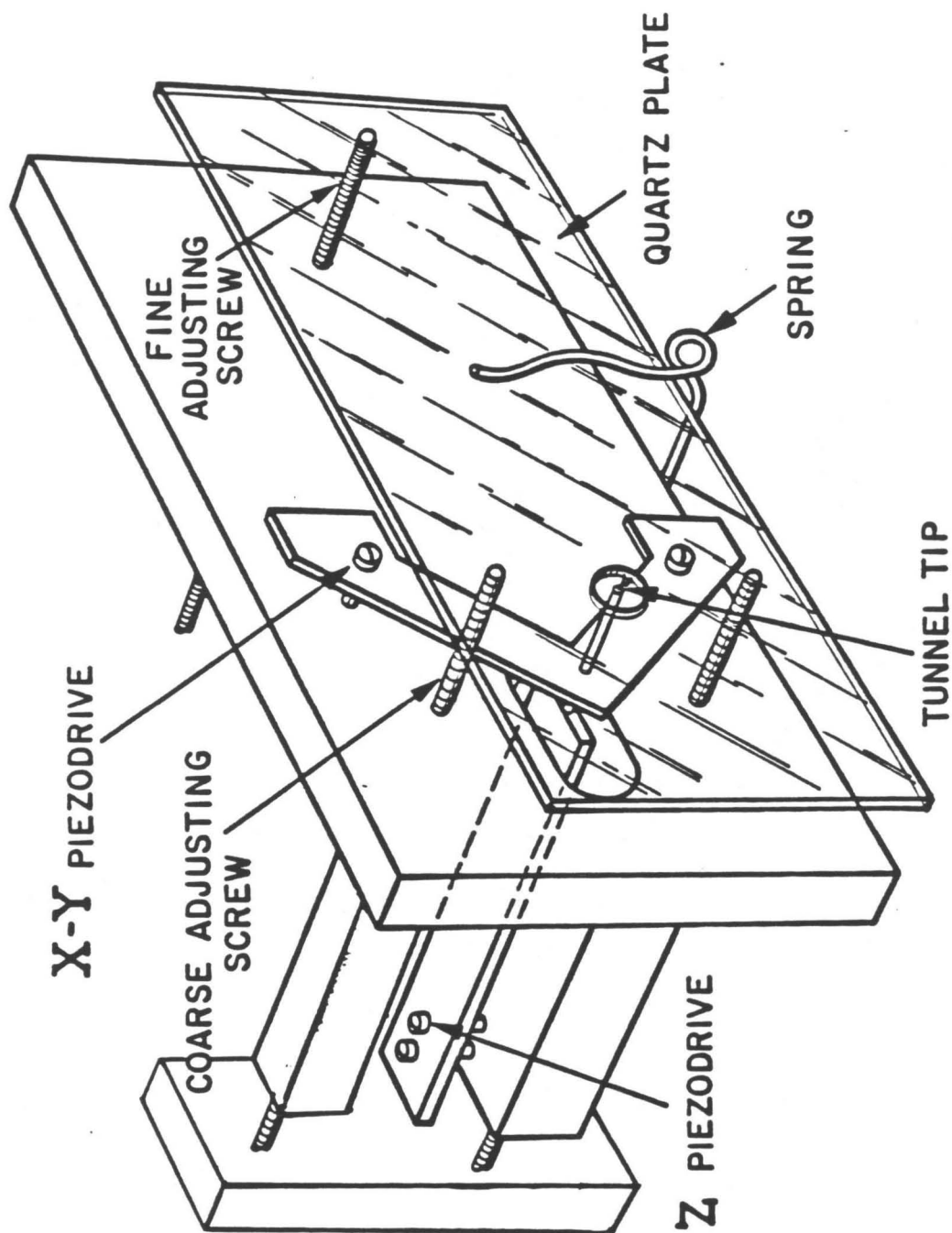


Figure 2: The core STM based on a design by Dr. William J. Kaiser at the Jet Propulsion Lab. The actual body is only three inches long. Being very compact, the rigid structure reduces transmission of low frequency vibrations. The function of the screws is explained in the text.

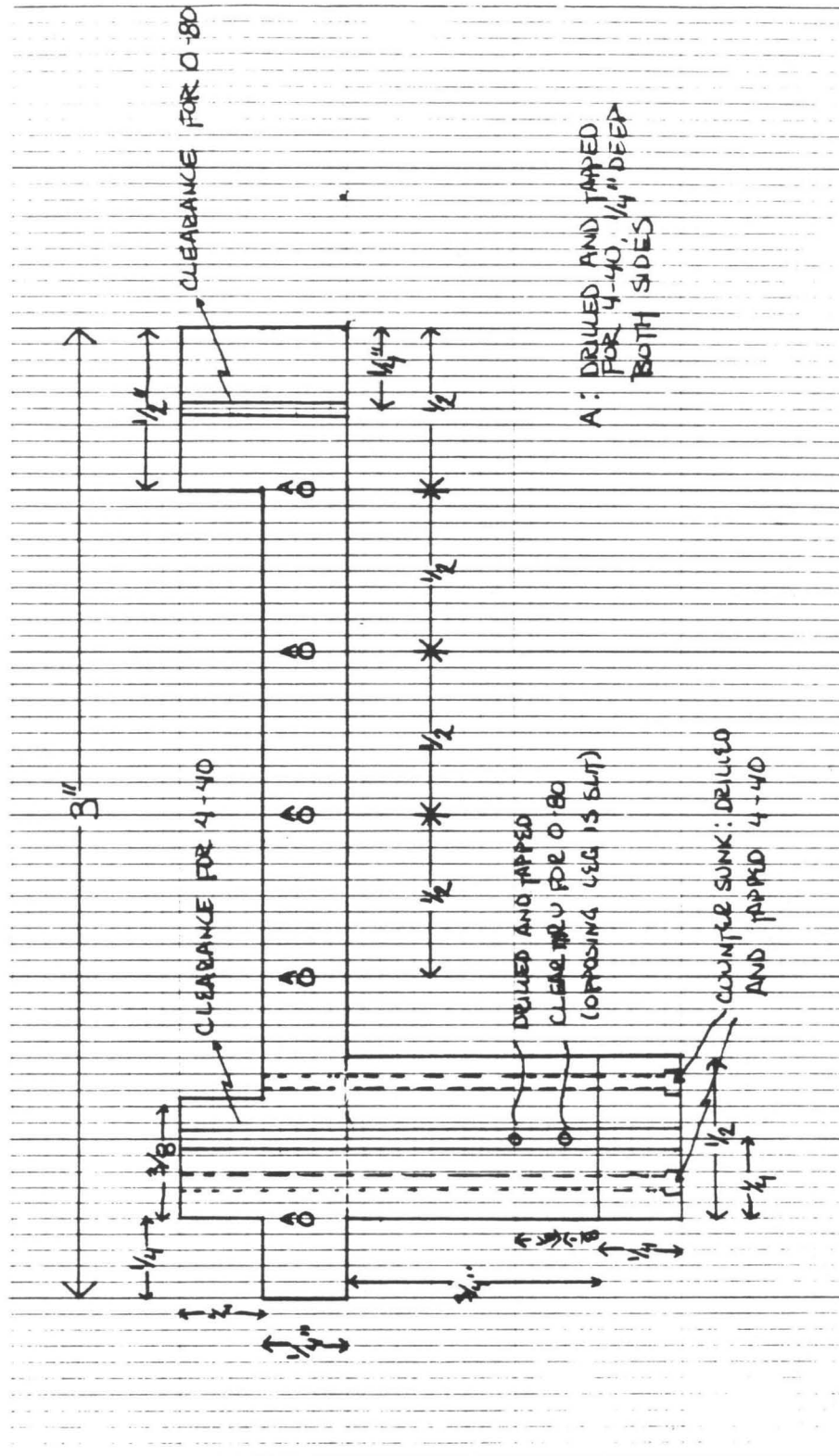


Figure 3: Side view of the STM frame with the T-bar attachment.

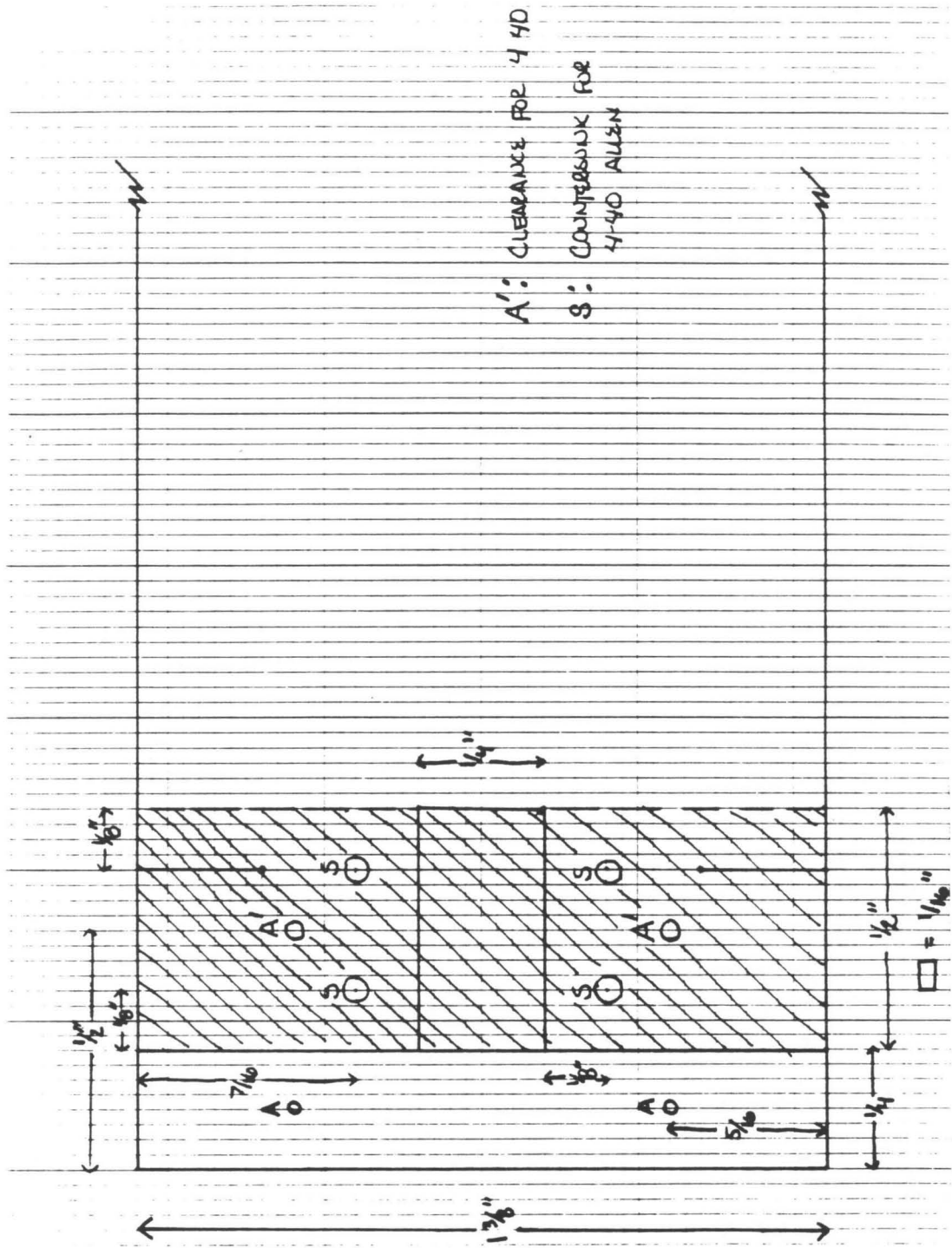


Figure 4: Top view of the STM T-bar end to highlight the T-bar overlay.

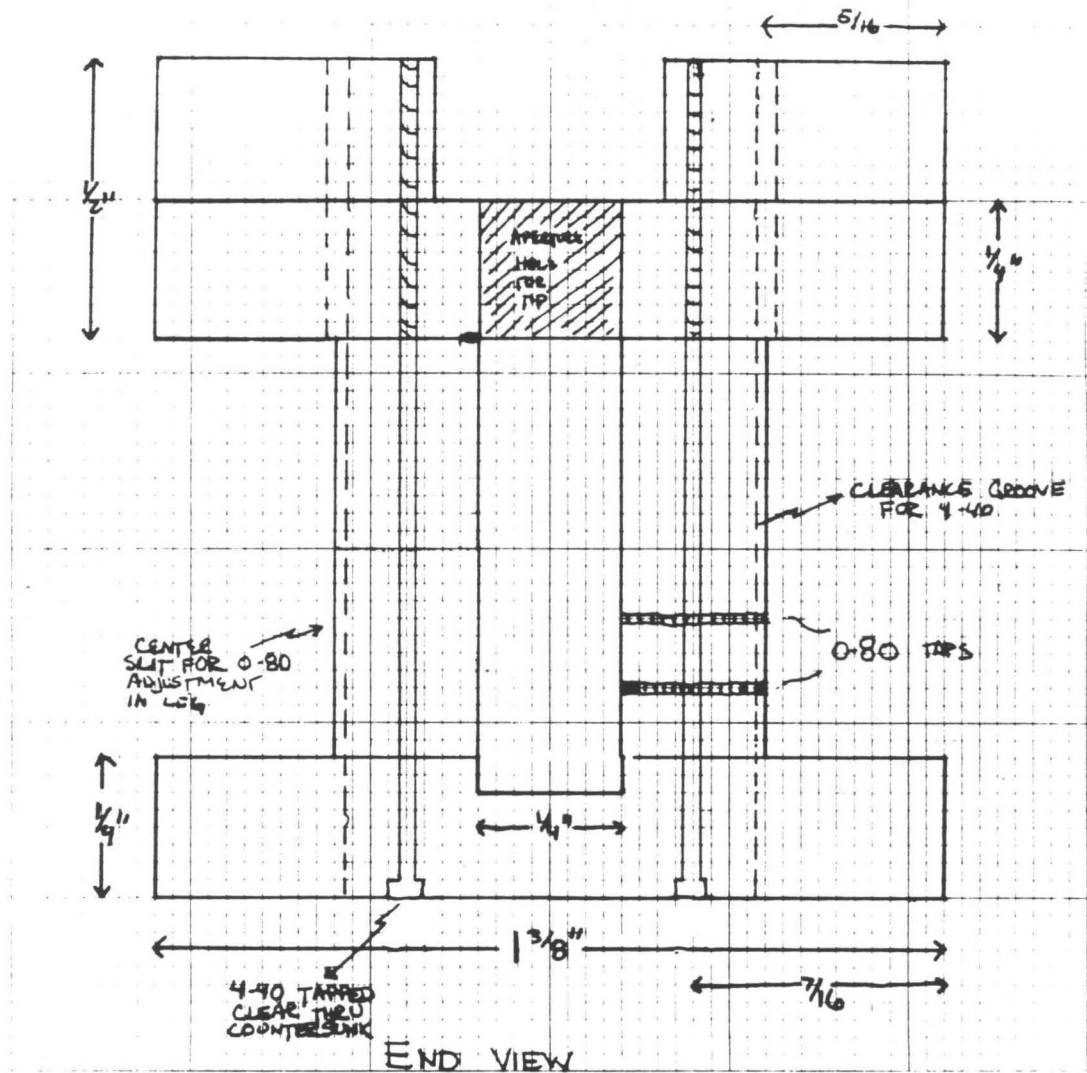


Figure 6: End view of the STM frame with the T-bar attachment showing detail for tip aperture and z-piezoceramic attachment.

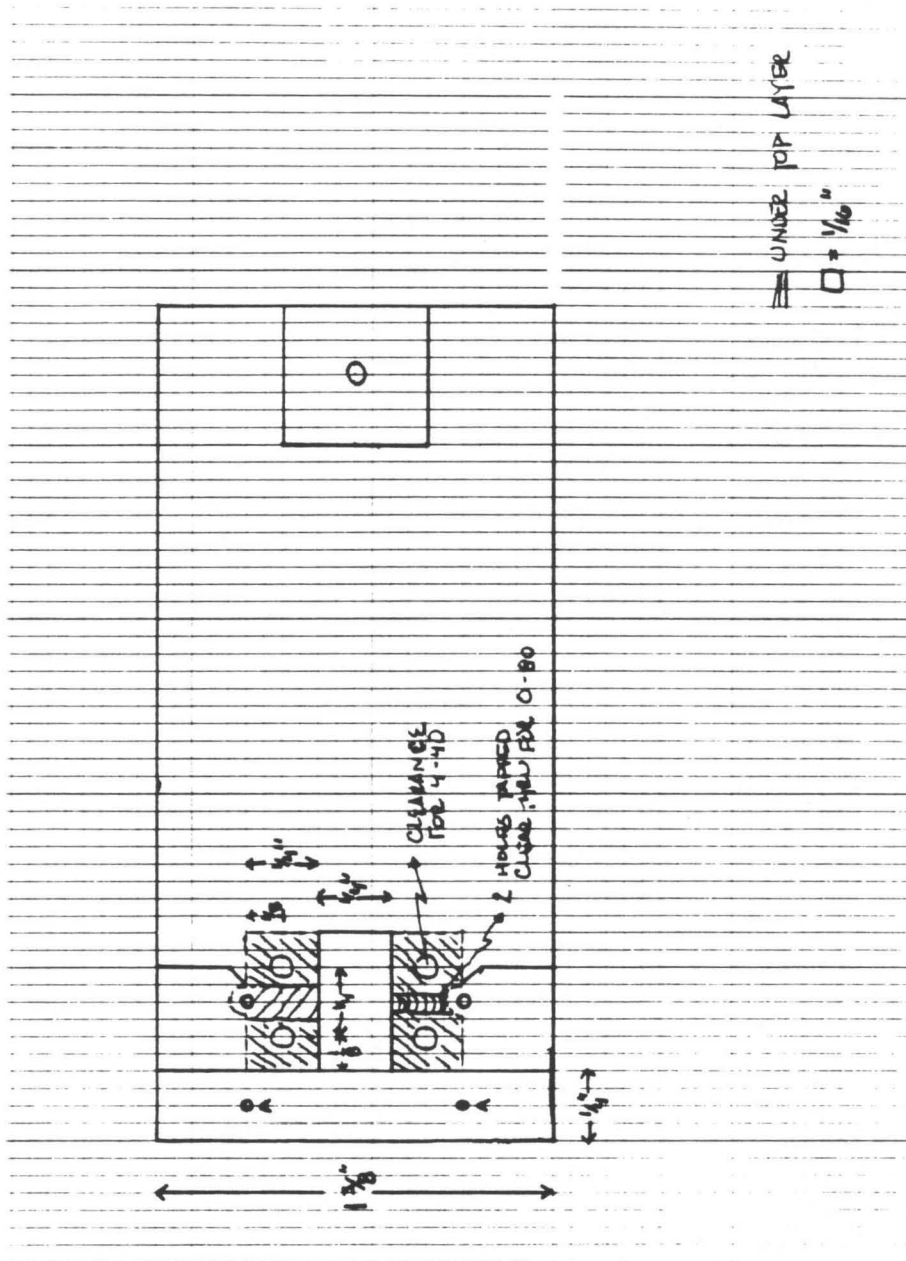


Figure 7: Top view of the STM frame with detail of leg attachment.

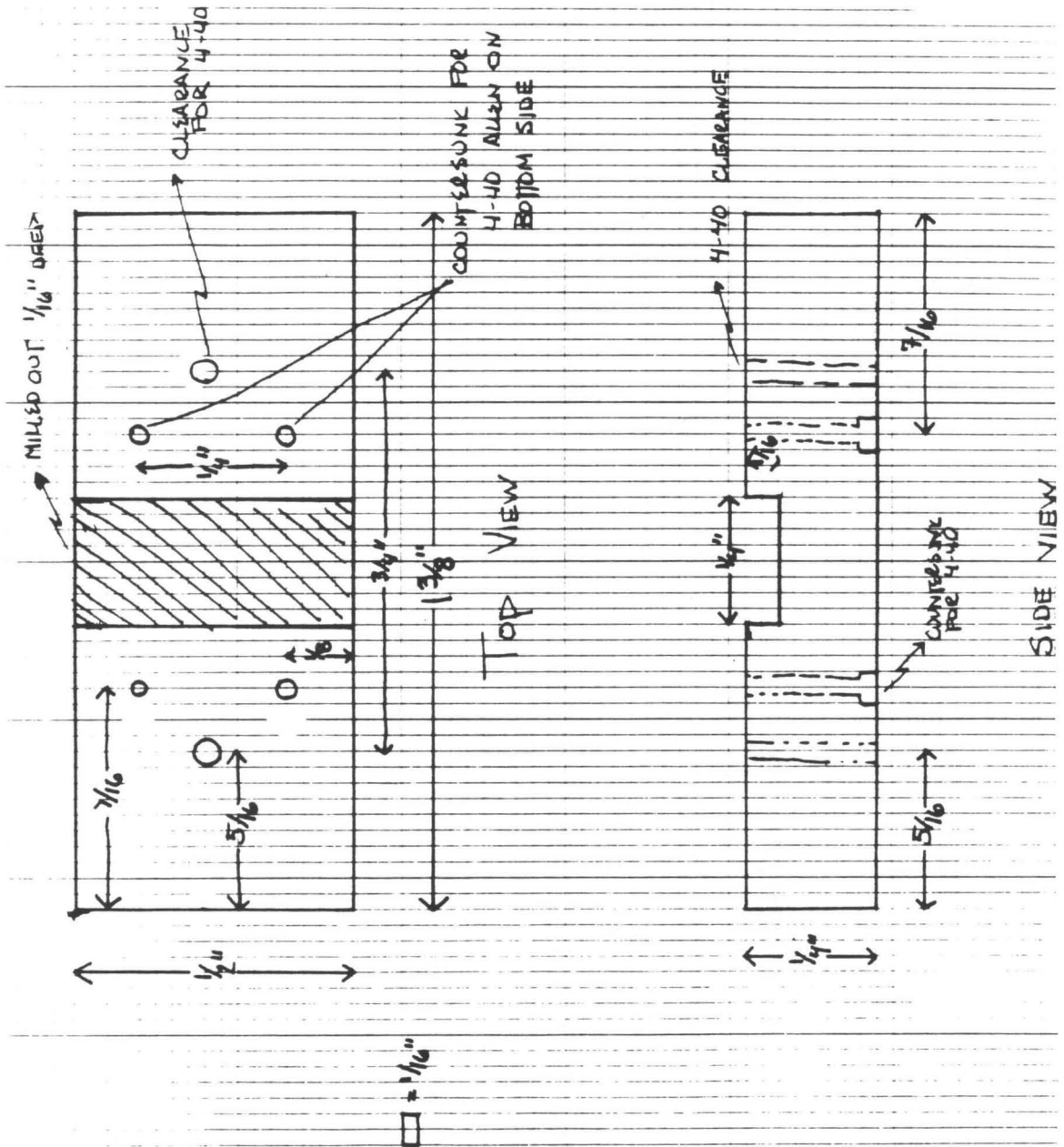
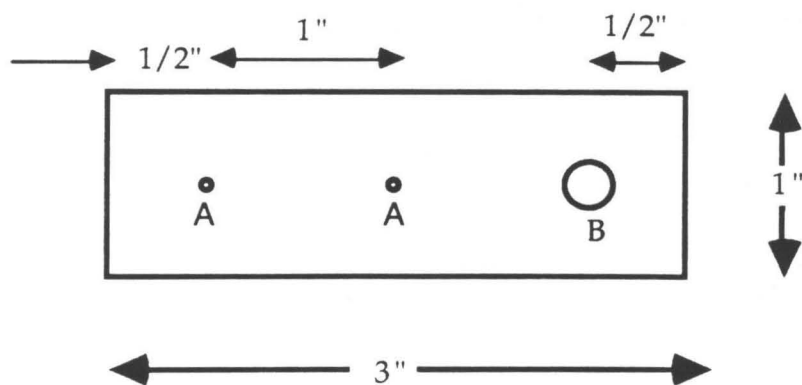


Figure 8: Top and side view of the T-bar attachment.



A = 1/16" diameter

B = 1/4" diameter

Quartz Plate ~1/16" thick

Figure 9: The quartz plate sample holder.

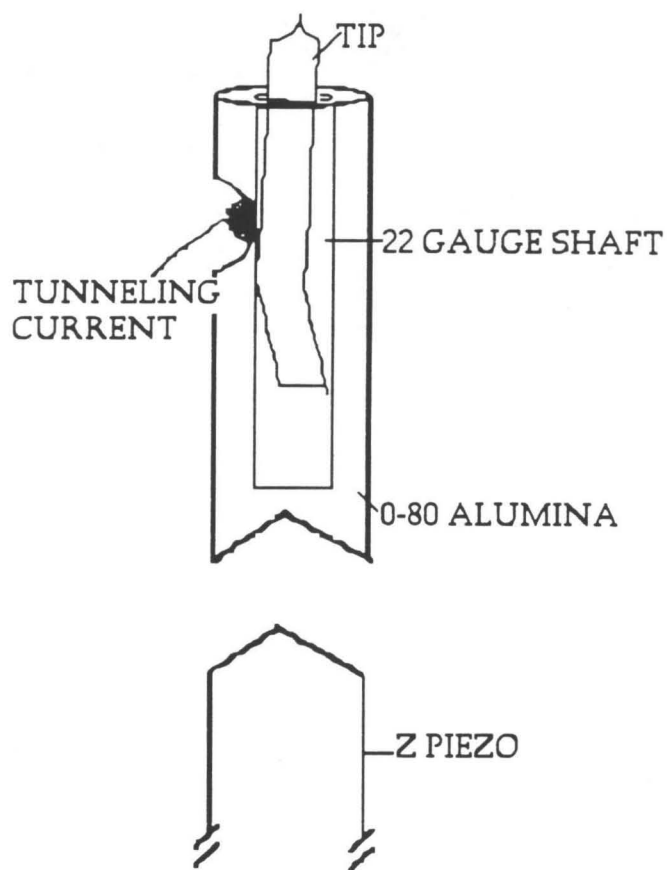


Figure 10: Schematic diagram of the tip holder. The tip wire is kinked in order to secure it within the steel shaft. The shaft is insulated in an alumina tube, and the tunneling current is fed directly to a preamp mounted on the STM.

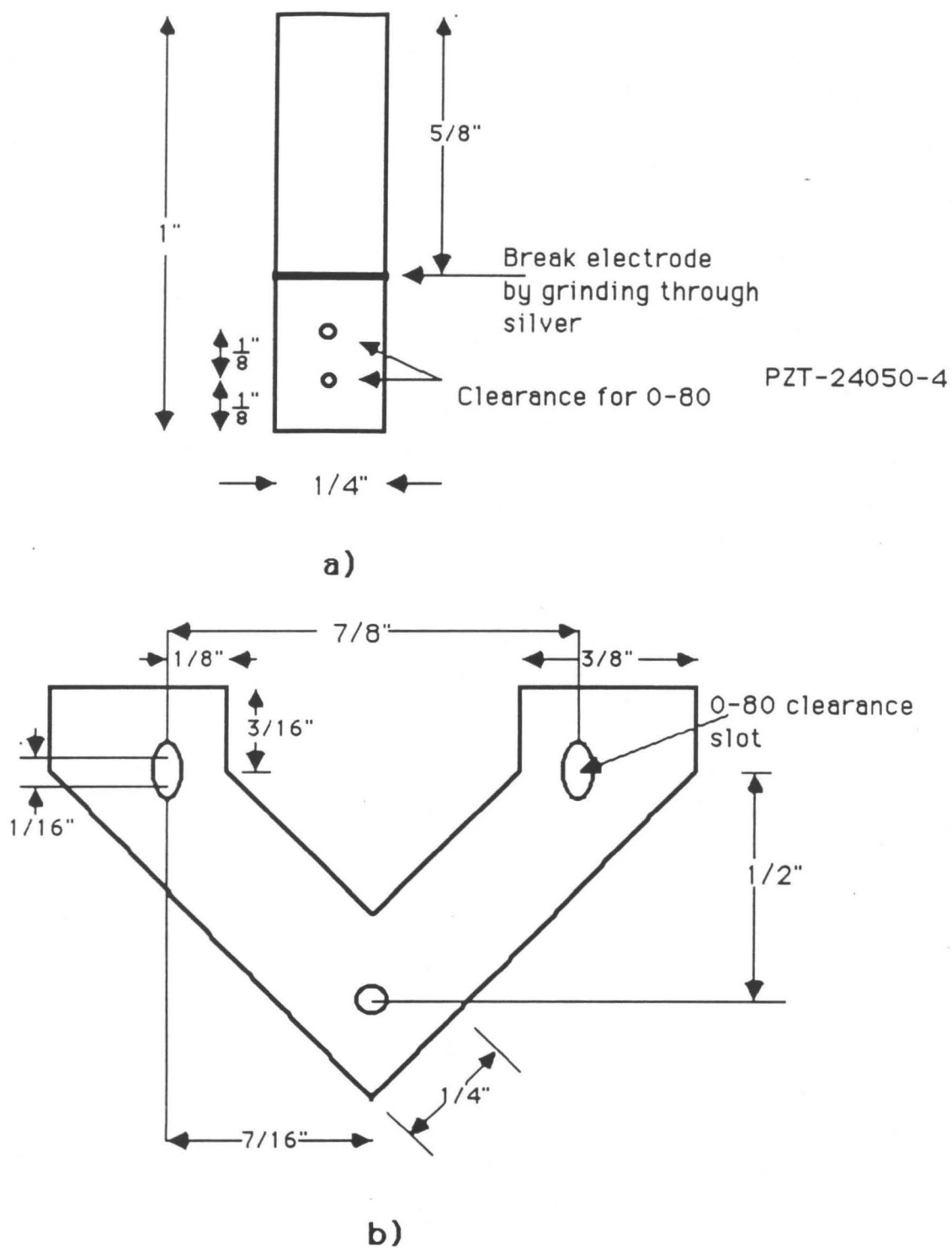


Figure 11: The piezoceramics. a) the z piezoceramic and b) the x-y piezoceramic.

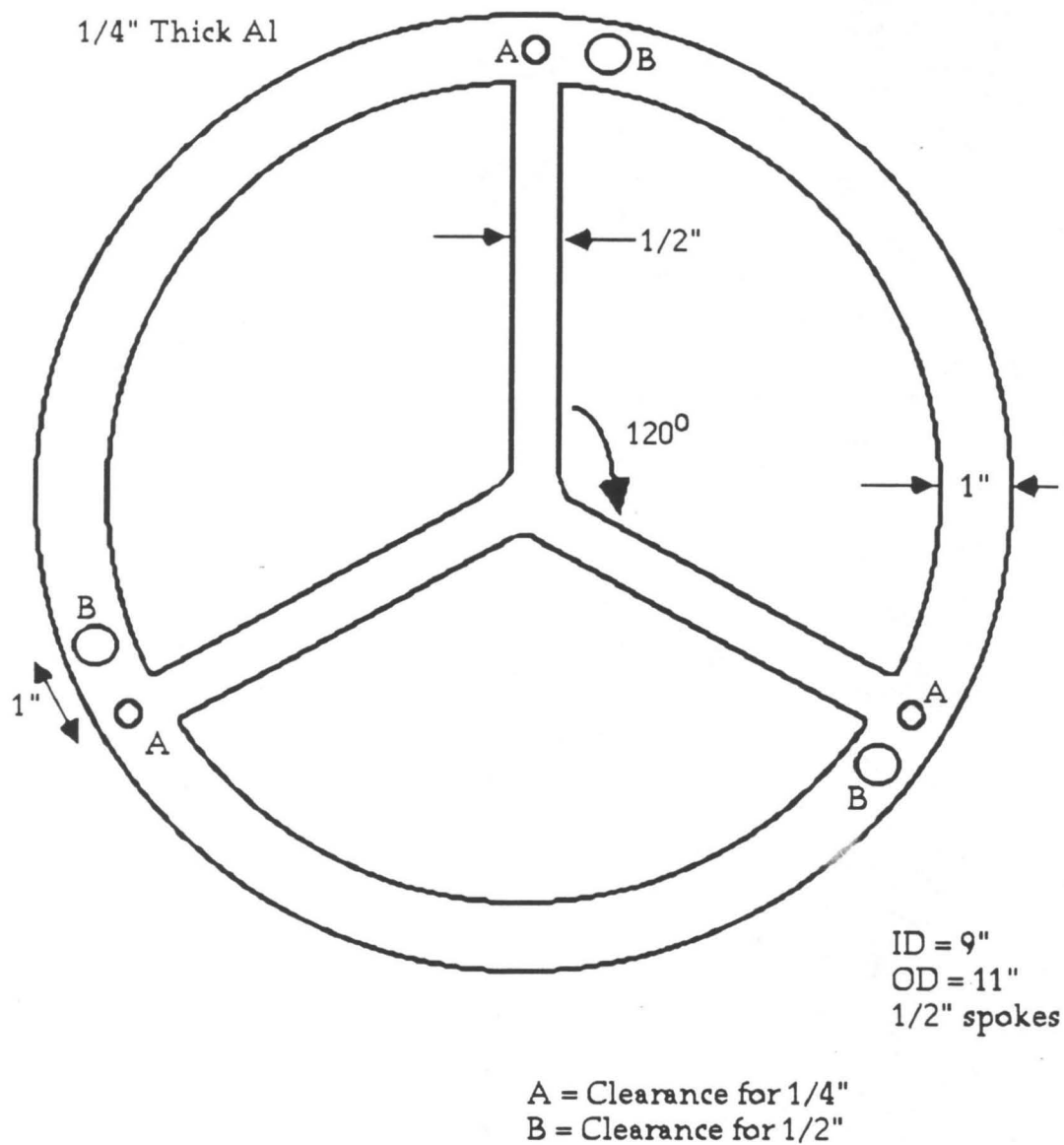
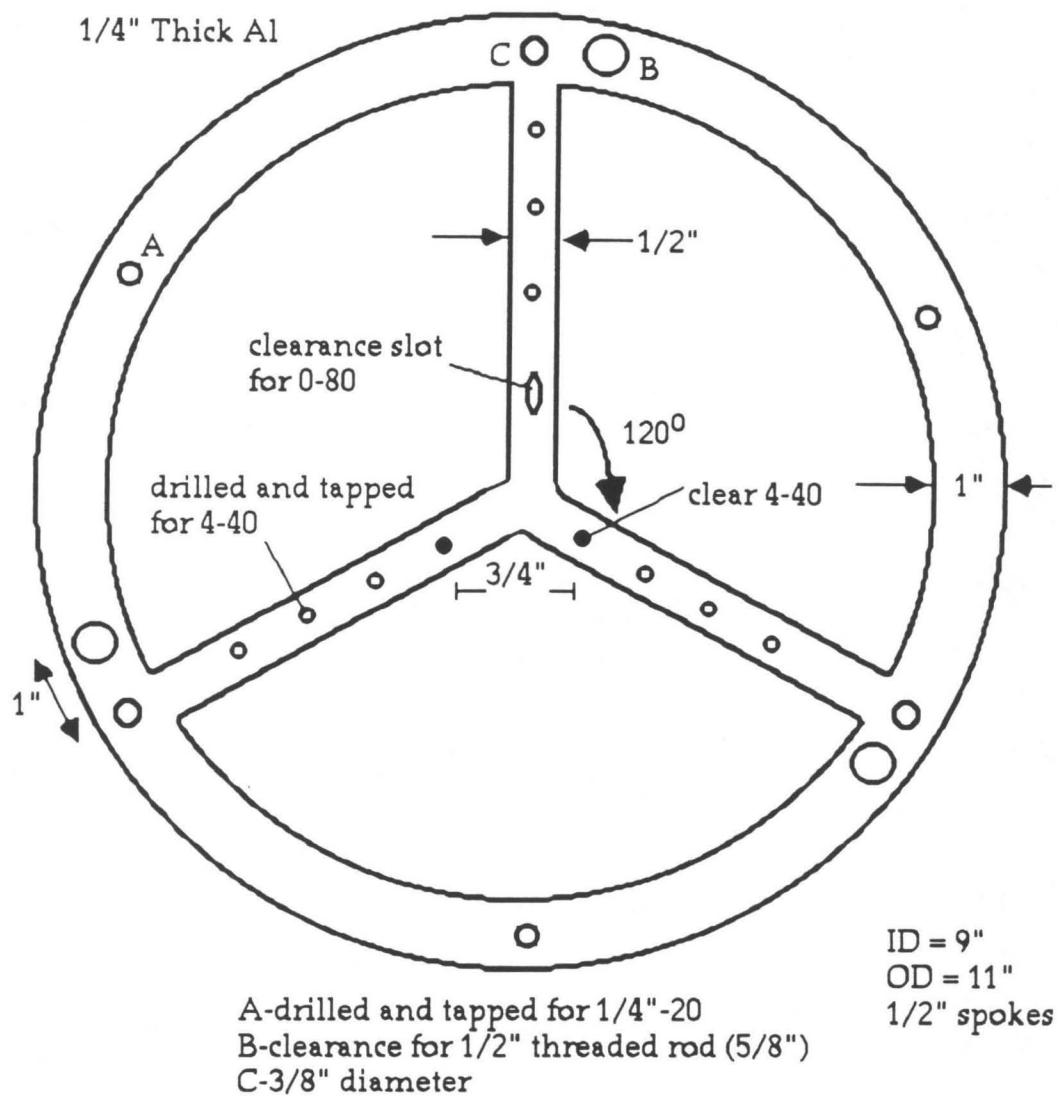


Figure 12: Top plate of the vibration-isolation spring stand. (not to scale)



*Clearance holes and slot in center fit STM screws and adjustment screw exactly.

Figure 13: Base plate of the vibration-isolation spring stand upon which the STM is mounted. (not to scale)

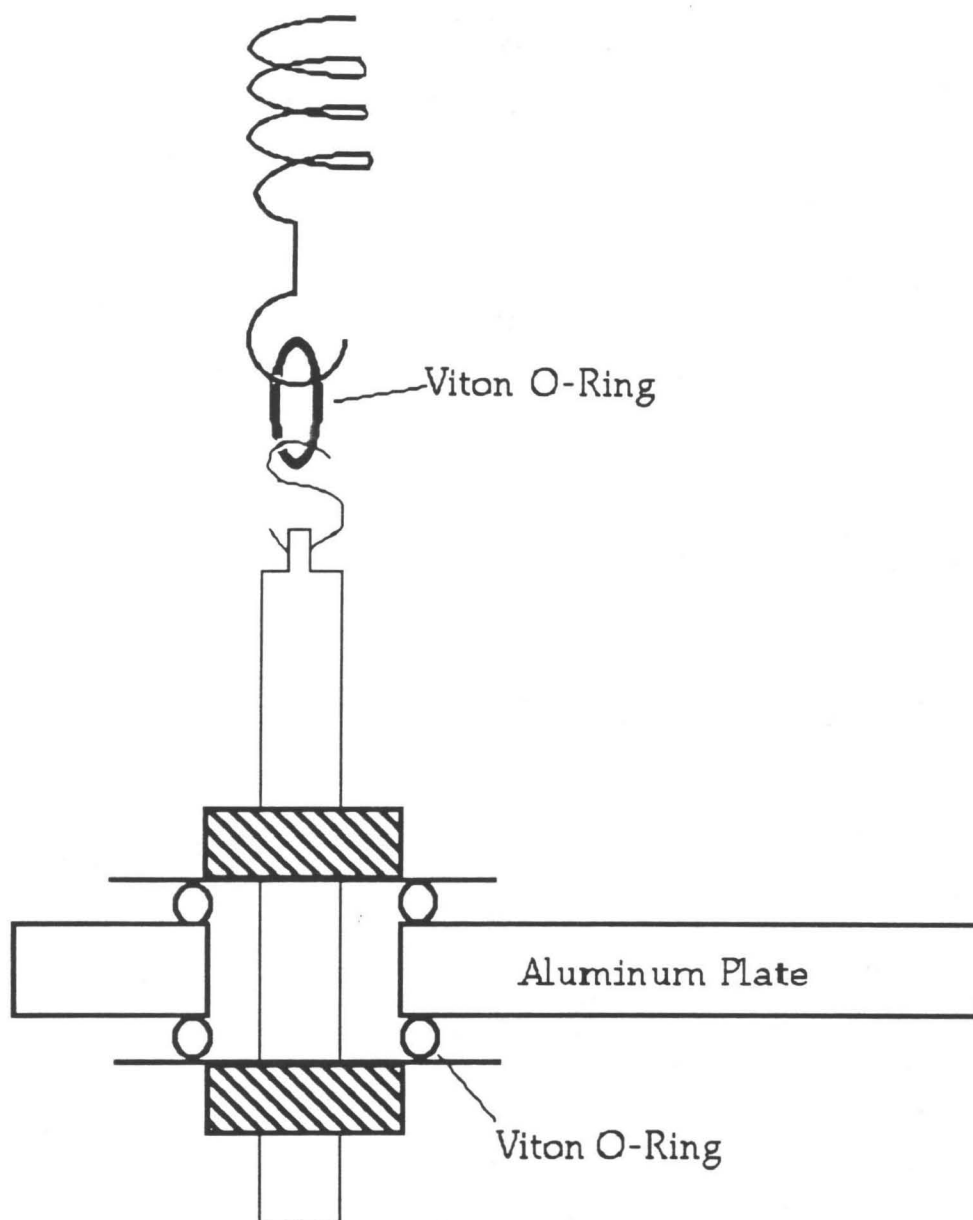


Figure 14: Electrical and vibrational decoupling of the vibration support structure from the STM stage. Viton O-rings provide electrical insulation as well as vibrational damping. The system is repeated at the upper support plate as well.

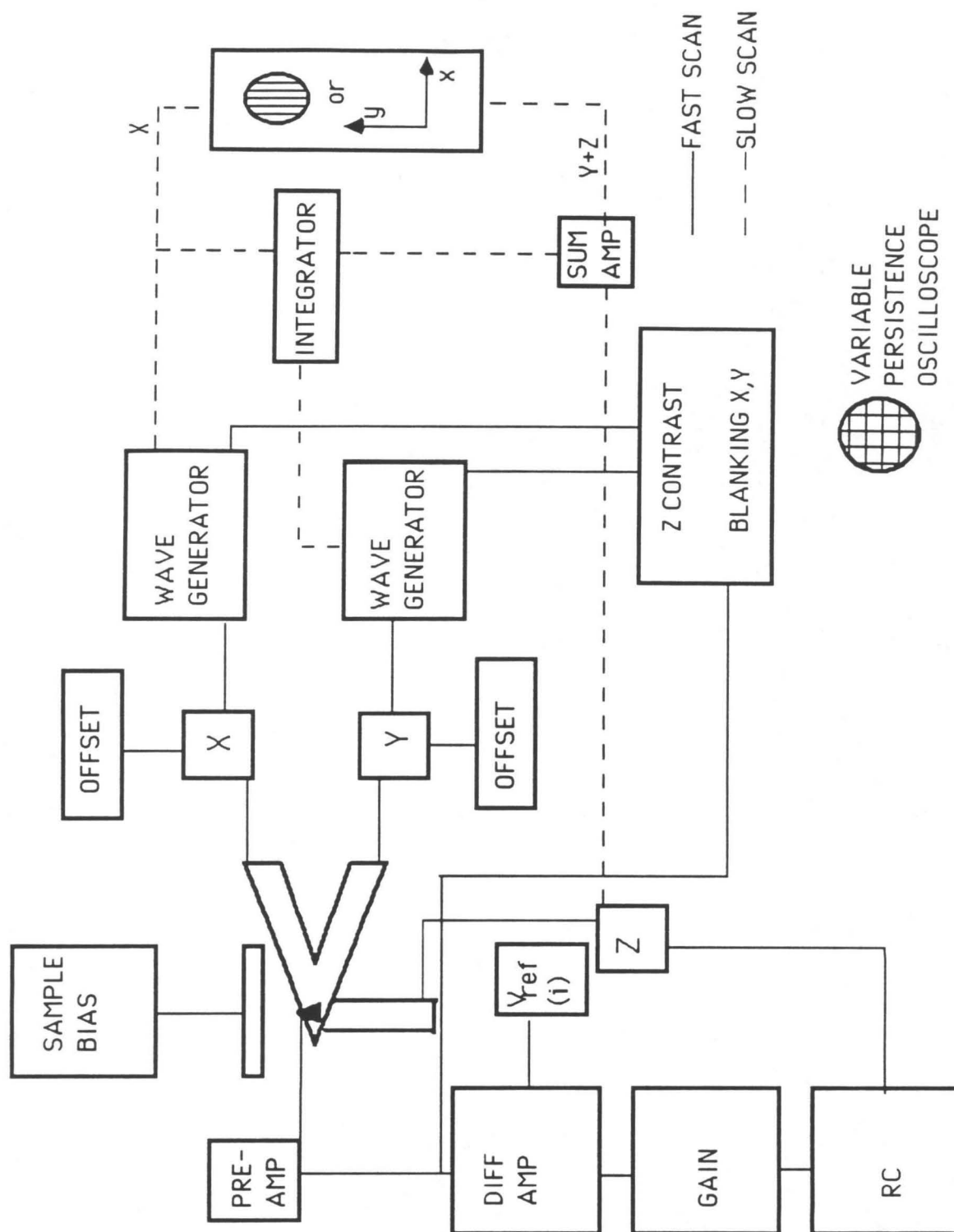


Figure 15: Block electronic diagram. This schematic representation of the entire circuitry of the STM shows the required components for both fast and slow scans. Details are found in the text and in the remainder of the figures.

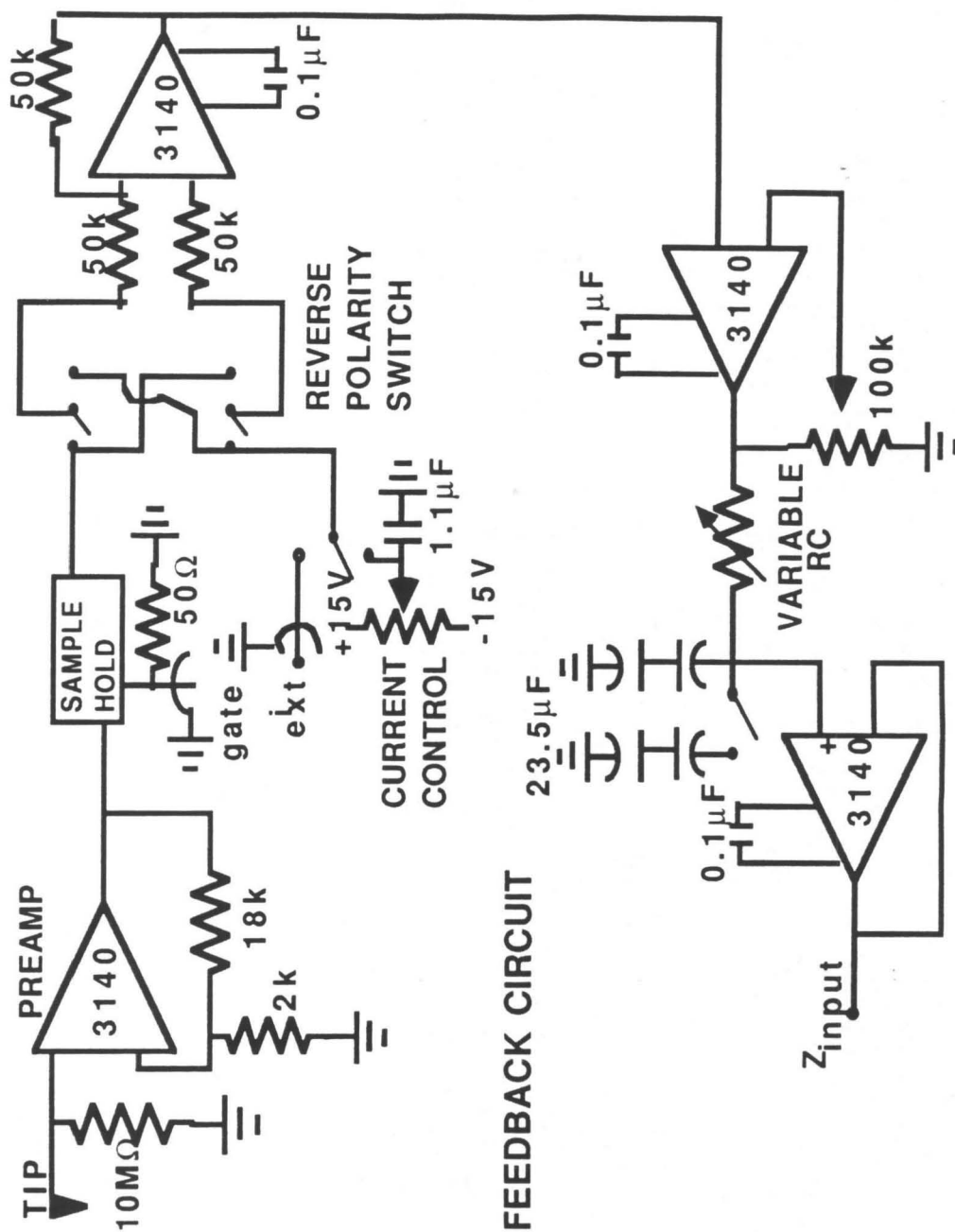


Figure 16: The feedback circuit for maintaining a constant current by moving the tip in and away from the sample by a voltage-driven piezoelectric ceramic.

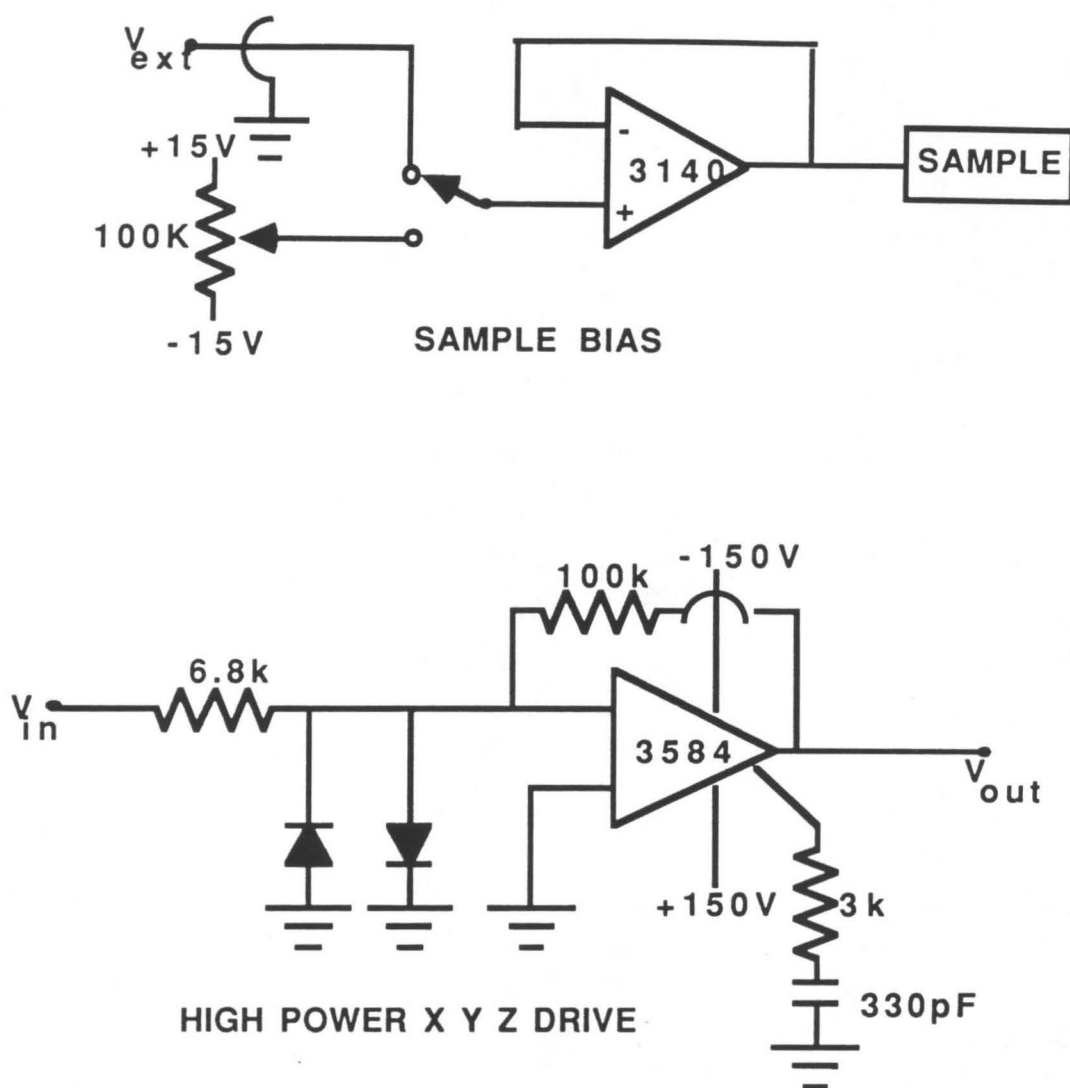


Figure 17: The a) the high power X Y Z drive and b) the sample bias circuit.

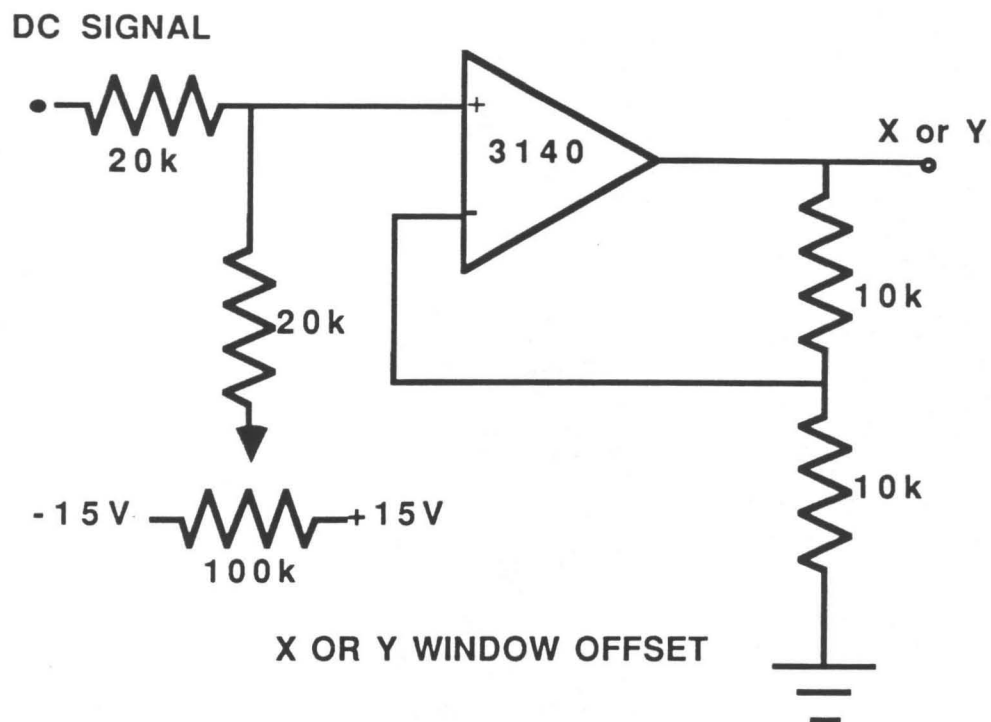


Figure 18: The X and Y offset circuit.

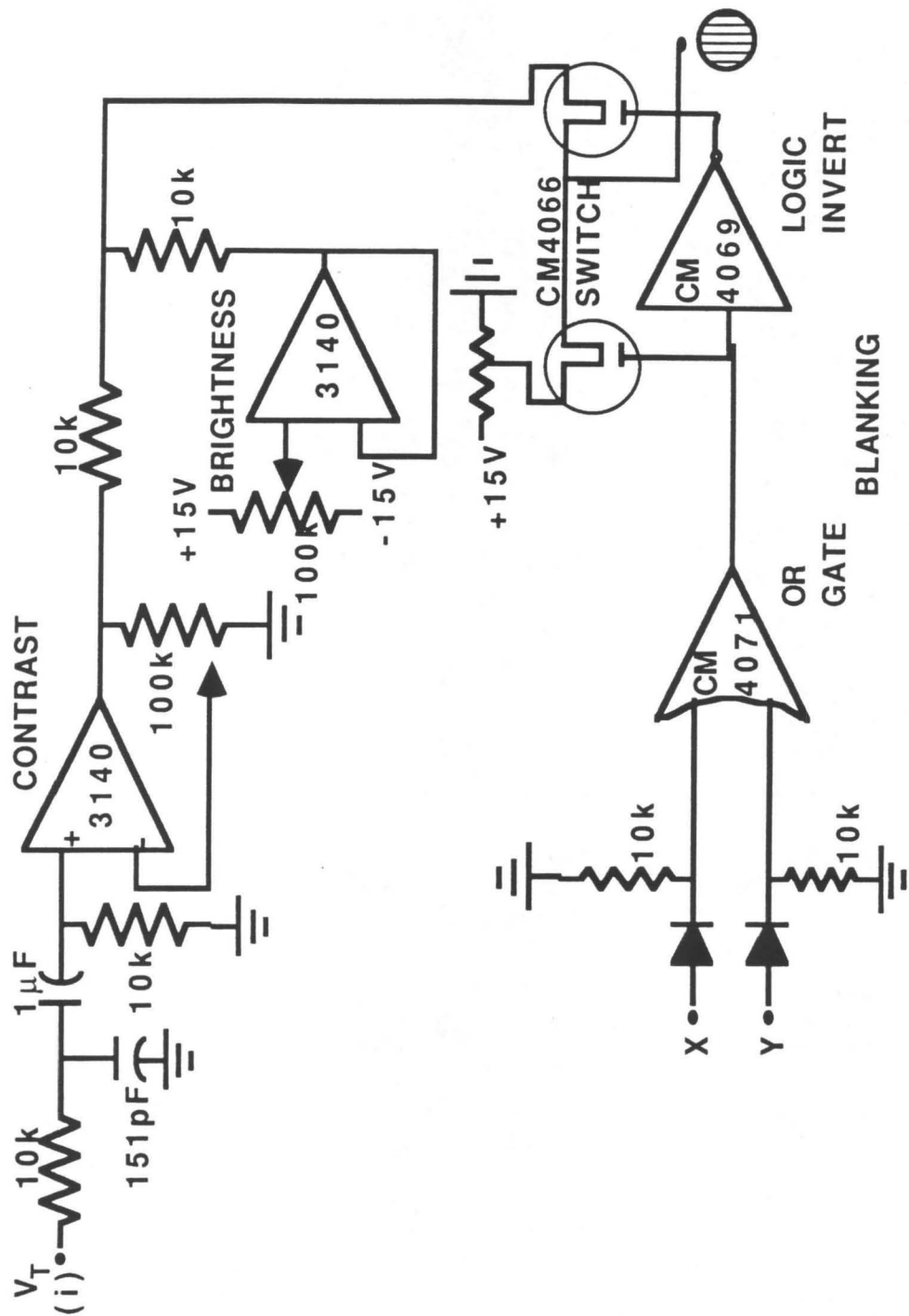
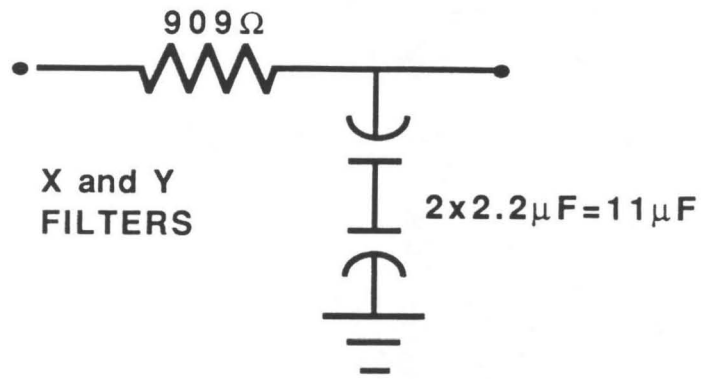
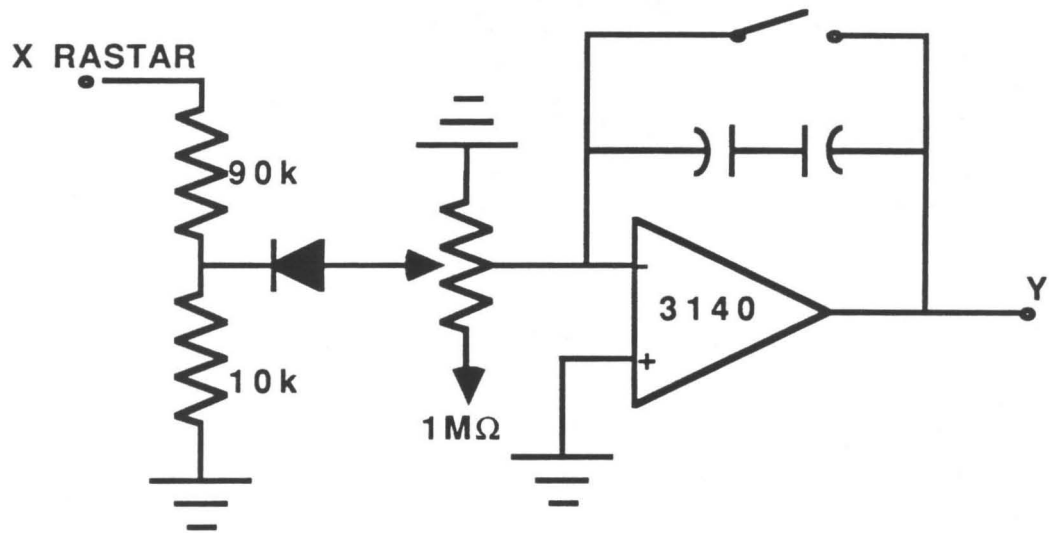


Figure 19: The contrast, brightness and blanking circuit for control of the Z output.



LOW PASS FILTER



VARIABLE INTEGRATOR

Figure 20: The variable integrator and low-pass filter.

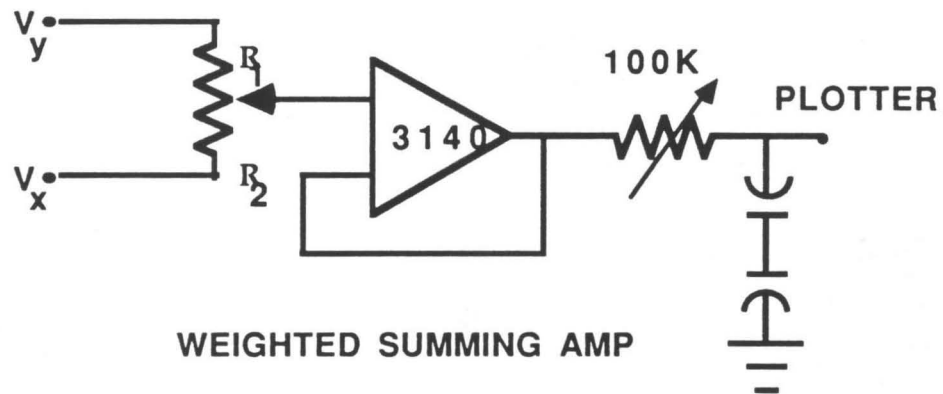
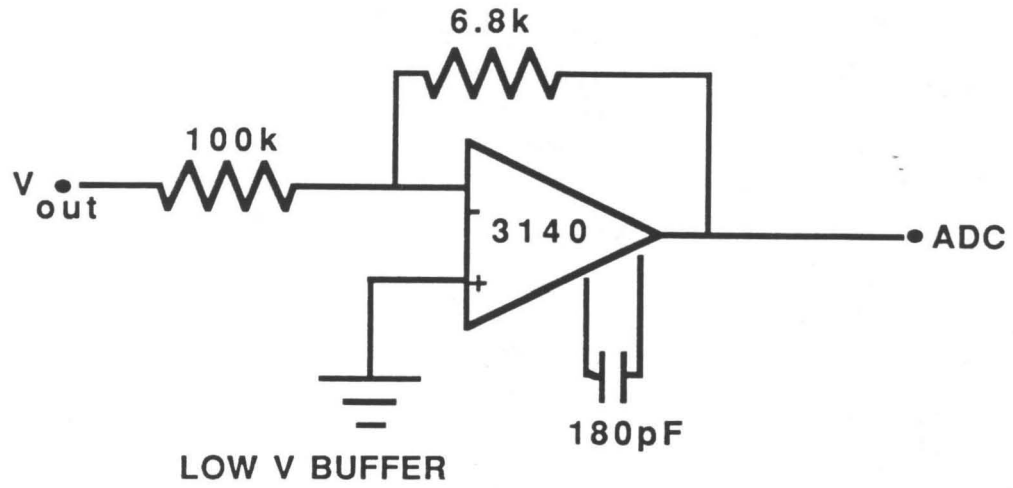


Figure 21: The low voltage buffer and summing amplifier.

Appendix B

ON IMAGING BIOLOGICAL MOLECULES
WITH THE SCANNING TUNNELING
MICROSCOPE--
A PROTEIN-ANTIBODY COMPLEX

INTRODUCTION

The ability to observe the structure of biological molecules on an atomic scale has been possible only for select samples. Samples are crystallized meticulously so that x-ray diffraction or LEED patterns can be obtained. These analytic techniques, while potentially useful, have the disadvantage that they require large numbers of molecules whose individual characteristics may be lost by the averaging. Furthermore, they are not direct imaging techniques and rely upon transformation calculations to derive atomic positions. Additionally, the crystalline structure of the sample may not represent adequately the characteristics of the molecule in its natural state.

Molecular resolution can be observed for larger biological molecules with Scanning Electron Microscopy only for samples "shaded" with a conducting layer. Although the general structure of the molecule can be deduced, direct observation of single molecules to atomic resolution has not yet been possible by these techniques. With the development of the STM, another technique is emerging for examination of molecules to molecular or potentially atomic resolution with the added advantage of nondestructive analysis of individual molecules in ambient atmospheres or liquid solutions.

Although biological molecules do not typically support current transport through them, several attempts at imaging proteins¹ and nucleic acids² with the STM have been marginally successful. An astounding atomically resolved image of double-stranded DNA³ shows the potential that may be found in STM imaging, although reproducibility and interpretation of height from these images is difficult. The ability to distinguish between the electronic nature of each imaged site by Scanning Tunneling Spectroscopy (STS), thus providing chemical distinction, needs to be further developed to realize STM's full potential for molecular imaging.

For successful STM imaging of any molecule, the need for a stable complex on the surface is imperative to ensure that the tip does not move the object under study. Although conductivity of the molecule has been an

¹Johann P. Ruppertsberg, J. K. H. Hörber, Ch. Gerber and G. Binnig *FEB* 257 (2), 460 (1989)

²David D. Dunlap and Carlos Bustamante *Nature* 342, 204 (1989)

³Robert J. Driscoll, Michael G. Youngquist and John D. Baldeschwieler *Nature* 346 (6281), 294 (1990)

assumed necessity, a conductive substrate may be adequate for providing electron conduction away from the molecule for smaller samples. The possibility that tunneling is occurring not to energy levels within the sample but to perturbed surface levels⁴ could account for this phenomenon.

This appendix presents a collaboration with Abbott Laboratories towards the observation of an antibody-antigen complex covalently bound to a sputtered gold surface. This sample was not examined extensively, but the work is significant because the nature of imaging and interpreting STM of biological molecules is well represented by this study. Although the identification of the antigen-antibody complex was not verified by other techniques, the size and characteristics of the feature under imaging conditions are consistent with this tentative assignment. The stability of the adsorbate was sufficient to scan reproducibly a single complex numerous times. The molecule could be removed, however, by applying a negative sample bias. The relative "flatness" of the gold surface provided a smooth background, a conductive substrate and a surface with enough reactivity with which to bind linkers for the antibody complex. A discussion of the parameters and considerations in imaging such large biological molecules is presented.

EXPERIMENTAL

The samples studied were supplied by Abbott Laboratories⁵ and examined in an ultrahigh vacuum STM system. The substrate was a sputtered gold layer on ~1000Å metallic chromium layer, deposited for adhesion on a silicon wafer slice. Abbott's measurements with elliptical reflectometry predict a film thickness of $2820 \pm 0.8\text{\AA}$. The antibody complex consisted of an amino-propyl silane linker to a human serum albumin protein (HSA). An antibody (anti-HSA) was subsequently bound to the HSA to produce the entire complex.

The antibody complex sample was rinsed with doubly distilled H₂O and dried with N₂. The samples were introduced into the UHV system through a nitrogen-purged load lock and long stroke translator. STM images

⁴M. G. Youngquist, R. J. Driscoll, T. R. Coley, W. A. Goddard and J. D. Baldeschwieler *J. Vac. Sci. Technol. B* 9 (2), 1304 (1991)

⁵Dr. Steven Stroupe, D9TW, Building AP20, Abbott Labs, Abbott Park, IL 60064 in August, 1990

were taken at less than 10^{-9} torr with freshly ac-etched tungsten tips. All images were taken at 1nA feedback current in the standard constant current mode at +2.2V sample bias unless noted for each image presented.

RESULTS

Sputtered Gold Surface

The HSA samples are spread in less than monolayer coverage on the sputtered gold surface. Rough areas are observed on the surface by STM, but more often, areas with large terraces and multiple atomic steps were observed. **Figure 1** (ABH080B) shows a typical $340 \text{ \AA} \times 340 \text{ \AA}$ area on the surface with a number of atomic steps. The step density is relatively high, suggesting that the underlying mica or chromium layer is not atomically flat. The step heights correspond to single and multilayer steps as expected for the Au(111) surface. A smaller image of such an area is shown in **Figure 2** (ABH080H), which is $90 \text{ \AA} \times 90 \text{ \AA}$ and shows a total Z variation of 1.4 \AA , atomically flat. Although no antibody is present in these images, this surface represents the type of ideal, flat area on which identification of a protein complex could be accomplished.

Antibody Complex on Sputtered Gold Surface

Occasional bumps of the dimensions expected for the HSA + anti-HSA complex are observed on the surface. One such item is shown in the large area, $1400 \text{ \AA} \times 1400 \text{ \AA}$ image of **Figure 3** (ABH081D). The surrounding area is not as smooth as observed on the atomically flat, terraced areas, but the small bump remains persistent through a number of scans of the area.

Upon closer examination of the bump, the features of the complex can be better discerned. The image in **Figure 4** (ABH082B) is $670 \text{ \AA} \times 670 \text{ \AA}$. The two halves of the complex are separated by a valley. The molecule in the image is 168 \AA wide and 132 \AA long.

Molecular Manipulation

A series of $340 \text{ \AA} \times 340 \text{ \AA}$ images taken at this particular site for various sample biases are shown in **Figure 5a-c** (ABH082D-F). From the image of **Figure 5a**, the dimensions of the complex can be seen. The width of the

complex is 232\AA and the length is 142\AA (the dimensions may seem distorted by the method of presentation-- x vs y+z because of the convolution of a large z gain with y). The molecule seems to be spread out by subsequent scans when compared to the image in **Figure 4** and may appear larger than it really is due to the macroscopic size of the tip. The bias is subsequently switched to a negative sample bias (from $+2.2\text{V}$ to -2.2 V so electrons tunnel out of the sample to the tip) to determine if changing the tunnel parameters will enhance the resolution or change the character of the image. The result is shown in **Figure 5b**. The image is clearly degraded. Upon returning to the original biasing voltage, the complex is completely removed as shown in **Figure 5c**.

DISCUSSION

The observations of molecular distortion and manipulation by the STM tip while imaging biological molecules is representative of the difficulties often encountered and the potential for molecular control with the STM. Molecular distortion is certainly likely due to the complex's insulating properties. The familiar Y-shaped antibody is typically $\sim 130\text{\AA}$ wide across the short chain (top of the Y) and $\sim 120\text{\AA}$ parallel to the long chain (leg of the Y)⁶ Consequently, although the observed images have a valley that could correspond to the Y shape, the complex appears large because of the molecule beneath, the shape of the tip and the previously mentioned spreading effect from tip interactions with the molecules. Additionally, the STM tip may have to push into the molecule in order to attain a distance conducive to tunneling to the surface. As observed in **Figures 3 - 5a**, the complex was distorted, but not removed. Presumably, the molecule was bound tightly to the linker, which in turn was covalently bound to the gold surface.

The ability to remove a molecule with the tip at different biases is beginning to appear in the literature. Lyo and Avouris⁷ have recently been able to move single atoms or clusters selectively from or to a silicon(111) (7×7) surface. By applying a bias of the appropriate polarity, they have selectively removed and deposited atoms at specific sites.

6Joseph A. Belianti *Immunology III* (W B Saunders Co.: Philadelphia), 93 (1985)

7I. Lyo and Ph. Avouris *Science* 253, 173 (1991)

The fact that the HSA+anti-HSA sample was removed at a negative sample bias suggests either that the molecule was unstable when electrons were drawn from it or that a lower density of states was available from which to tunnel, resulting in physical removal by the tip. Since conduction and stability did not seem to be a problem at positive bias, the latter suggestion is more probable. Thus, in order to draw current from the sample and transfer it to the tip, the tip was required to move closer to the surface. It is speculated that the tip was *in* the sample and that the molecule was either swept away or picked up by the tip upon scanning.

In imaging biological molecules with the Scanning Tunneling Microscope, parameters such as the polarity and magnitude of tunnel current will be important factors in determining the success of the experiment. The stability of the molecule on the surface and a smooth, flat background that provides adequate contrast are also necessary. With the development of STS and the Atomic Force Microscope as a complementary tool, atomic resolution of biological molecules is imminent.

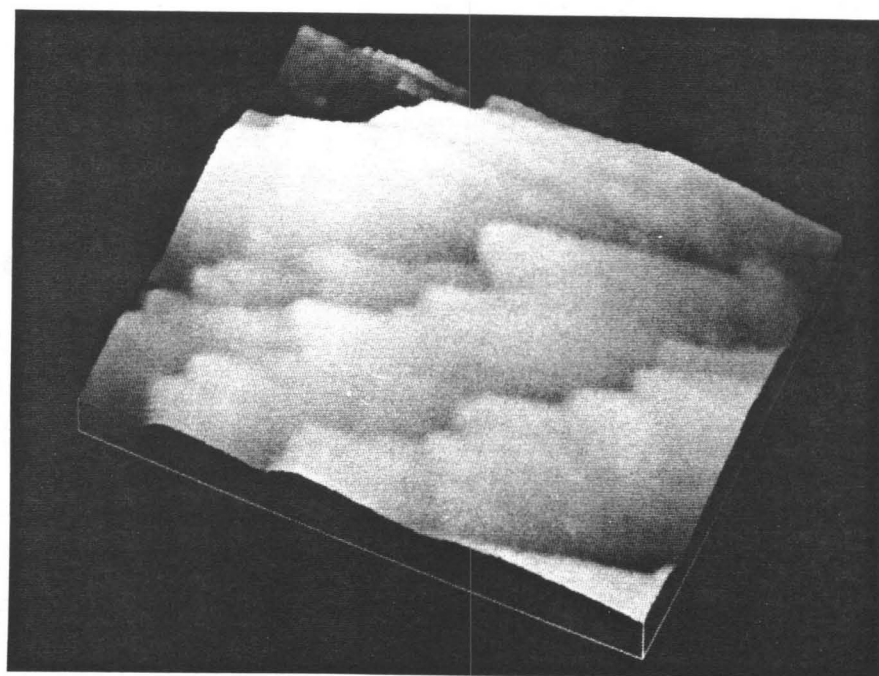
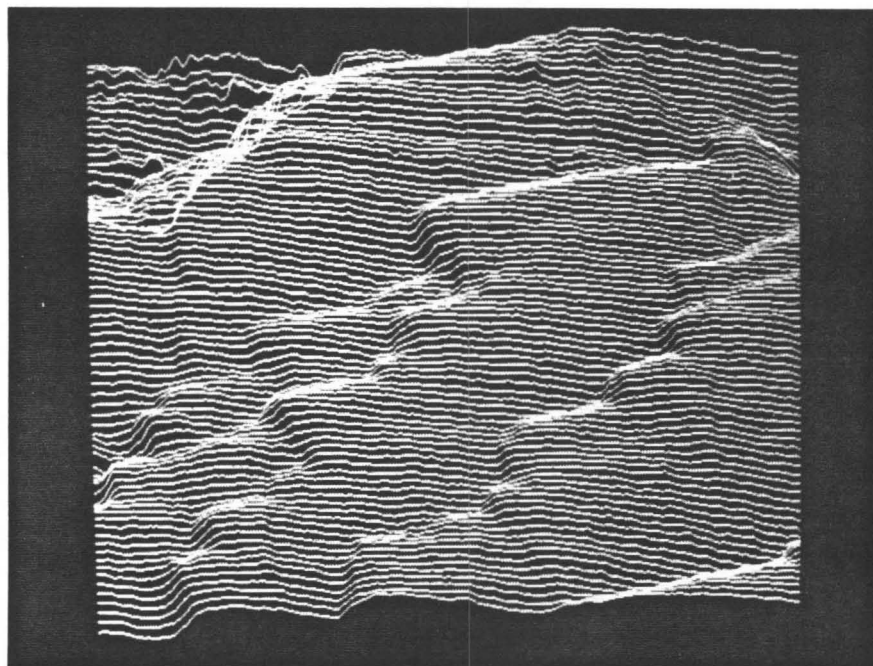


Figure 1: (ABH080B) A $340 \text{ \AA} \times 340 \text{ \AA}$ image of multiple steps on the sputtered gold surface. A Gaussian sliding window average smoothing of $\sim 2 \text{ \AA}$ FWHM was applied.

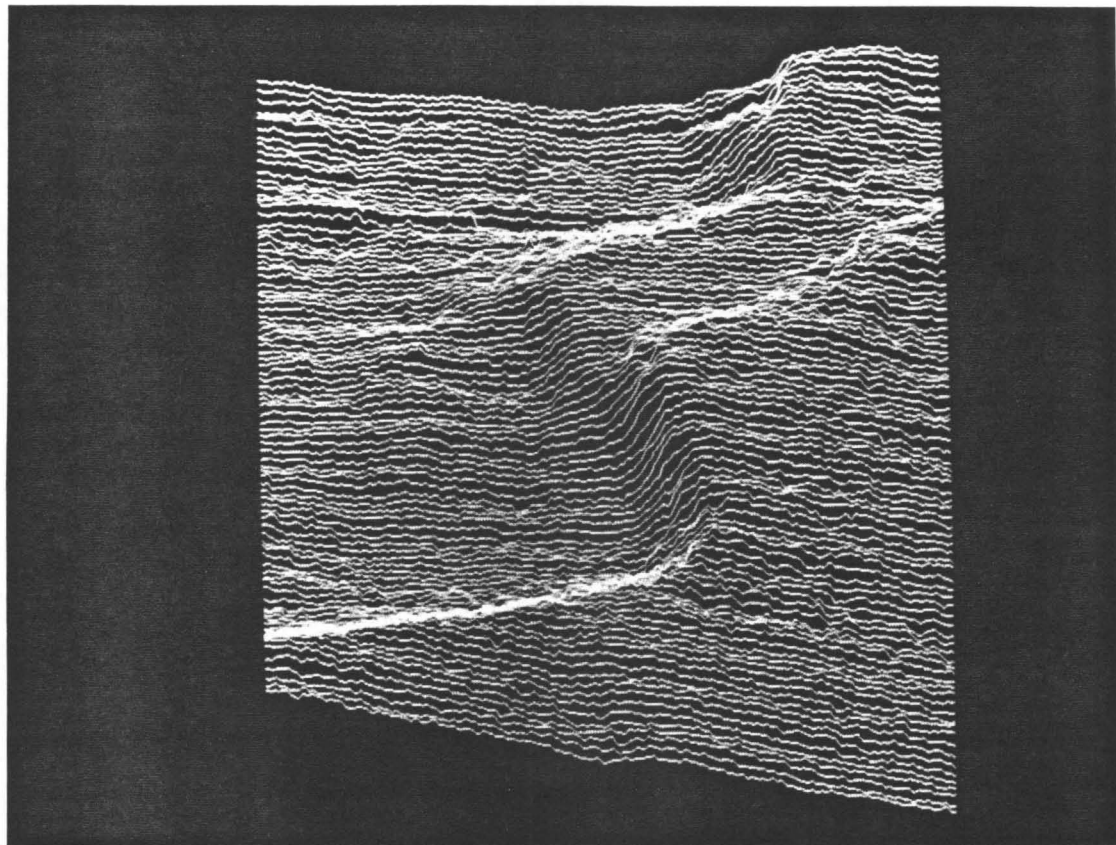


Figure 2: (ABH080H) A higher resolution image ($90 \text{ \AA} \times 90 \text{ \AA}$) of the flat terrace on a sputtered gold surface. (smooth $\sim 0.5 \text{ \AA}$ FWHM)

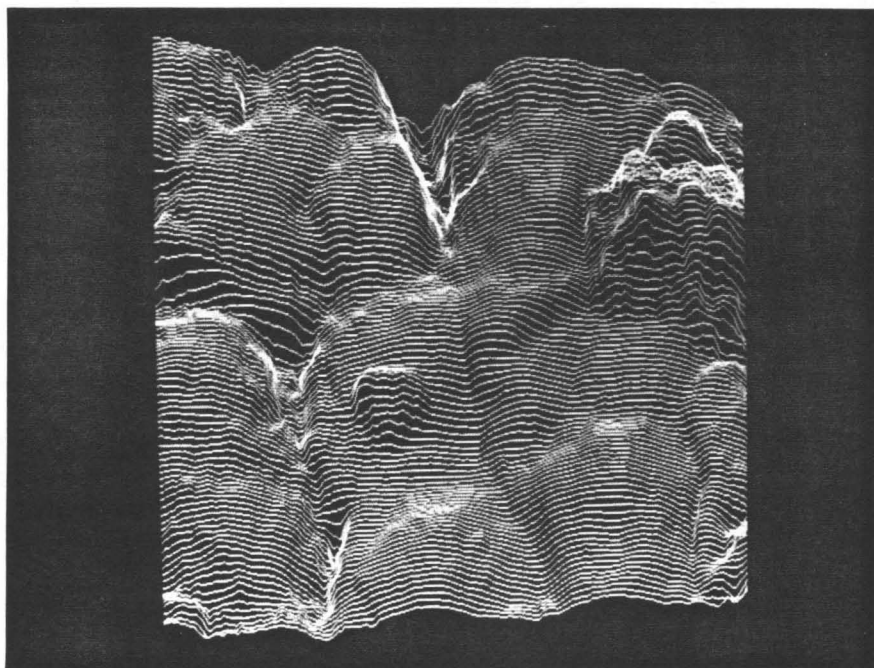


Figure 3: (ABH081D) A large $1400 \text{ \AA} \times 1400 \text{ \AA}$ image of an interesting feature on the sputtered gold surface. It measures $\sim 185 \text{ \AA}$ long by 145 \AA wide. (smooth $\sim 5 \text{ \AA}$ FWHM)

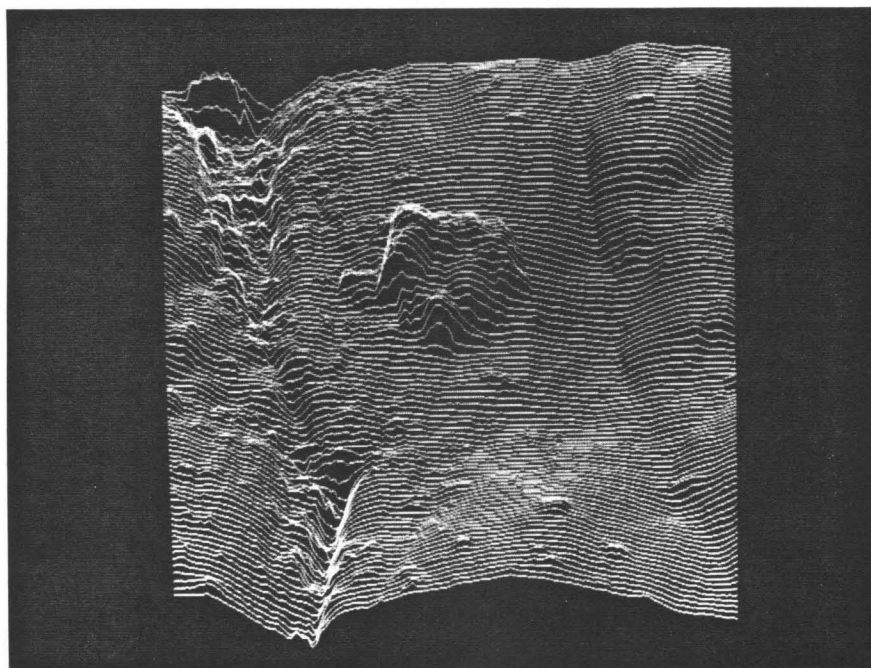
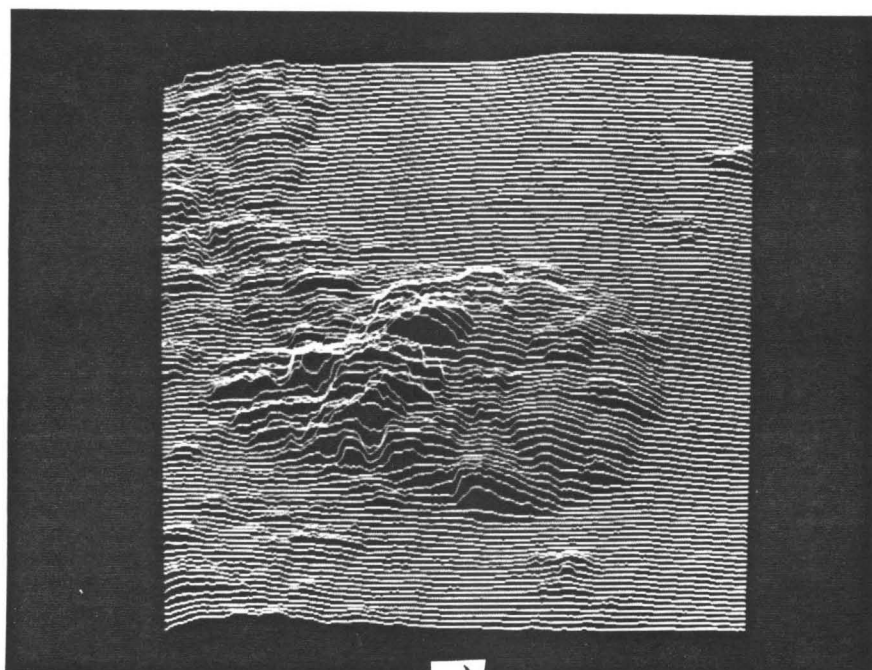
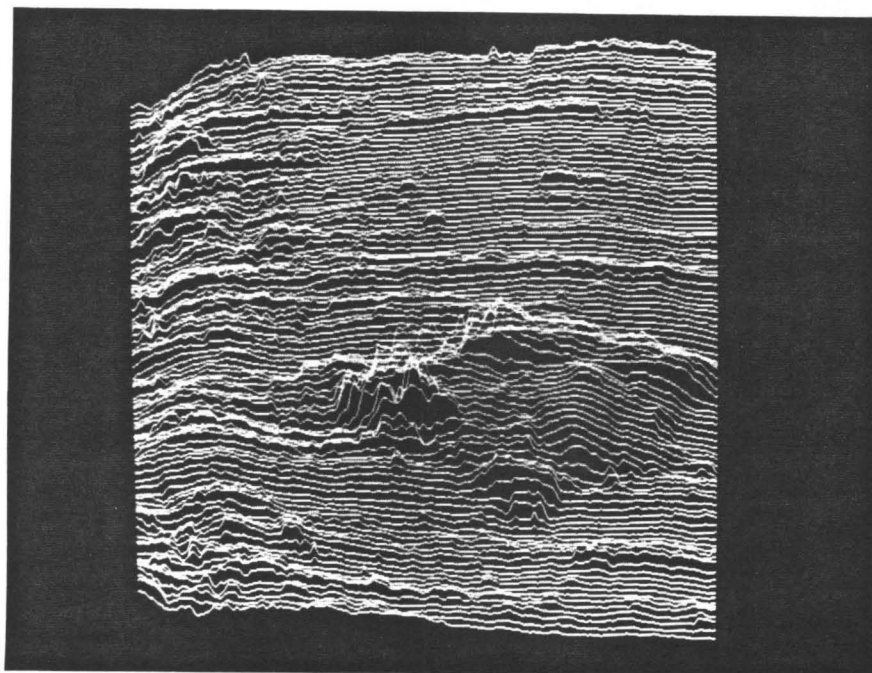


Figure 4: (ABH082B) Higher resolution ($670 \text{ \AA} \times 670 \text{ \AA}$) image of the feature of Figure 3. The feature is tentatively assigned to be the HSA + anti-HSA complex and is $\sim 130 \text{ \AA}$ long by 170 \AA wide. The height varies from 28 \AA on the shoulders of the complex to 18 \AA in the center valley.

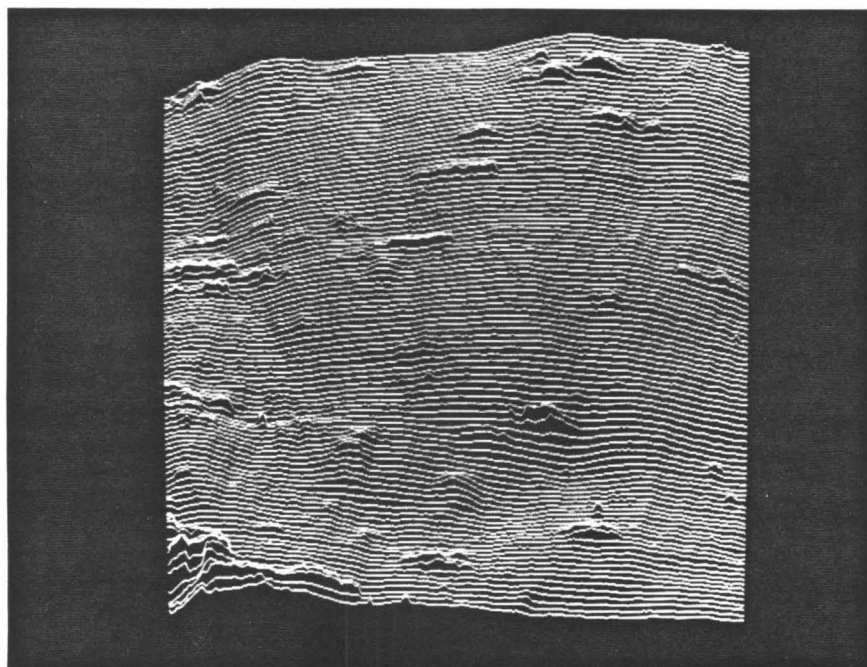


a)



(b)

Figure 5a-c: (ABH082D-F) A series of higher resolution ($340 \text{ \AA} \times 340 \text{ \AA}$) images of the complex shown in **Figure 4** taken at a sample bias of a) $+2.2 \text{ V}$, b) -2.2 V and c-next page) $+2.2 \text{ V}$. Notice that the image degrades at negative sample bias and seems to have disappeared upon returning to positive bias.



(c)

Figure 5c: (ABH082D-F) A series of higher resolution ($340 \text{ \AA} \times 340 \text{ \AA}$) images of the complex shown in **Figure 4** taken at a sample bias of c) $+2.2 \text{ V}$.